FINAL REPORT

on

Study of the Effect of Cloud Inhomogeneity on the Earth Radiation Budget Experiment

NASA grant NAG 5-101

Period covered: July 1, 1987 to August 31, 1988

Principal Investigator: Professor Phillip J. Smith

Department of Earth and Atmospheric Sciences

Purdue University, West Lafayette, In 47907

Early research on the above grant under the direction of the previous principal investigator, Professor Roger Davies, assisted in the design and validation of the inversion process for scanner data from the Earth Radiation Budget Experiment. This work was documented in references 1–3. More recent work at both Purdue and McGill Universities has concentrated on analysis of the scanner radiance data from both the ERBS and NOAA-9 satellites. This work has lead to the recognition of the major statistical dependences in the radiances data and the need for an unbiased sampling strategy to obtain accurate monthly mean radiation budgets.

Research on the subject grant is best summarized in the attached thesis of François Payette (reference 5) which was written under the supervision of Professor Davies at McGill University. Referenced in this thesis is that of another M.Sc. student, Mr. Guoyong Wen, who was also supervised by Professor Davies (reference 4). A joint publication between Davies and Payette, summarizing the highlights of the thesis findings is currently in preparation and will acknowledge support under this grant number.

References

1.   "Reflected Solar Radiances from Broken Cloud Scenes and the Interpretation of Scanner Measurements". R. Davies, *J. Geophys. Res., 89,* 1259—1266, 1984.

2.   "Inversion Methods for Satellite Studies of the Earth's Radiation Budget: Development of Algorithms for the ERBE Mission". G. L. Smith, R. N. Green, E. Raschke, L. M. Avis, B. A. Wielicki and R. Davies. *Rev. Geophys., 24,* 407—421, 1986.

3.   "The Effect of Cloud Sides on Reflected Solar Radiation as Deduced from Satellite Observation". J. A. Coakley and R. Davies. *J. Atmos. Sci., 43,* 1025—1035, 1986.

4.   "Analysis of ERBE scanner data". Guoyong Wen, M.S. thesis, Dept. of Earth and Atmospheric Sciences, Purdue University, 1987.

5.   "Applications of a sampling strategy for the ERBE scanner data", F. Payette, M.Sc. thesis, Dept. of Meteorology, McGill University, 1988.

Applications of a sampling strategy

for the

ERBE scanner data

by

François Payette

A Thesis submitted to the Faculty of Graduate Studies and Research in partial fulfillment of the requirements for the degree of Master of Science.

September, 1988
Department of Meteorology
McGill University
Montreal, Quebec

à Marie-France

ABSTRACT

The Earth Radiation Budget Experiment (ERBE) is the most recent and probably the most intensive mission performed in order to gather precise measurements of the Earth's radiation components. The data obtained from ERBE will certainly be of great importance for future climatological studies.

A statistical study reveals that the ERBE scanner data are highly correlated and that instantaneous measurements corresponding to neighbouring pixels contain almost the same information. Analyzing only a fraction of the data set when sampling is suggested and applications of this strategy are given in the calculation of the albedo of the Earth and of the cloud-forcing over ocean.

RESUME

La mission ERBE (Earth Radiation Budget Experiment) est la plus récente et probablement la plus importante des missions spatiales ayant pour but de mesurer précisement l'intensité de la radiation réfléchie et émise par la terre. Les données fournies par ERBE seront certainement d'une grande utilité pour de futures études climatologiques.

Une étude statistique révèle que les données de ERBE provenant des instruments à haute résolution sont fortement corrélées et que des mesures simultannées correspondant à des pixels voisins fournissent une information presque identique. Cette recherche suggère qu'une fraction seulement de l'ensemble des données soit anlysée et présente aussi en guise d'applications un calcul de l'albedo de la terre ainsi que du forçage radiatif dû à l'ennuagement au-dessus des océans.

ACKNOWLEDGEMENTS

TABLE OF CONTENTS

LIST OF FIGURES

LIST OF TABLES

Chapter 1

Introduction : the Earth Radiation Budget Experiment

1.1   Net radiation and ERBE

The treatment of radiation is an important aspect of climate modelling. The Earth receives shortwave (SW) radiation from the Sun which is partly reflected and partly absorbed by both the atmosphere and the planet surface. It also emits longwave (LW) radiation which is lost to space. On the average, the net radiative input, δ, can simply be written as

$$\delta = \frac{S_o}{4} (1 - \alpha) - L \qquad (1.1)$$

where S_o is the solar constant

α is the albedo i.e. the ratio of the reflected SW irradiance to the incident solar irradiance

and   L is the outgoing LW irradiance emitted by the Earth and its atmosphere.

On a global scale and over a large period of time (on the order of years), we would certainly expect δ to be zero since during this period the Earth remains on the average in radiative equilibrium. But for regional studies the net incoming radiation is non-zero and it is this radiative input or output that drives the atmospheric and oceanic circulations.

For the last 25 years, satellites (for example the Tiros and Nimbus series) have been used to study net radiative input (Stephens *et*

1

al., 1981 and Smith *et al.*, 1986). At first more global studies were made, but with time more accurate measurements were needed over smaller regions (i.e. a better resolution) in order to perform more sophisticated studies.

The Earth Radiation Budget Experiment (ERBE) was organized in order to obtain such measurements (c.f. Barkstrom, 1984). It is the first multisatellite system designed to precisely measure components of the Earth's radiation budget and it features an improved sampling procedure developed on the basis of the experience gained from the Nimbus 6 and 7 missions.

The ERBE system is composed of three satellites : the Earth Radiation Budget Satellite (ERBS) and two NOAA satellites (NOAA-9 and -10). The orbital characteristics of the three satellites were chosen in order to maximize the amount of surface viewed and diurnal coverage, within budgetary and launch constraints. ERBS is a 57° inclination NASA satellite situated at an altitude of 600 kilometres and precesses 4.95° west per day (i.e. 180° in 36 days). The two NOAA satellites are respectively at altitudes of 870 km and 833 km and have inclinations of 98.91° and 98.75° ; both are sun-synchronous.

1.2 The ERBE instruments

There are two instrument packages on each of the ERBE satellites : scanner and non-scanner radiometers. Each satellite also has calibration equipment on board. The non-scanner package contains 4 Earth-viewing detectors and a solar monitor. There are 2 spatial resolutions : a limb-to-limb Wide Field Of View (WFOV) and a 1000 km

diameter Medium Field Of View (MFOV). Shortwave (0.5 to 5 μm) and total wavelength measurements are made at each of these spatial resolutions. Non-scanner measurements are taken every 0.8 seconds.

The scanner package contains 3 Earth-viewing broadband channels :

SW (0.2 to 5 μm)

LW (5 to 50 μm)

total (0.2 to 50 μm)

The value of 5 μm for the wavelength was chosen to be a good point at which to separate solar and terrestrial radiation.

The scanner instruments are mounted on a pedestal which rotates in the azimuthal direction and usually scans perpendicularly to the orbital track because this maximizes the spatial coverage (more complex scanning patterns were used with Nimbus 6 and 7). The instantaneous field of view (FOV) is hexagonal in order to decrease aliasing and is 4.5° along satellite ground track and 3.5° wide. At nadir, the area viewed is :

47 × 31 km for ERBS

65 × 44 km for the two NOAA's.

A complete scan including resetting for the next scan takes 4 seconds and contains 62 pixels.

1.3 The measurements

The ERBE measurements must be treated before being used for climate study purposes (see Smith *et al.*, 1986). Initially they consist of raw data from thermometers which are subsequently converted to satellite altitude radiances in physical units.

The scanner and non-scanner instruments provide important but different types of information. The advantage of the non-scanner measurements is that they give a better idea of the global and regional outgoing flux density. The scanner measurements are much more useful because of the small resolution and the different viewing positions which allow a study of angular dependence of the physical quantities, but we need to infer a value of the flux from the measured radiance in order to study climatology. This can be done using the angular distribution function $\mathcal{R}$, also called the bidirectional function for SW. It is defined as

$$\mathcal{R}_\Lambda = \frac{\pi \, I_\Lambda}{F_\Lambda} \qquad (1.2)$$

where I and F are respectively the radiance and the flux density which, for a matter of convenience, will simply be referenced by the term flux throughout the text, and where the subscript Λ indicates the wavelength range (SW or LW). $\mathcal{R}$ gives an idea of the asymmetry of the radiation field ; if it is identically equal to one the field is isotropic. For the ERBE data, $\mathcal{R}$ was empirically determined using Nimbus 7 data as well as models derived from GOES and AVHRR data.

One difficulty is to choose the correct $\mathcal{R}$ for the scene type the scanner is looking at. The problem is to identify this scene type. The ERBE data are classified according to 12 scene categories given in Table 1.3.1. They include four divisions of cloudiness which are clear (0 to 5% cloudiness), partly cloudy (5 to 50% cloudiness), mostly cloudy (50 to 95% cloudiness) and overcast (95 to 100% cloudiness). As for the

4

TABLE 1.3.1 The twelve ERBE scene types

Scene identification number	Description
1	clear ocean
2	clear land
3	clear snow
4	clear desert
5	clear land-ocean mix
6	partly cloudy over ocean
7	partly cloudy over land or desert
8	partly cloudy over land-ocean mix
9	mostly cloudy over ocean
10	mostly cloudy over land or desert
11	mostly cloudy over land-ocean mix
12	overcast

surface characteristics, they are easily determined knowing the satellite position and the geography. For the cloud coverage, use is made of Maximum Likelihood Estimators (MLE). The basic assumption is that :

clear skies are dark and hot

and   cloudy skies are bright and cold.

The brightness is characterized by the SW measurements and the temperature is determined by the LW measurements. This means that in a SW versus LW graph of outgoing radiation such as Fig. 1.3.1, clear sky radiance measurements are going to appear in the lower left of the graph and overcast radiance measurements will tend to be found in the upper right part of the graph. To obtain the MLE, measured radiances are compared with surface observations and are then classified according to the 4 cloud cover types. In the figure, the dot indicates the mean values of SW and LW radiances for each type and the decision line is determined using standard deviations of the radiances for the different categories of cloudiness (see ERBE PAT users' guide, 1987). The x shows an example of a pair of measurements (SW and LW) that will be classified. There are several different MLE's, one for each of the scanner and Sun position categories.

Problems are still encountered in the use of the bidirectional function $\mathcal{R}$. There is an important scatter of the data within a cloud category and it is still difficult with the MLE to distinguish between a few horizontally extensive stratiform clouds and many horizontally limited cumuliform clouds (Smith *et al.*, 1986). Theoretical derivations of $\mathcal{R}$ for cumulus- or stratus-like clouds might be useful since empirical
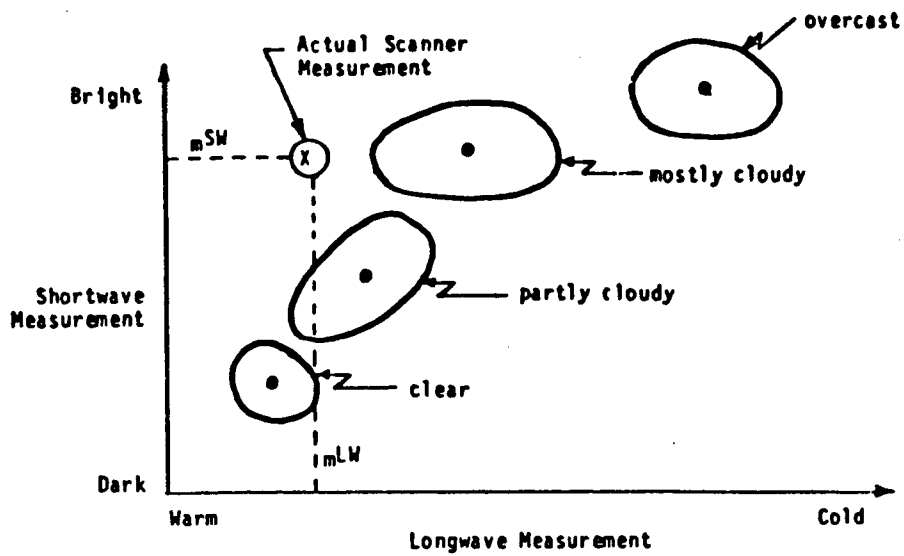
FIG. 1.3.1 Graph of SW and LW outgoing radiances. The Maximum Likelihood Estimators are based on such graphs.

data for a good estimation of $\mathcal{R}$ would require a very high resolution of the satellite instruments. Some work has been done in that field (Davies, 1984).

The main ERBE scanner data are the measured radiances, the estimated fluxes inferred from the bidirectional models and the scene identification. In the present study, only the unfiltered radiances are used. The filtered scanner radiance is the raw measurement corresponding to the integral over the SW or LW spectrum of the spectral radiance incident on the instrument weighted by the instrument spectral response, while the unfiltered scanner radiance is defined to be the same integral for a perfectly flat instrument spectral response. Either the SW or the LW unfiltered measurement is inferred from both the filtered SW, LW and total measurements using regression coefficients which are functions of directional angles, latitude and scene type (see ERBE PAT users' guide, 1987).

1.4   Viewing angle dependence

One of the major sampling problems for ERBE is the variation associated with viewing zenith angle. There are two important effects.

First, from elementary geometry, we know that the area viewed increases with viewing angle. Figure 1.4.1 shows the surface ratio across satellite track versus the distance from the nadir point. The surface ratio is defined to be the ratio of the area viewed by the scanner instrument normalized by the same area viewed at nadir. Up to 400 km ($\cong 40°$ from the satellite) the surface ratio is near 1 but increases rapidly afterwards. There is also a cutoff angle beyond which

ERBS
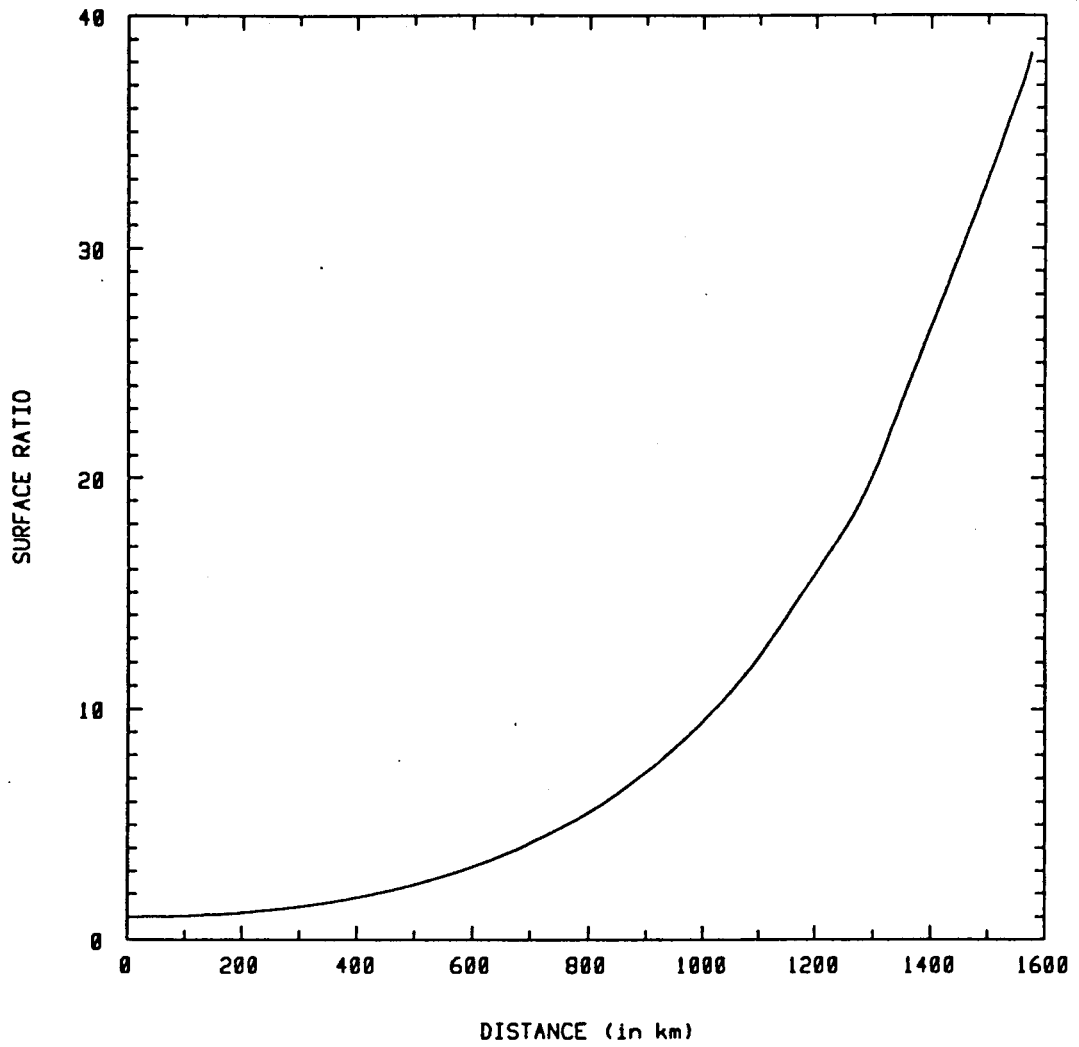
FIG. 1.4.1 Surface ratio versus distance across satellite track for the Earth Radiation Budget Satellite (ERBS).

the Earth does not entirely fill the field of view. Measurements for viewing angles larger than this value (e.g. near $70°$ for ERBS) are rejected.

The effect of cloud sides is also important. As the scanner goes towards large viewing angles it tends to classify broken cloud scenes as overcast scenes because it sees more of the cloud sides. This could affect the results obtained from analysis of the ERBE data.

1.5 Angle definitions

Figure 1.5.1 defines the important angles mentioned in this work. All angles are defined at the target point. θ is the zenith angle at which one sees the satellite and is called the viewing angle. θ_o is the zenith angle indicating the position of the Sun and is called the solar zenith angle. ϕ is the azimuthal angle which is $0°$ when the Sun is ahead of the viewing position and $180°$ when the Sun is behind the viewing position. It is called the relative azimuth.

The values of the cosine of θ and θ_o are also used and symbolized by μ and μ_o.

The symbol λ will be used to represent latitude with positive values of λ corresponding to the northern hemisphere.

1.6 The present study

Comprehensive analysis of the ERBE data presented in the previous sections is expected to yield interesting results regarding, for example, radiation budgets, symmetry of the radiation field or cloud-forcing. Since ERBE is an intensive and recent mission providing various

10
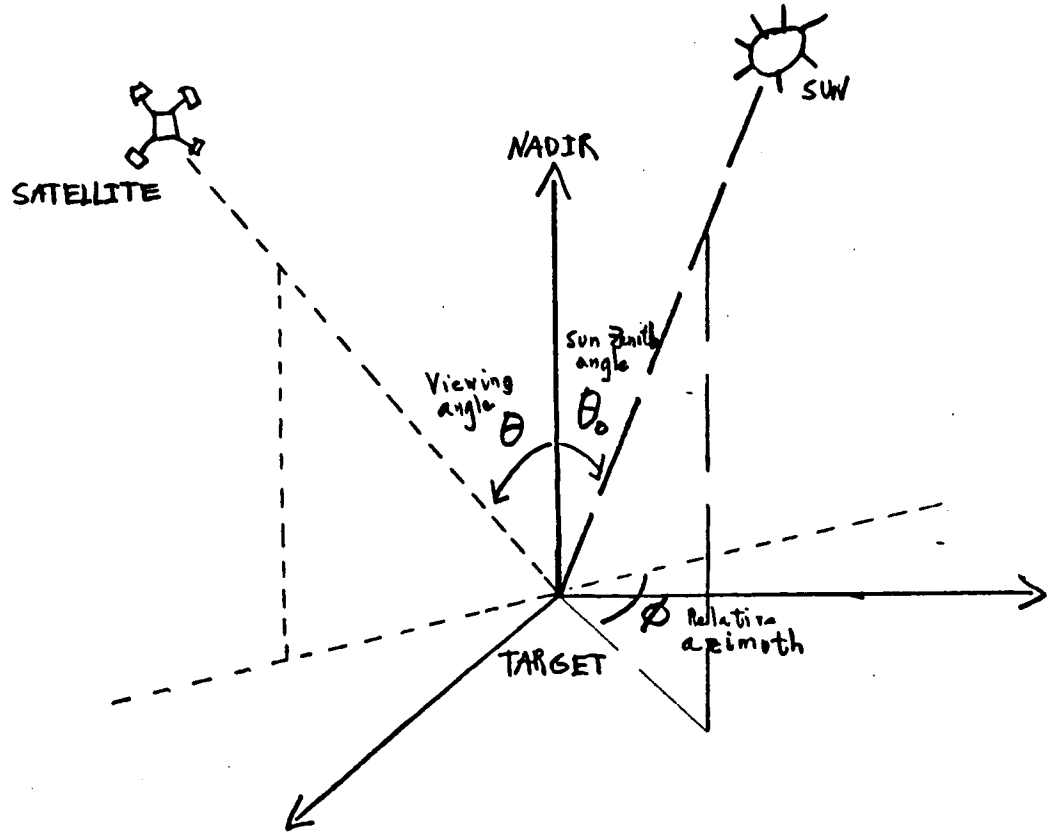
FIG. 1.5.1 Geometry characterizing the ERBE data.

measurements, one could be tempted to directly analyse the whole of the data in order to obtain such results. Before proceeding on such a task, however, it is of considerable interest to examine an initial subset of the data to determine its information content in a statistical sense, as well as its self consistency in terms of validation. An understanding of the statistical dependence of the data is in fact a prerequisite to determining an optional sampling strategy for obtaining monthly averages and for assessing the uncertainty in such averages due to both natural variability and potential biases in the inversion technique.

Consequently, this study is first directed towards an analysis of the ERBE data from a statistical point of view. In Chapter 2 we examine the correlation of the data and then develop a sampling strategy. This is applied in Chapter 3 to the study of climatological quantities such as the albedo and the cloud-forcing, mainly to observe the variability of the data and a possible dependence of these quantities on certain parameters.

The data used in this research are the diurnal unfiltered SW and LW radiances, the related estimated SW and LW fluxes and the scene identification numbers from ERBS and NOAA-9 for the month of April 1985. Data from ERBS November 1984 are also used.

Chapter 2

Correlation study

2.1 Statistical dependence of the ERBE data

Statistical independence is often assumed when applying classical statistical theory to scientific results. The value of a single datum is then considered not to be influenced by any other data and, conversely, it is assumed that this datum will not influence any other data value. For instance, this is usually the case when several length or time measurements are taken to estimate the value of a distance or a period of time. A set of results of the heads or tail game is also a classical example of an independent data set. But we could also think of a simple experiment where the results are not independent of each other. When, for example, one is outside and looks directly overhead to see if there are clouds, it is likely that he will get the same answer if he was to look at $45°$ above the horizon in front of him. These two observations are certainly dependent since cloudy areas are usually large. Such data sets cannot be treated with normal distribution statistics.

The earlier results of Wen (1987) showed that the ERBE scanner data cannot be considered as if they were statistically independent. His experiment has been repeated, confirming his results. He first divided the data according to viewing angle, solar zenith angle, latitude bins, and scene types, and then calculated the mean values of the radiances for each category for a set of 10 days of ERBS April 1985 data. These days were homogeneously distributed within the month so that he would

pick one day out of three consecutive days (e.g. the 1st, 4th, 7th, etc... of April). He then repeated this procedure twice for 10 other days of the same month thus obtaining three values of mean radiance for each category. He then compared the 3 absolute differences, $\Delta\overline{m}$, between the means of a category to the expected error of the mean $\sigma/\sqrt{N}$ of that data category (σ is the standard deviation and N is the number of data). If the data were totally independent, a normal distribution would be observed and 95% of the differences $\Delta\overline{m} - 2\sigma/\sqrt{N}$ for all categories would be negative, which is to say that 95% of the differences of the means would be within two standard deviations of the mean.

Table 2.1.1 shows the results based on ERBS April 1985 data. For each of the physical quantities studied (radiance or estimated flux), a mean value of $\delta = \Delta\overline{m} - 2\sigma/\sqrt{N}$ over all cases, $\overline{\delta}$, is presented with the number n(+) of cases where this difference is positive and the number n(-) of negative cases. The values of $\overline{\delta}$ give an idea of the departure of the $\Delta\overline{m}$'s from the standard error. It clearly shows that $\overline{\delta}$ is positive most of the time (at least 74% of the cases), and the data are not normally distributed. This leads us to think that the data are highly correlated and that the number of data N, even of the order of several thousands, is not large enough to invoke normal distribution statistics. Tables 2.1.2 and 2.1.3 show similar results based on ERBS November 1984 data and NOAA-9 April 1985 data respectively. From these three tables, it can be observed that the relative values of $\overline{\delta}$ for the radiances correspond to the relative values of $\overline{\delta}$ for the estimated fluxes. This suggests that a high variability in one of these two quantities implies a high variability in the other. Furthermore, it can be seen that the LW

14

TABLE 2.1.1 Mean values of $\delta = \Delta\bar{m} - 2\sigma/\sqrt{N}$, n(+) and n(-) for the SW and LW radiances and estimated fluxes. SW are divided according to solar zenith angle, viewing angle and latitude bins as well as scene type while LW are divided according to viewing angle and latitude bins only. Data are from ERBS April, 1985.

	I_{sw}	F_{sw}	I_{lw}	F_{lw}
$\bar{\delta}$ (in Wm^{-2})	2.67	6.94	0.39	1.14
n(+)	500	512	83	85
n(-)	99	87	23	21

TABLE 2.1.2 Same as Table 2.1.1 for ERBS November, 1984 data.

	I_{sw}	F_{sw}	I_{lw}	F_{lw}
$\bar{\delta}$ (in Wm^{-2})	1.57	4.80	0.52	1.60
n(+)	497	491	85	84
n(-)	117	123	12	13

TABLE 2.1.3 Same as Table 2.1.1 for NOAA-9 April, 1985 data.

	I_{sw}	F_{sw}	I_{lw}	F_{lw}
$\bar{\delta}$ (in Wm^{-2})	1.24	3.99	0.33	1.04
n(+)	318	320	115	114
n(-)	114	112	20	21

$\bar{\delta}$'s are smaller than the SW $\bar{\delta}$'s since the variability of the SW data is more important. Lower values of the $\bar{\delta}$'s for NOAA-9 indicate less variability in the data from that satellite.

Direct examination of the ERBE data also reveals statistical dependence. Figure 2.1.1 gives the mean value of the SW radiance versus the number of data N from the ERBS April 14th, 1985 data set. The radiances are for $0° \leq \theta \leq 15°$, $0° \leq \theta_o \leq 25.8°$, all ϕ and latitudes $0° \leq \lambda \leq 30°$ N and are taken consecutively. The + sign represents the mean value of I_{sw} at each value of N being a multiple of 10. The solid line shows the percentage of the last 10 data added to the mean that were overcast (95% to 100% cloudiness) and the dashed line shows a similar percentage for the clear ocean scenes (0% to 5% cloudiness). The first 100 data are dominated by clear sky data and $\bar{I}_{sw}$ has a low value (about 40 W m^{-2} sr^{-1}). The first sign of overcast data appears after N = 200. $\bar{I}_{sw}$ increases by 15 W m^{-2} sr^{-1} when adding only 50 new data. From N = 360 to N = 580 all consecutive data correspond to overcast scenes and $\bar{I}_{sw}$ doubles by increasing steadily. For N larger than 600 the mean tends to stabilize only because the satellite is viewing a large partly cloudy area. Even for over 1300 data, $\bar{I}_{sw}$ can still fluctuate when the high values of overcast SW radiances are encountered. The value of $\bar{I}_{sw}$ eventually stabilizes for N greater than several thousand.

This figure clearly shows that the data are statistically dependent. Picking up as much as a hundred consecutive data is not enough to determine the real mean value of the physical quantity measured by the satellite, even if their standard deviation σ is small, because all the data can represent the same type of target.

ERBS APRIL 1985
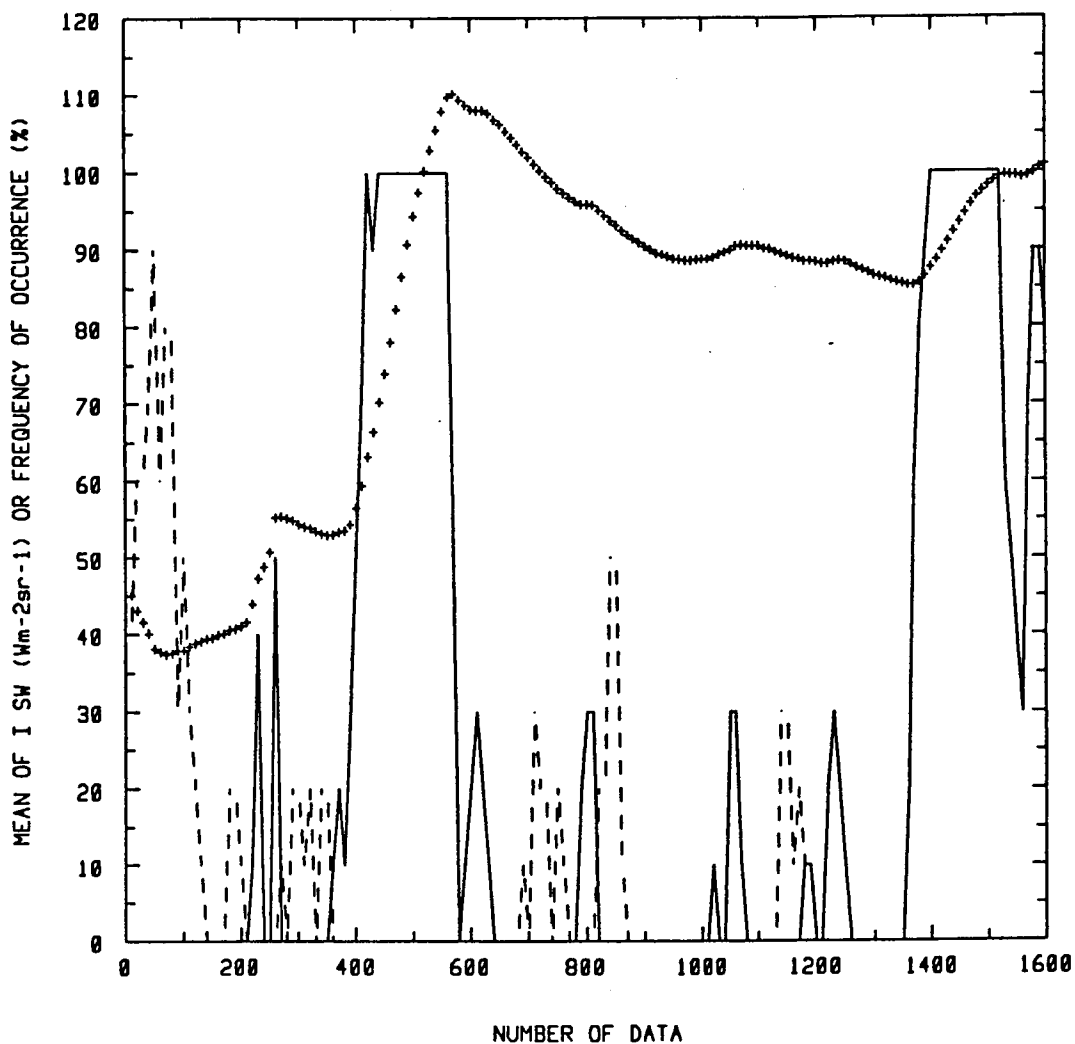
+   mean radiances for N consecutive measurements

———— frequency of overcast scenes in previous 10 values

- - - - - frequency of clear ocean scenes in previous 10 values

FIG. 2.1.1 Mean value of the SW radiance and frequency of occurrence of the clear ocean and overcast scene types. Data are from ERBS April the 14th, 1985 and for $0° \leq \theta \leq 15°$, $0° \leq \theta_0 \leq 25.8°$ and $0° \leq \lambda \leq 30°N$.

2.2 Autocorrelation versus distance

From the preceding section it was shown that taking several consecutive satellite radiance measurements does not necessary lead to the right value of the mean of the physical quantity studied because the measurements, being strongly dependent, are similar. It would seem that it is not useful to pick up two consecutive data since they generally contain similar information. This observation suggests that uniformly sampling the data set in order to collect a fraction of it would lead to the same results as if all the data were taken. Separation between data would tend to give them a statistically independent behaviour. Applying that strategy would also reduce computer time and memory space used during processing.

A study of the autocorrelation versus physical distance on the Earth's surface was therefore conducted in order to find a quantitative separation between two satellite measurements so that they become more independent. Let us define an arbitrary path X on the Earth's surface characterizing the position of the measurement M(X). If D is the distance separating the pairs of measurements to be studied, the linear autocorrelation coefficient is defined as

$$R(D) = \frac{\sigma(X, X + D)}{\sigma(X)\ \sigma(X + D)} \qquad (2.1)$$

where $\sigma(X, X + D)$ is the covariance defined as

$$\sigma(X, X + D) = \frac{1}{N} \sum_{i=1}^{N} [M_i(X) - \overline{M}(X)] \cdot [M_i(X+D) - \overline{M}(X+D)] \qquad (2.2)$$

18

and where $\sigma(X)$ is the standard deviation defined as

$$\sigma(X) = \left[\frac{1}{N} \sum_{i=1}^{N} [M_i(X) - \bar{M}(X)]^2 \right]^{1/2} \qquad (2.3)$$

The absolute value of R is never larger than 1 and R is positive for correlated data pairs, negative for anticorrelated pairs and zero for totally uncorrelated data. R is calculated for different values of the separation distance D and is plotted for different categories of data sets.

The study is done for the ERBE scanner radiance measurements which are classified according to wavelength, θ_o, ϕ, and λ bins. Wavelength bands are SW and LW ERBE broadbands, solar zenith angle θ_o is divided in 10 equal μ_o bins such that bin number 1 is for $0.9 \leq \mu_o \leq 1.0$ or $0° \leq \theta_o \leq 25.8°$, etc... This is done because the solar input depends on μ_o. Relative azimuth ϕ is divided in three categories : "Sun in front" for $330° \leq \phi \leq 360°$ or $0° \leq \phi \leq 30°$ (forward scatter), "Sun in back" for $150° \leq \phi \leq 210°$, "Sun on sides" for $30° \leq \phi \leq 150°$ or $210° \leq \phi \leq 330°$. There are four categories for the latitude λ : low-latitudes for $0° \leq \lambda \leq 30°$ North or South and mid-latitudes for $30° \leq \lambda \leq 60°$ North or South. A better latitudinal resolution is used for some LW studies and will be described later.

The linear correlation coefficient R is plotted against distance along or across satellite track defined as follows. The satellite track is the intersection of the plane containing the satellite orbit with the Earth's surface or, in other words, the path the satellite generates when looking directly towards the centre of the planet. The distance

19

along-track is then defined to be the distance on the Earth separating two points on the satellite track or on a path parallel to it. Calculation showed that two consecutive ERBS or NOAA-9 satellite data lying along-track are separated by 27 kilometres on the Earth's surface. This along-track separation shows little variation up to viewing angles of the order of $45°$.

The distance across-track is defined to be the distance separating two points on Earth lying on a path perpendicular to the along-track direction i.e. the path the scanner instrument is looking at. This scanline contains 62 pixels that are not uniformly separated because of the curvature of the Earth. For ERBS, calculation gave a separation value of 22 kilometres for two consecutive across-track pixels at a viewing angle of $0°$ up to a value of 40 kilometres for a viewing angle of $45°$. For NOAA-9, since its altitude is higher, this separation is larger and varies from 32 to 60 kilometres for a viewing angle varying respectively from a value of $0°$ to $45°$.

The next sections will present results of the autocorrelation coefficient R versus distance along- or across-track.

2.2.1   Results from ERBS April 1985 data

Results presented in this section are restricted to $0° \leq \theta_o \leq 25.8°$ (or $0.9 \leq \mu_o \leq 1.0$), ϕ being for the "Sun on sides" case and to $0° \leq \lambda \leq 30°$ N. There are five days of data processed (the 16th to the 20th of April).

a)   R *along-track dependence on viewing angle*

Figure 2.2.1 shows the correlation coefficient R along-track versus viewing angle, negative angles corresponding to the scanner results to the right with respect to the satellite motion. The upper solid and dashed lines show these correlations for the 1st and 4th neighbour i.e. for the pairs of data that are 1 or 4 scanlines apart. The lower dashed line recalls the shape of the surface ratio defined earlier.

It is clear from that figure that the value of R along-track increases with viewing angle. This effect could be explained by the fact that the dependence of the angular distribution function on cloud geometry weakens with increasing viewing angle up to a value of $\theta = 60^{\circ}$ (Davies, 1984). Consequently, measurements taken at larger viewing angles will tend to be more similar hence an increase in the value of R with θ. This dependence could also be due to the increasing area viewed with viewing angle but it is not obvious since the effect takes place even for small values of the viewing angle where the variation of the surface ratio is not too important. This effect was observed using any SW or LW data from either ERBS or NOAA-9 data sets.

b)   R *along-track for SW and LW*

Figure 2.2.2 shows the correlation coefficient R versus the along-track distance for the 31st radiance measurements of a scanline i.e. near $\theta = 0^{\circ}$. The solid line is for the SW data and the dashed line is for the LW data.

Two important observations can be made. Data separated by a distance of about 2000 km seem to be uncorrelated. This is not too
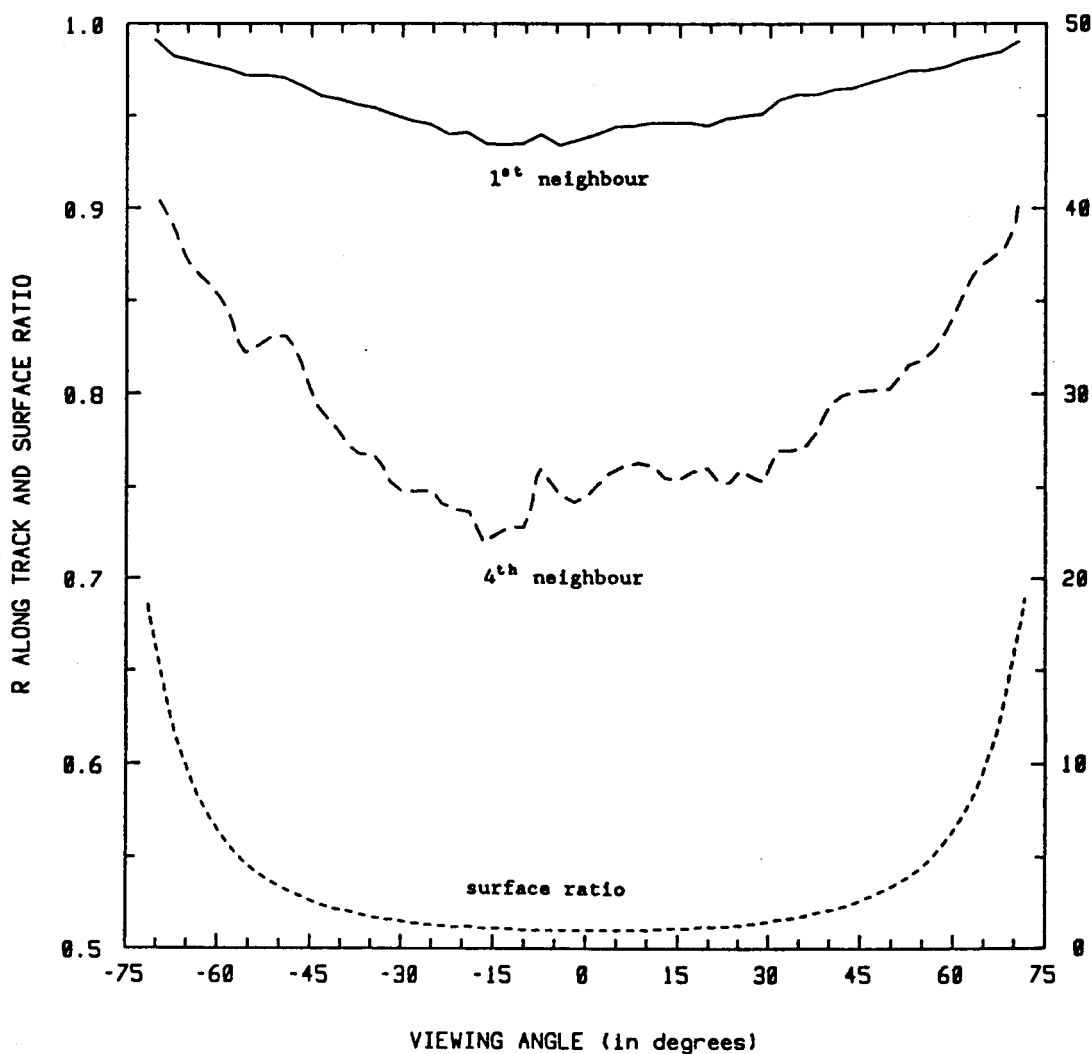
FIG. 2.2.1 SW autocorrelation coefficient along satellite track and surface ratio versus viewing angle. Values of R are given on the left y-axis and values of S are given on the right y-axis. Data are from ERBS April the 16th to the 20th, 1985 and for $0° \leq \theta_o \leq 25.8°$, Sun on sides and $0° \leq \lambda \leq 30°N$.

ERBS APRIL 1985

FIG. 2.2.2 SW and LW autocorrelation coefficients for the 31st scan measurements versus distance along satellite track. Solid line is for SW and dashed line is for LW. Data are from ERBS April the 16th to the 20th, 1985 and for $0° \leq \theta_o \leq 25.8°$, Sun on sides and $0° \leq \lambda \leq 30°N$.

surprising since this value is of the order of magnitude of the synoptic scale. It is also clear that the SW measurements decorrelate faster than the LW measurements, the value of R reaching 0.5 at a distance of 370 km for SW and 740 km for LW. This is due to the fact that the reflection of SW radiation depends on a larger number of degrees of freedom than the LW emission. The LW radiation depends mostly on temperature and cloud versus no-cloud state while the SW reflected radiation can depend on surface type and cloud type as well. The reflection of the SW radiation is complex because the distance to which this radiation penetrates a scattering and absorbing medium before being absorbed is much greater than for the LW radiation (Coakley and Davies, 1986). Furthermore, since clouds can have different shapes and sizes and can contain different populations of water and/or ice droplets, one can easily imagine that the probability of two separate SW radiance measurements being similar is smaller than for two LW measurements ; hence the faster decorrelation for SW coefficient R.

c)   R *across-track for the SW and LW*

Figures 2.2.3 and 2.2.4 represent R against the across-track separation distance. Again the solid line is for the SW data and the dashed line corresponds to the LW data.

The origin of the coordinates in Fig. 2.2.3 is chosen to be at the 31st measurement of a scanline. Again it can be observed that SW radiance measurements decorrelate faster than the LW measurements with R = 0.5 at a distance of 250 km for SW and 640 km for LW. In this figure the tails of the across-track correlation curves are different from the previous along-track ones. They show less tendency to reach the zero
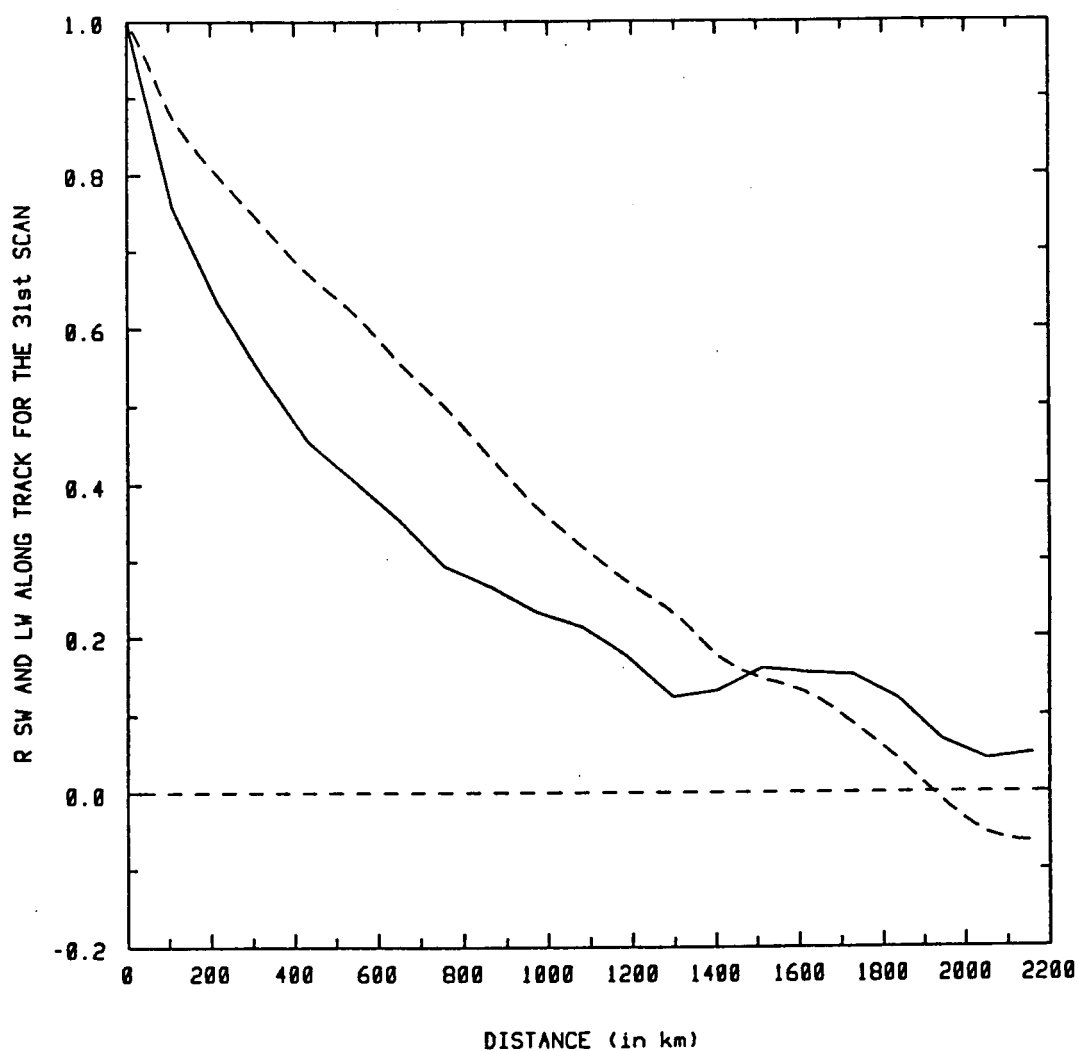
24
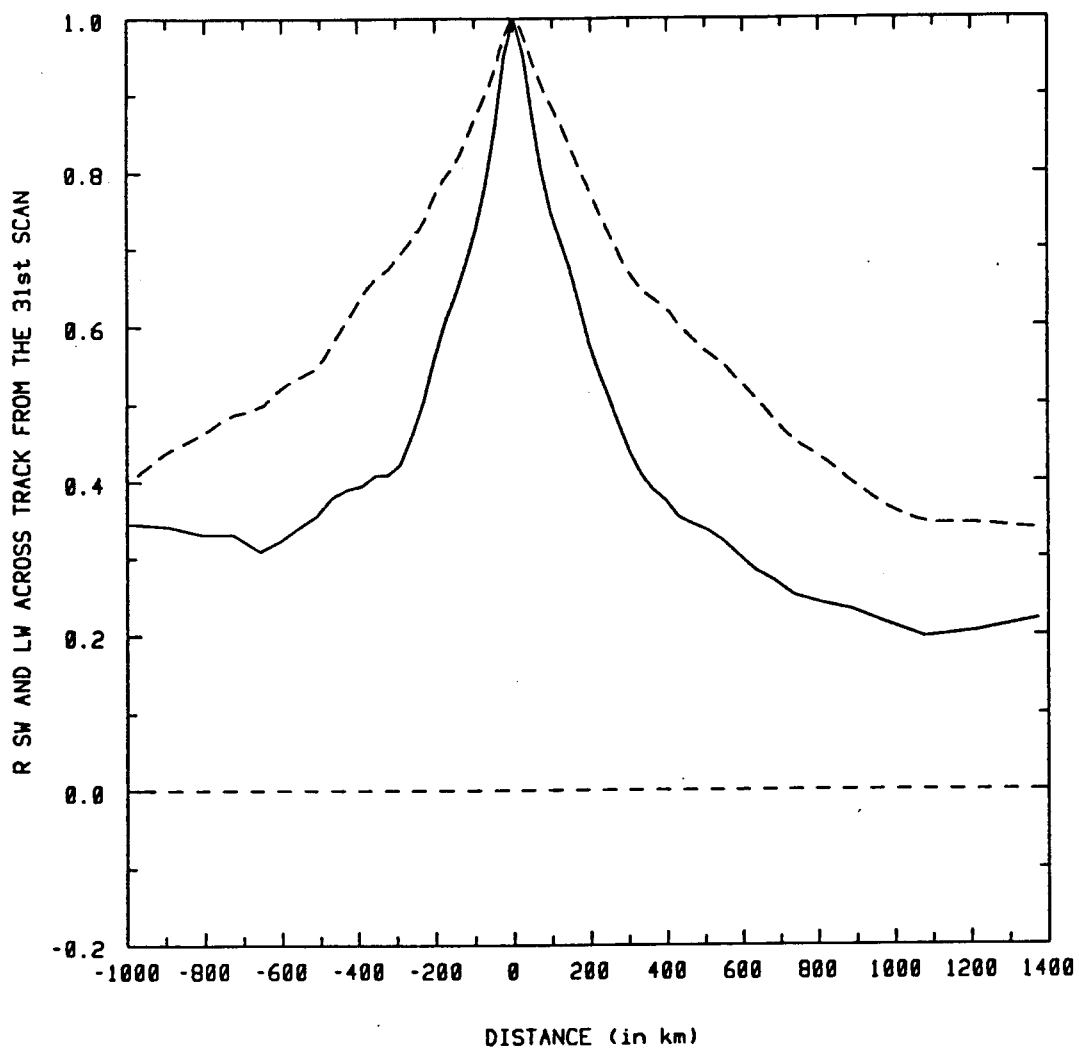
ERBS APRIL 1985

FIG. 2.2.3 SW and LW autocorrelation coefficients from the 31st scan measurements versus distance across satellite track. Solid line is for SW and dashed line is for LW. Data are from ERBS April the 16th to the 20th, 1985 and for $0° \leq \theta_o \leq 25.8°$, Sun on sides and $0° \leq \lambda \leq 30°N$.

ERBS APRIL 1985
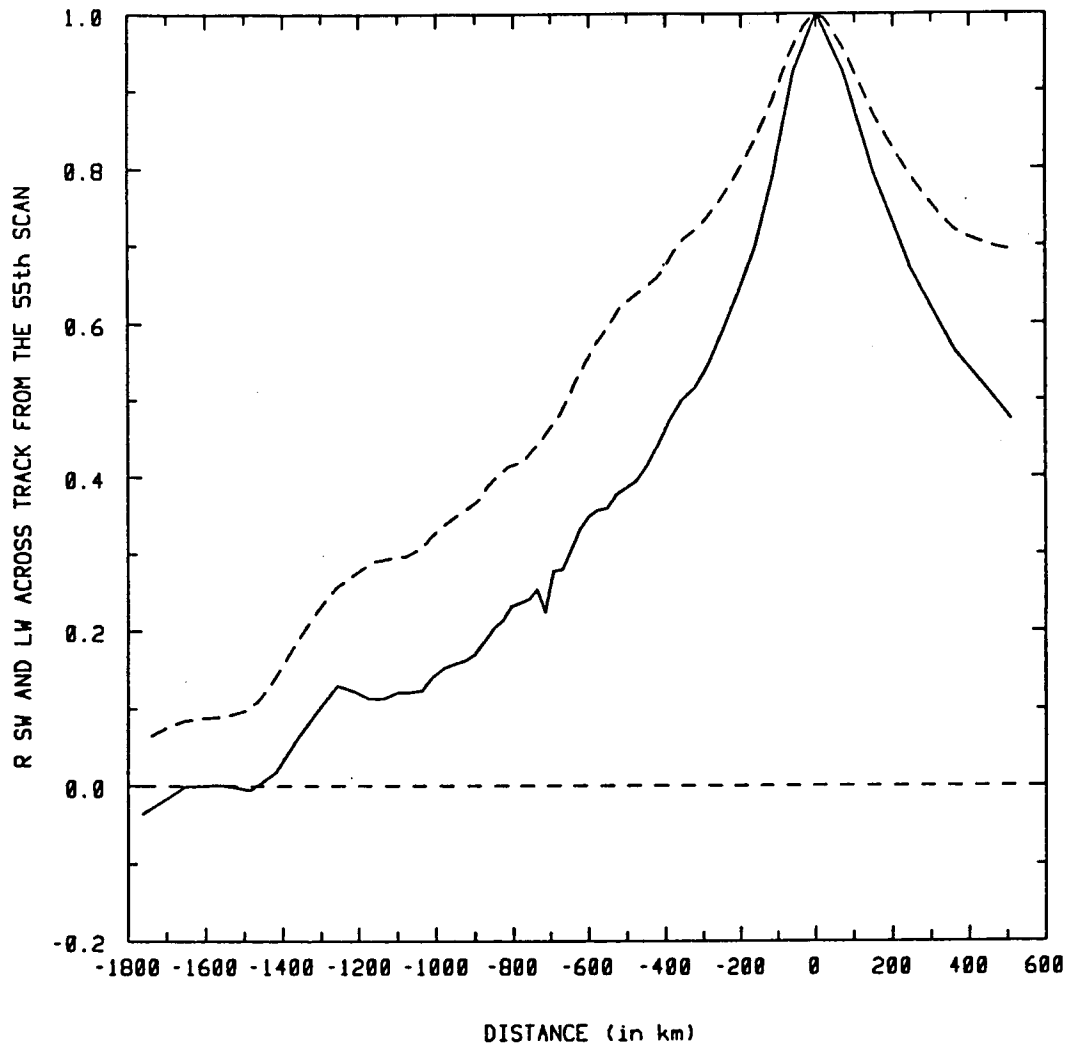
FIG. 2.2.4 Same as Fig. 2.2.3 with the autocorrelation coefficients from the 55th scan measurements.

26

line. The explanation comes from the fact that, as the scanner instrument looks away from nadir, the area viewed becomes larger. Consequently, the measurements on a same scanline far away from satellite track will tend to be similar hence a smaller slope at the tail of the across-track R curve.

This is in agreement with what is shown in Fig. 2.2.4. It is similar to the previous one except for the origin which is now chosen to be at the 55th measurement of a scanline (i.e. the left wing of the scanline from the satellite point of view). The left tails of the curves are towards nadir where the area viewed does not vary much with viewing angle and we observe it reaches smoothly the zero line. The peak of that figure is also wider than the peak of Fig. 2.2.3 again because adjacent data away from nadir tend to be more similar due to the larger area viewed. R now reaches 0.5 at distances of 480 km and 320 km respectively to the right and to the left of the peak, the larger value of these two correlation distances pointing towards the direction of larger area effect.

d)   *Comparison between along- and across-track SW R*

Figure 2.2.5 shows both the along- and across-track SW R against distance with respectively the solid and dashed line. One more day of data (April 21st) was added to reduce noise in the tail part of the across-track R curve. The distance to half correlation where R – 0.5 is now 280 km, a value less than the one from the previous along-track R curve but still within the uncertainty of the curves (see the discussion on the uncertainty in section 2.2). The two curves are extremely similar up to 600 km where the surface ratio begins to increase rapidly (see

27
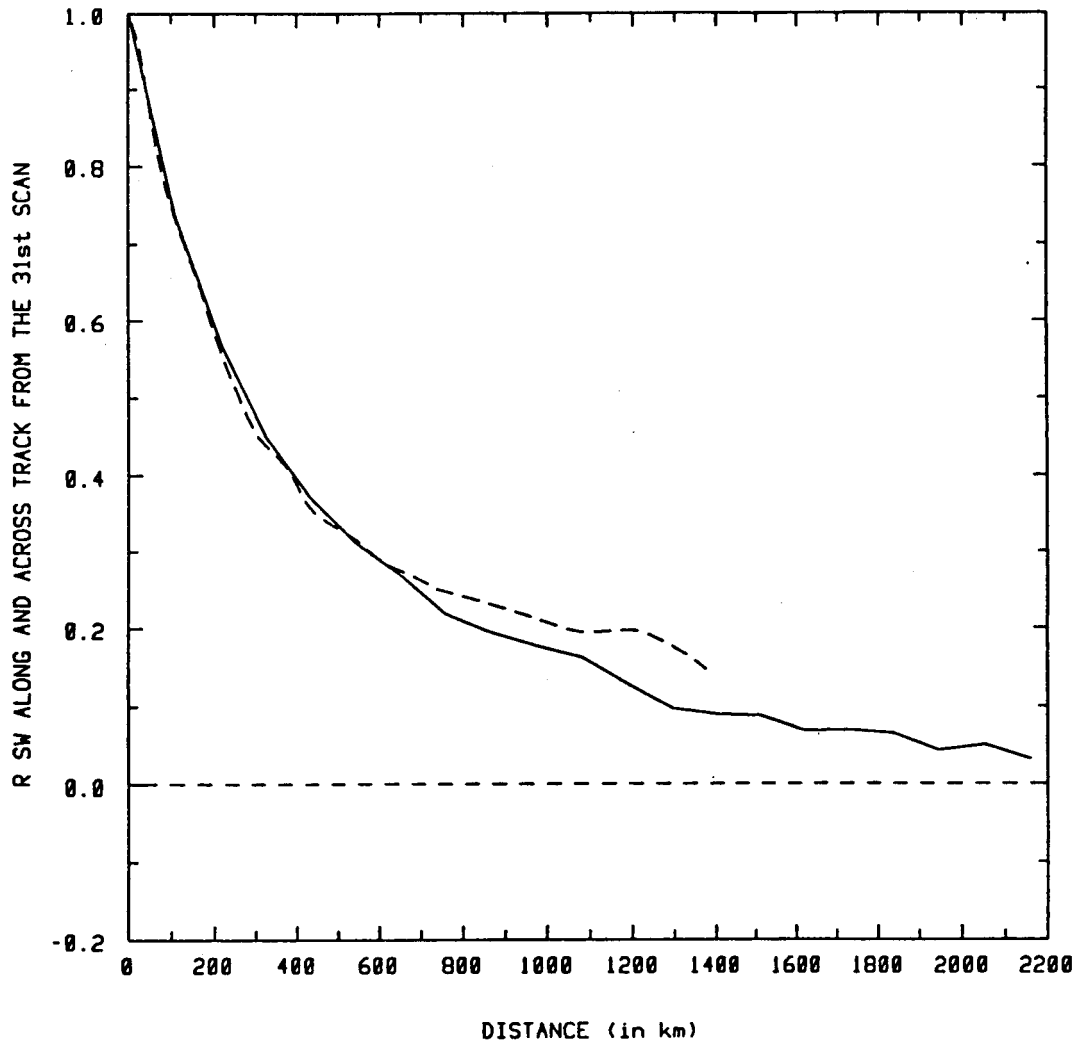
ERBS APRIL 1985

FIG. 2.2.5 SW along- and across-track autocorrelation coefficients from the 31st scan measurements versus distance. Solid line is for along-track R and dashed line is for across-track R. Data are from ERBS April the 16th to the 21st, 1985 and for $0° \leq \theta_o \leq 25.8°$, Sun on sides and $30°S \leq \lambda \leq 30°N$.

ERBS APRIL 1985
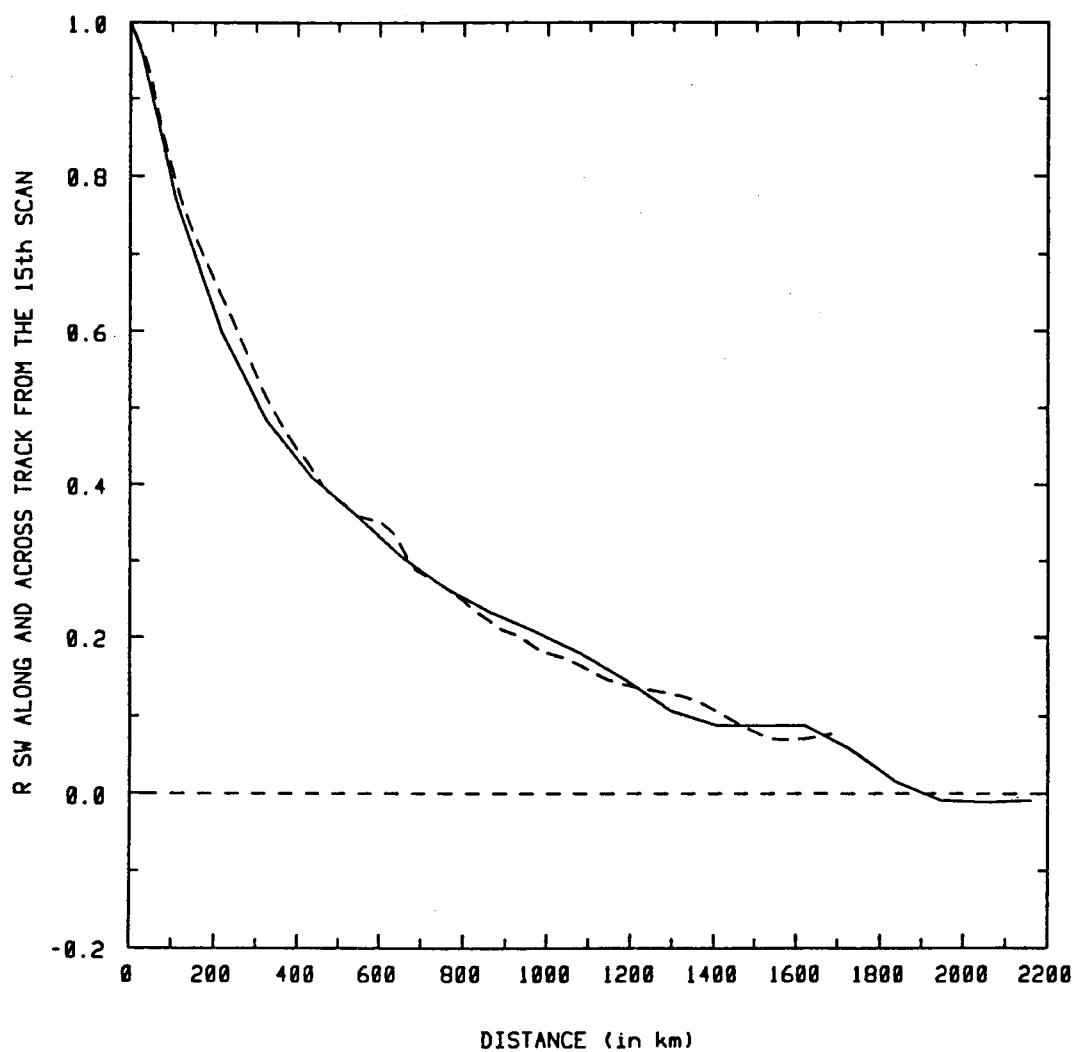
FIG. 2.2.6 Same as Fig. 2.2.5 with the autocorrelation coefficients from the 15th scan measurements.

Fig. 1.4.1). Afterwards the across-track R curve has a higher value than the along-track one. This could be due to statistical noise or to the area effect on the across-track R curve. Looking at Fig. 2.2.6 reinforces the conclusions from the previous figure. It shows again the along- and across-track SW R but this time from the 15th scan number (right wing of the scanline from the satellite point of view). The across-track R curve is directed towards nadir where the area viewed is about the same for two adjacent across-track pixels. We observe now that the two curves are extremely similar everywhere. The distance to half correlation for the two curves is larger in this case ($\cong$ 320 km) because the area effect is more important near the 15th scan measurement.

It is believed that, for the latitude band studied, the autocorrelation coefficient along-track R is similar to the across-track R for viewing angles not too large ($\theta \lesssim 50°$). It is not sure that this conclusion would still stand if smaller equatorial regions were studied because, in that case, zonal phenomenon like the Inter-Tropical Convergence Zone (I.T.C.Z.) could change the correlations.

e)   *Variation of the along-track R with latitude*

Along-track R for the 31st scan measurement was studied for different latitudes. Figure 2.2.7 gives the value of R versus λ for 27, 108, 540 and 1512 kilometres of along-track separation distance corresponding respectively to the upper, middle and lower curves. The number of latitude bins was doubled for a better resolution (now each 15^{0} latitude bands from the equator). The correlation seems a bit higher for the mid-latitudes at constant separation distance. This is possibly explained by the fact that the sub-tropical highs are found near

30

ERBS APRIL 1985

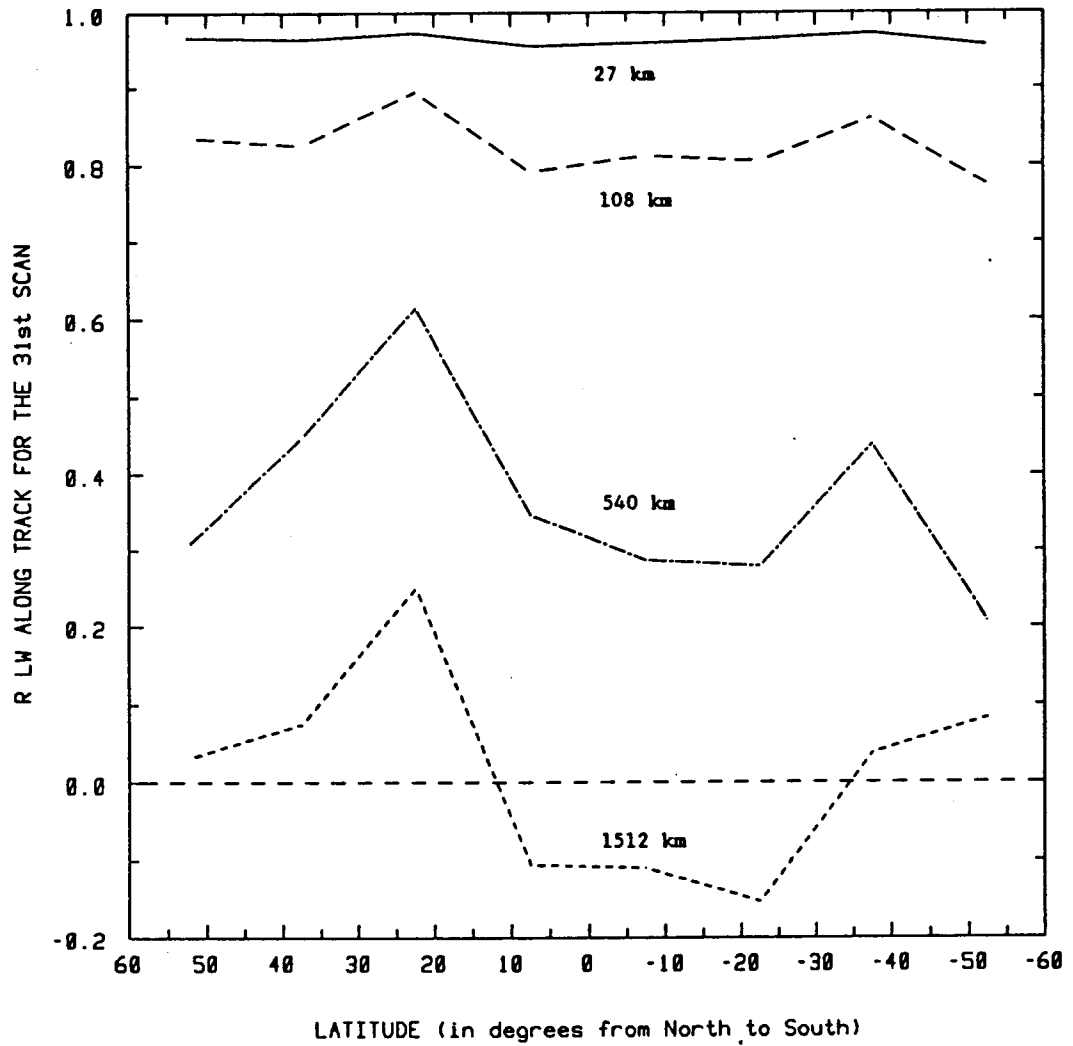FIG. 2.2.7 LW autocorrelation coefficient along satellite track for the 31st scan measurements versus latitude. Results are for along-track distances of 27, 108, 540 and 1512 km. Data are from ERBS April the 16th to the 19th, 1985 and for all θ_o and all ϕ.

$30°$ North and South so that these regions are much more cloud-free, increasing the correlation between neighbouring pixels.

f)   *Varying solar zenith angle*

Previous   results   are   all   for $0.9 \leq \mu_o \leq 1.0$ (i.e. $0° \leq \theta_o \leq 25.8°$). A comparison with another solar zenith angle bin is made on a short along-track separation distance in order to verify if a complete different behaviour is observed. Figure 2.2.8 shows R along-track for the SW data corresponding to two different θ_o bins. The solid line is for $0.9 \leq \mu_o \leq 1.0$ ($0° \leq \theta_o \leq 25.8°$) and the dashed line is for $0.7 \leq \mu_o \leq 0.8$ ($36.9° \leq \theta_o \leq 45.6°$). Sun is on sides. No important differences are observed.

g)   *Varying the relative azimuth*

Changing the relative azimuth ϕ did not seem to affect any correlation coefficient curve studied. This indicates that for large data sets, the results are statistically homogeneous with respect to ϕ. This is also in agreement with results for the albedo shown in a report to the 23rd ERBE team meeting by E. Ahmad and V. Ramanathan.

2.2.2   Results from ERBS November 1984 data

An autocorrelation study was also made for 5 days of the ERBS November 1984 radiance measurements. The main observations are presented here. As before, only the results for $0.9 \leq \mu_o \leq 1.0$ and for Sun on sides are shown. Latitude is now $30°S \leq \lambda \leq 30°N$ to increase data volume.

Figure 2.2.9 illustrates the value of R against along-track separation distance for the November SW and LW measurements. The

ERBS APRIL 1985
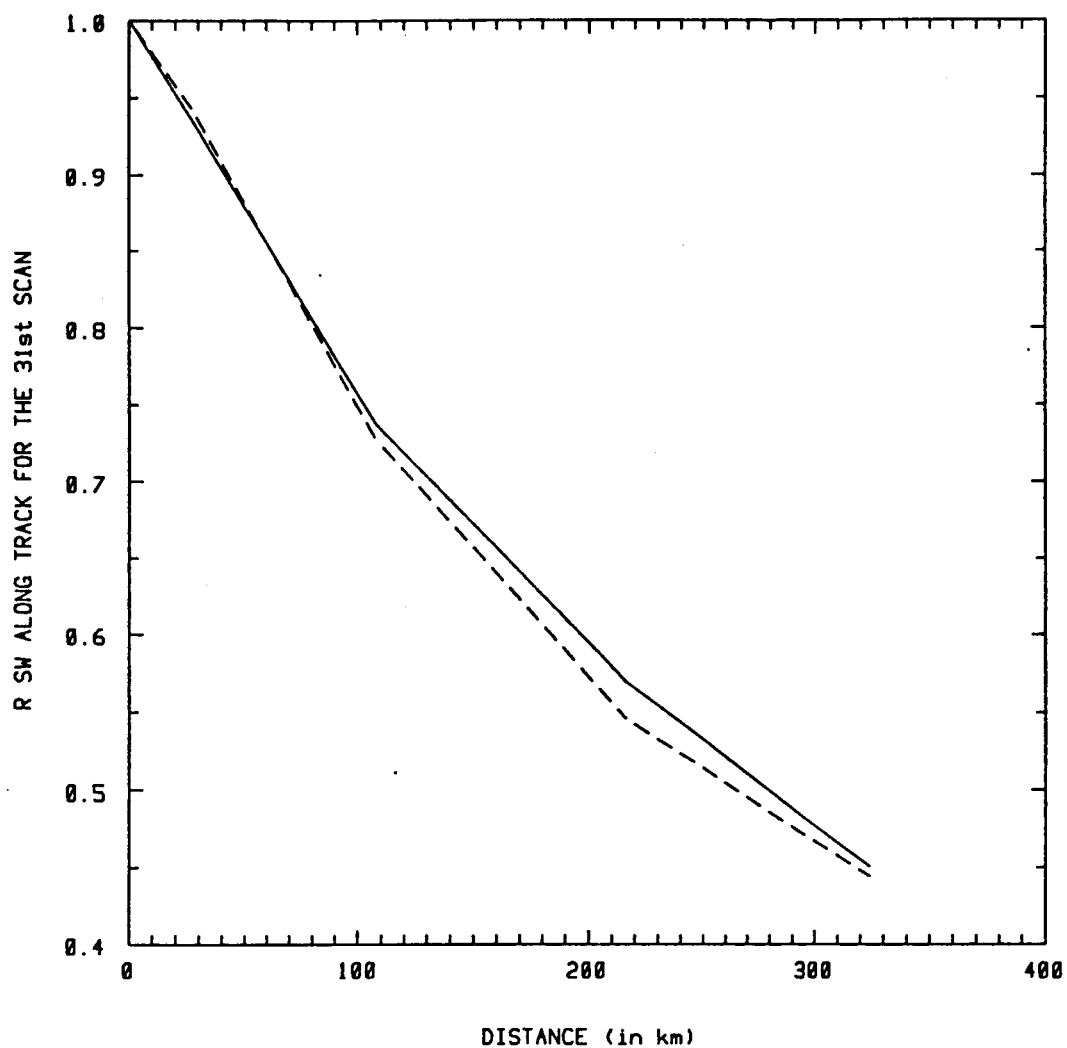
FIG. 2.2.8   Comparison between two SW autocorrelation coefficients for different Sun positions versus distance along satellite track. Solid line is for ERBS April the 16th to the 20th, 1985 with $0° \leq \theta_o \leq 25.8°$ and dashed line is for ERBS April the 11th to the 14th, 1985 with $36.9° \leq \theta_o \leq 45.6°$. Sun is on sides and $30°S \leq \lambda \leq 30°N$.

ERBS NOVEMBER 1984

FIG. 2.2.9 SW and LW autocorrelation coefficients for the 31st scan measurements versus distance along satellite track. Solid line is for SW and dashed line is for LW. Data are from ERBS November the 18th to the 22nd, 1984 and for $0° \leq \theta_o \leq 25.8°$, Sun on sides and $30°S \leq \lambda \leq 30°N$.

ERBS NOVEMBER 1984 AND APRIL 1985
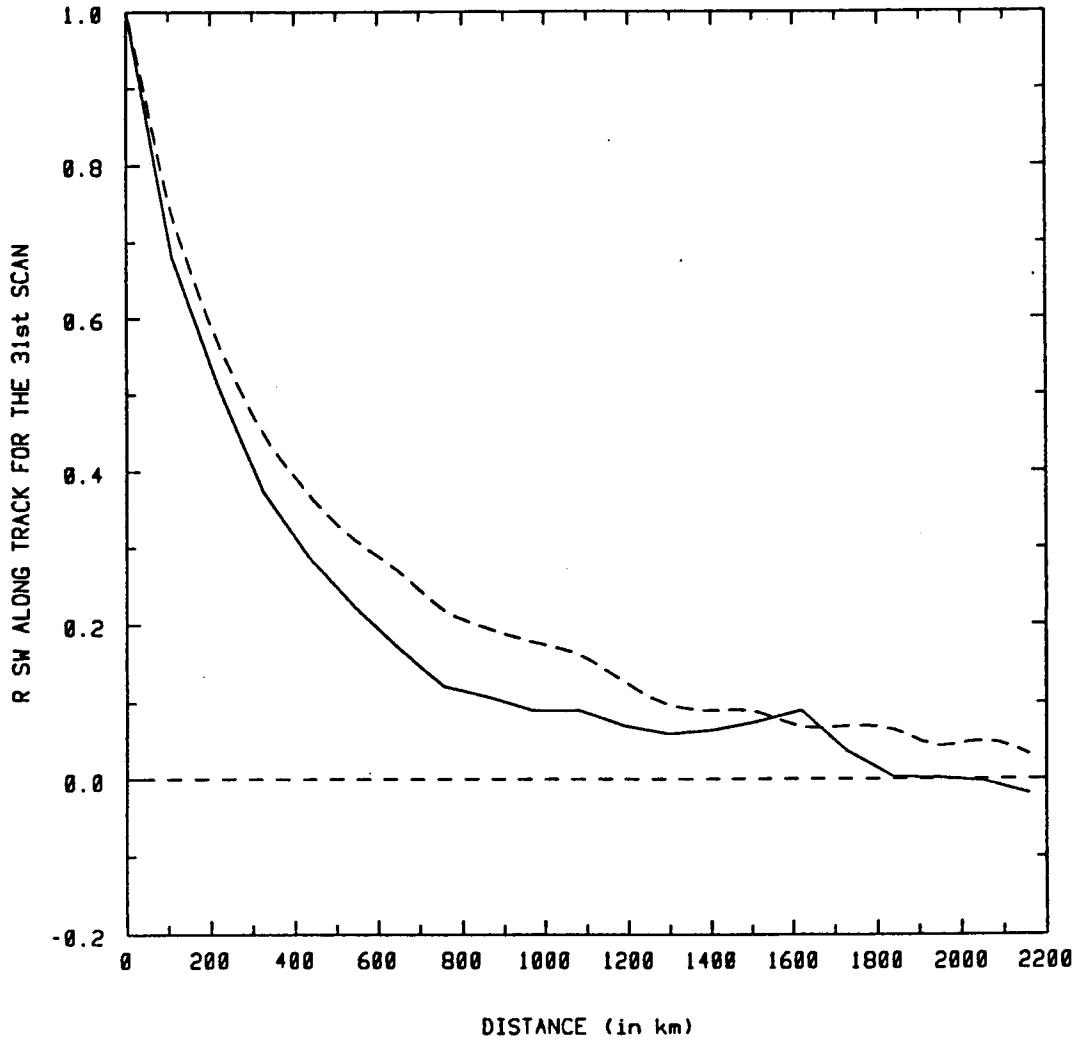
FIG. 2.2.10 SW autocorrelation coefficient for the 31st scan measurements versus distance along satellite track for two different months. Solid line is from ERBS November the 18th to the 22nd, 1984 while the dashed line is from ERBS April the 16th to the 21st, 1985. Data are for $0° \leq \theta_o \leq 25.8°$, Sun on sides and $30°S \leq \lambda \leq 30°N$.

previous conclusion that the SW along-track R decorrelates faster than the LW along-track R still stands for the data of that month. It is also verified for the across-track SW and LW R.

A comparison between ERBS November 1984 and April 1985 results for R along-track is presented in Fig. 2.2.10. The distance to half correlation for November SW data is 220 km, a value slightly smaller than the April value, and is 400 km for the LW data, a value much smaller than the April one. For overhead Sun position in low-latitude regions, the November data appear to decorrelate faster than the April ones, but because of the statistical uncertainty of the curves this difference may not be significant.

2.2.3   Results from NOAA-9 April 1985 data

Radiance measurements from another ERBE satellite were also studied. Since NOAA-9 is a sun synchronous satellite, not every Sun angle is available for the low-latitudes. For that reason, the results shown are for $0.7 \leq \mu_o \leq 0.8$ ($36.9^{\circ} \leq \theta_o \leq 45.6^{\circ}$), Sun on sides and $30^{\circ}S \leq \lambda \leq 30^{\circ}N$.

The first important observation is presented in Fig. 2.2.11 where the values of SW and LW R along-track for the 39th scanline measurements are plotted versus separation distance. The SW R curve decreases more rapidly than the LW R curve as observed earlier with the ERBS data, the distance to half correlation now being 280 km and 360 km respectively for SW and LW, but the difference between these two curves is smaller than the difference between the same curves from ERBS data set. An explanation was not found but a similar observation has been made for R
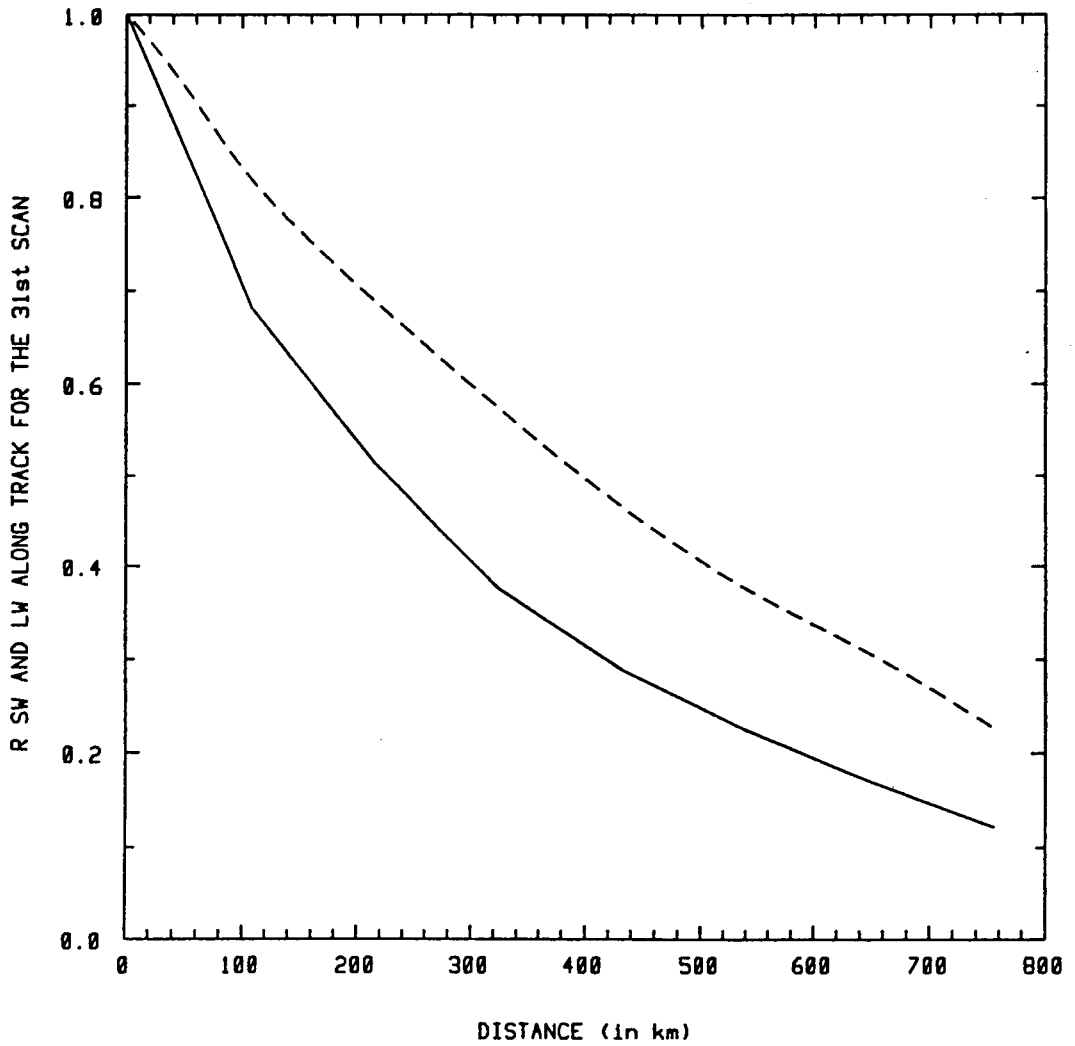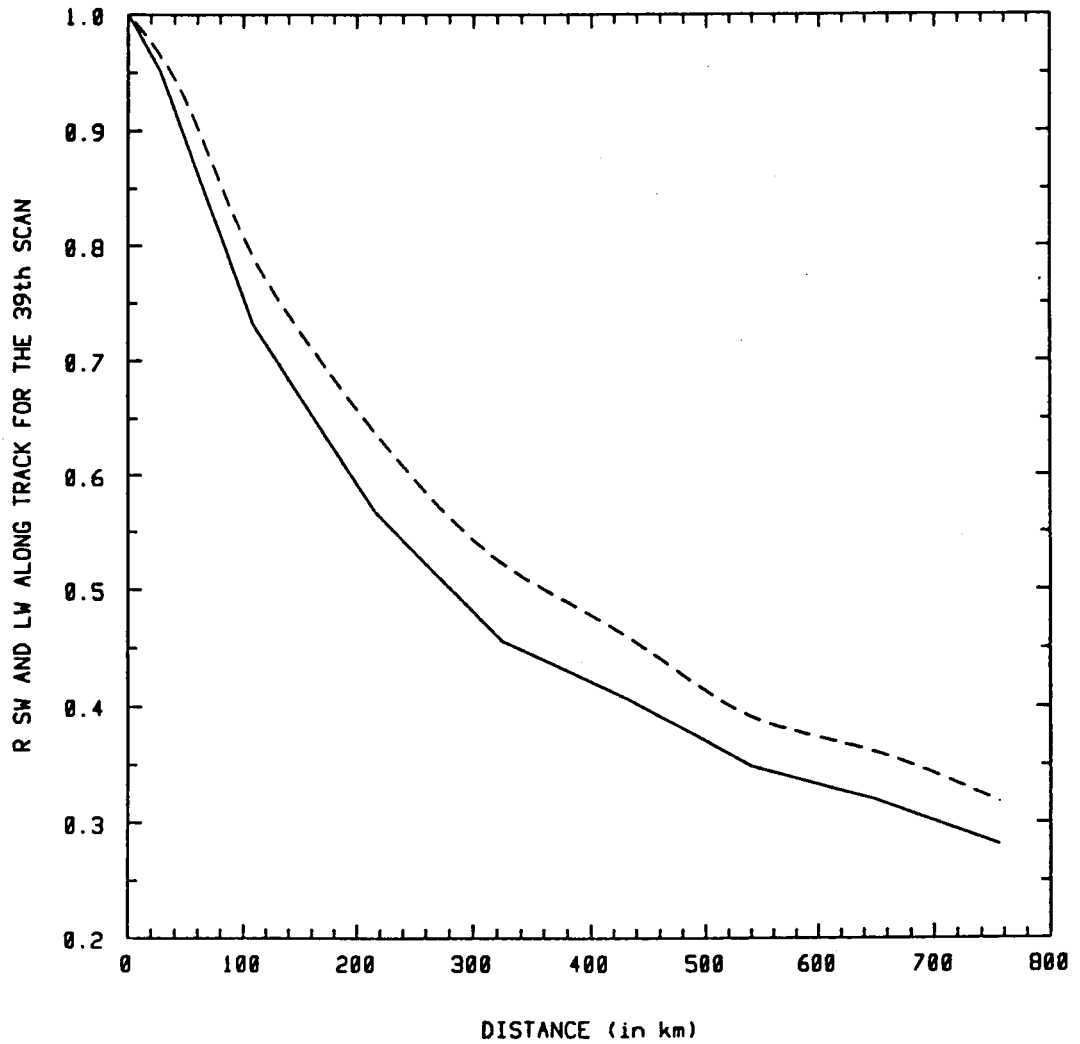
NOAA-9 APRIL 1985

FIG. 2.2.11 SW and LW autocorrelation coefficients for the 39th scan measurements versus distance along satellite track. Solid and dashed lines are for SW and LW respectively. Data are from NOAA-9 April the 11th to the 18th, 1985 and for $36.9° \leq \theta_o \leq 45.6°$, Sun on sides and $30°S \leq \lambda \leq 30°N$.

NOAA-9 AND ERBS APRIL 1985
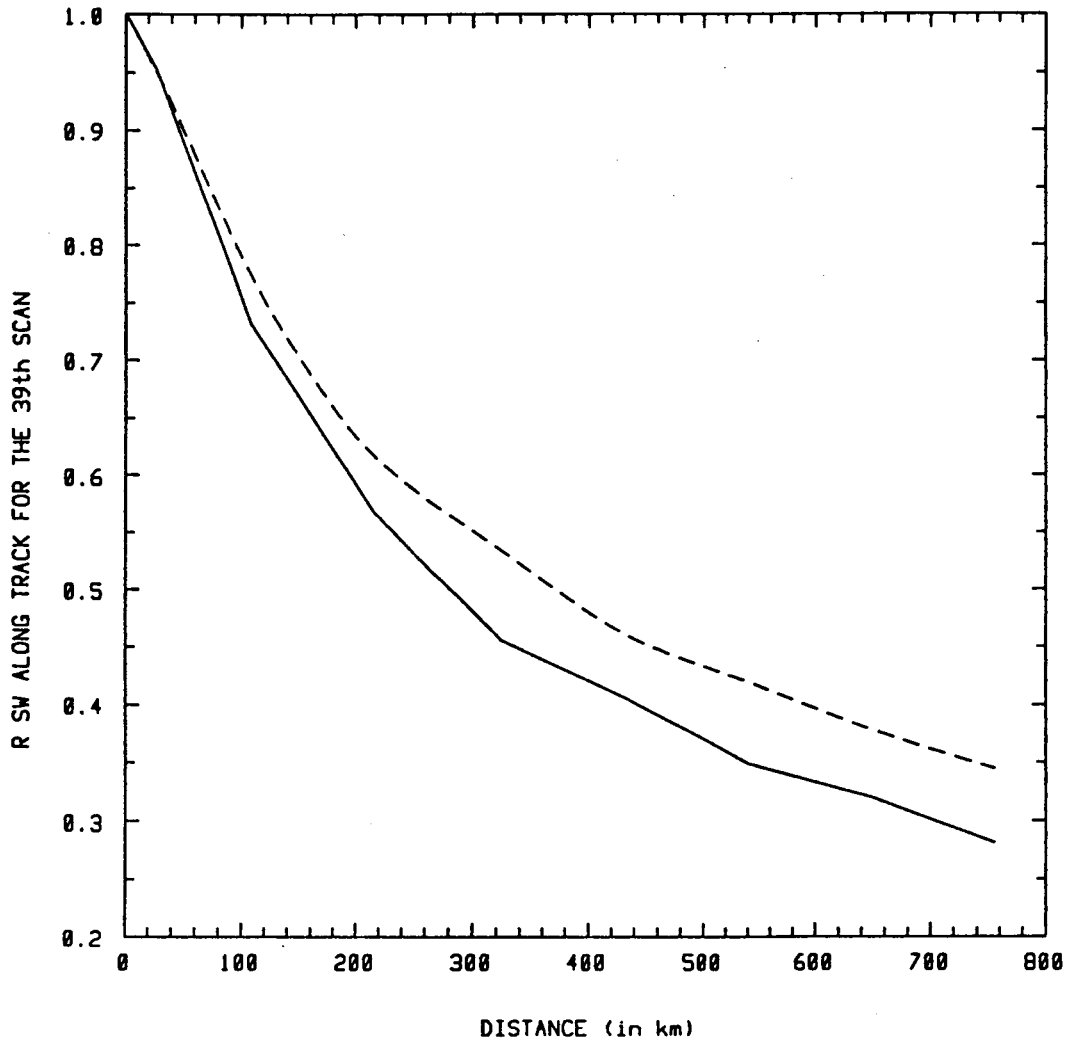
FIG. 2.2.12 Comparison between SW autocorrelation coefficients for the 39th scan measurements versus distance along-track for two ERBE satellites. Solid line is for NOAA-9 and dashed line is for ERBS. Data are from NOAA-9 April the 11th to the 18th, 1985 and from ERBS April the 11th to the 14th, 1985. For both satellites, $36.9° \leq \theta_o \leq 45.6°$ with Sun on sides and $30°S \leq \lambda \leq 30°N$.

NOAA-9 AND ERBS APRIL 1985
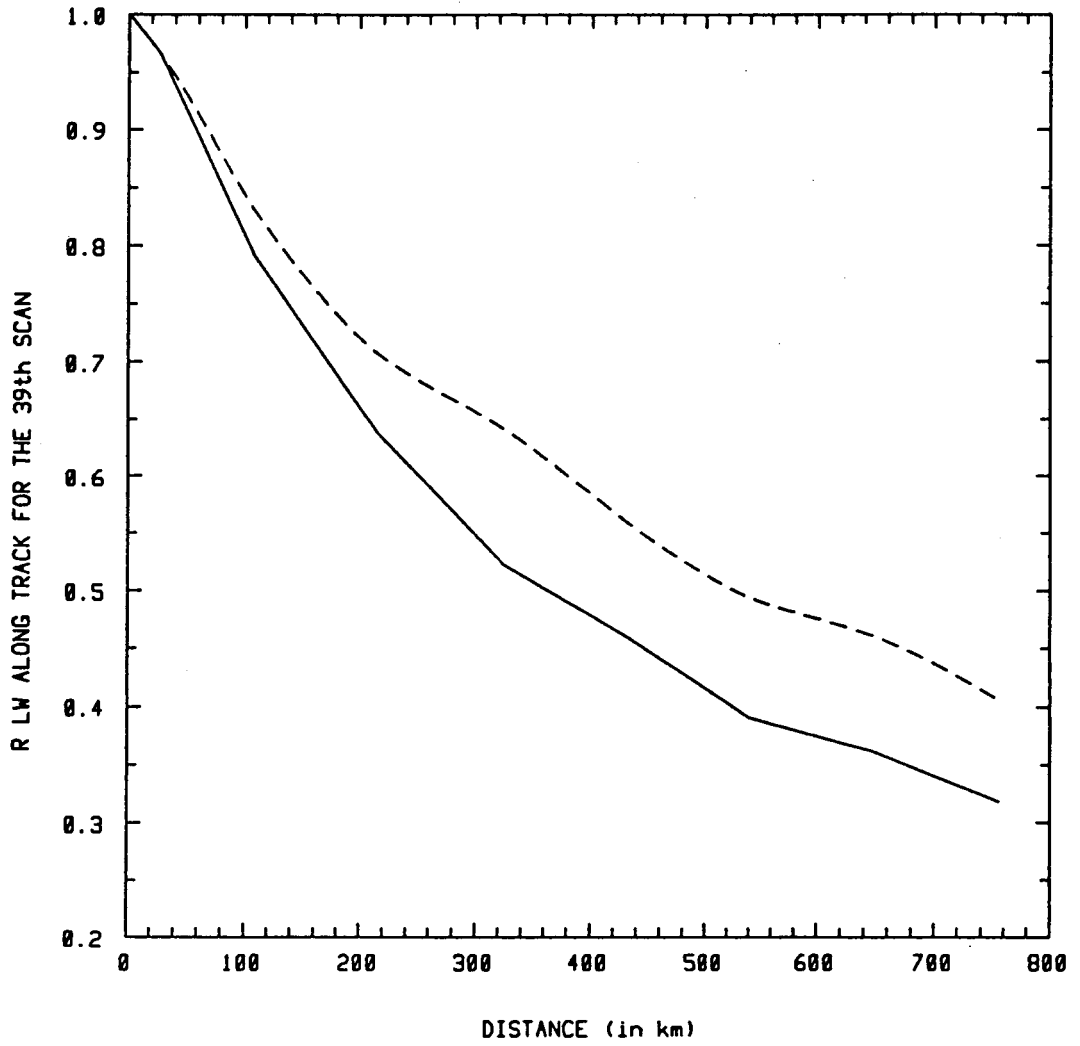
FIG. 2.2.13   Same as Fig. 2.2.12 for the LW data. Solid line is for
NOAA-9 and dashed line is for ERBS.

across-track.

Another important observation is that for almost the same days of April 1985, the SW and LW NOAA-9 data decorrelate more rapidly than the ERBS data. Figures 2.2.12 and 2.2.13 show respectively the SW and LW R along-track curves for NOAA-9 (the solid line) and for ERBS (the dashed line). Difference in the values of the distance to half correlation is of the order of 80 km for SW and 170 km for LW. Statistical noise in the curves could explain this difference since a physical explanation is hard to find.

2.3 Uncertainty in the autocorrelation curves

The autocorrelation curves presented earlier are surely subjet to statistical noise. Estimation of the uncertainty in the curves could certainly reinforce or weaken some conclusions. Two different approaches to estimate this uncertainty are discussed here.

The classical statistical theory provides a first method. It consists in calculating a kind of standard deviation from the statistical data used to derive the autocorrelation coefficient R. This standard deviation is then considered to be the standard error. Using the same definitions as in Section 2.2, it is given as

$$
e = \left\{ \frac{\displaystyle\sum_{i=1}^{N} [M_i(X)]^2 \cdot \sum_{i=1}^{N} [M_i(X+D)]^2 - \sum_{i=1}^{N} [M_i(X) \cdot M_i(X+D)]^2}{(N-2) \cdot \left[\displaystyle\sum_{i=1}^{N} [M_i(X)]^2 \right]^2} \right\}^{1/2}
\tag{2.4}
$$

where N is the total number of data. The origin of this expression will not be explained here and can be found in the literature (Edwards, 1979). The problem with this formula is that it can only be used with statistical independent data sets like most of the formula given by the classical theory. Since ERBE data used to calculate the coefficient R are highly correlated, great care must be taken when interpreting the value of e. The complete summations were used but the value of (N - 2) was changed. From the previous graphs, it can be seen that two sets of data separated by about 1000 km have a correlation below 0.2. A jump of 40 consecutive data for a certain scan measurement number gives approximately that distance. So the formula for the error e was used with (N/40 - 2) instead of the (N - 2) factor.

The calculated results for e that are related to the graphs presented in this chapter vary from less than 0.01 to 0.04 at worst, the larger values always corresponding to the end part of the curve's tail. All LW curves have e less than 0.025.

This method is possibly not adequate since the data used are strongly dependent.

Another very simple method to use is to examine the differences between two curves representing the same type of data. Figure 2.3.1 shows that experiment for NOAA-9 April data with $36.9° \leq \theta_o \leq 45.6°$, Sun on sides and $30°S \leq \lambda \leq 30°N$. The solid line is for the 11th up to the 18th of April while the dashed line is for April 1st to April 8th. The comparison shows a difference of 0.02 at worst for a separation distance less than 600 km, a value of the order of magnitude of the results from the previous calculations.
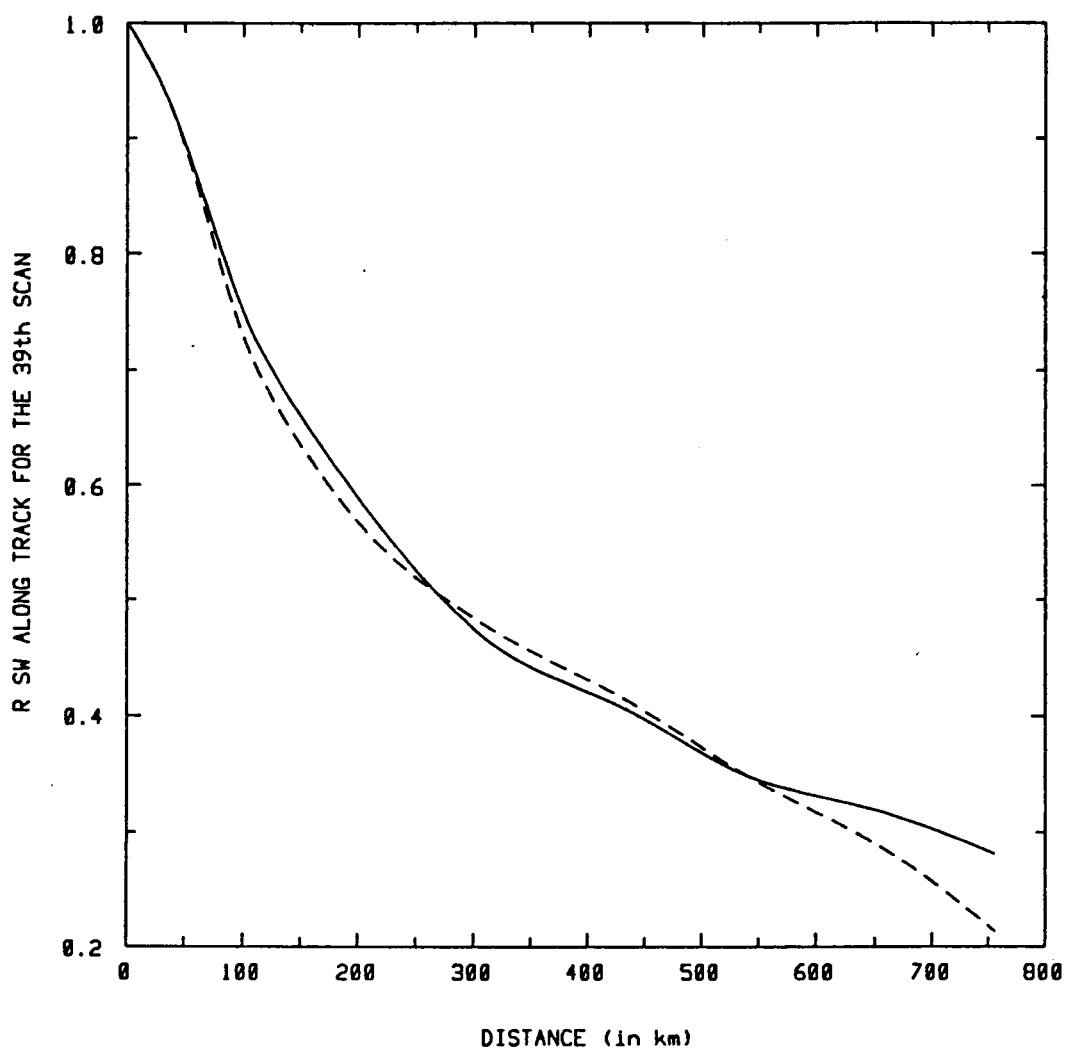
FIG. 2.3.1 Comparison between two NOAA-9 autocorrelation coefficient curves representing similar SW data sets. Solid line is for April the 11th to the 18th, 1985 and dashed line is for April the 1st to the 8th, 1985. Data are for $36.9° \leq \theta_o \leq 45.6°$, Sun on sides and $30°S \leq \lambda \leq 30°N$.

These two methods give at least an idea of the amplitude of the statistical noise of the autocorrelation coefficient curves presented in this chapter.

2.4   A sampling strategy

The purpose of the present chapter was to characterize quantitatively the statistical dependence of the ERBE scanner data. This was accomplished with the use of the autocorrelation coefficient R. It was shown that measurements of adjacent pixels are highly correlated i.e. very similar and a suggestion was to take only measurements that are separated by a certain distance on the Earth's surface in order to give the data a better statistically independent behaviour. The problem is now to find that distance.

One possibility could be to choose the separation distance at which the data are totally uncorrelated i.e. where R approaches zero. It is generally of the order 2000 kilometres. But this corresponds to an extreme case and loses information because R does not reach zero sharply but reaches it very smoothly.

The half value of 0.5 for R could determine the separation distance we are looking for, but a more general procedure is to choose that distance that separates the area under the R curves in two equal parts. This distance is generally between 300 km and 400 km for SW. For LW, it varies from 400 km to 600 km. For the ERBS April 1985 data package, which will be studied in Chapter 3, this separation distance is close to 400 km for SW corresponding approximately to a jump of 16 consecutive scanlines (4 PAT records). Figure 2.4.1 shows the mean value

of the radiances I_{sw} against the number of data for a partly cloudy ocean scene in April. Data have been collected by jumping 16 scanlines. The mean stabilizes rapidly and is well defined for N larger than 100. Comparison with Fig. 2.1.1 is interesting.

It seems a jump of 16 scanlines is appropriate to avoid redundancy of the SW data in order to collect a considerably smaller data volume without losing too much information. Since it is mostly the SW data that will be studied in Chapter 3, the same jump is used for LW in order to pick SW and LW data at the same time. Results of data analysis using this sampling strategy are presented in the next chapter.
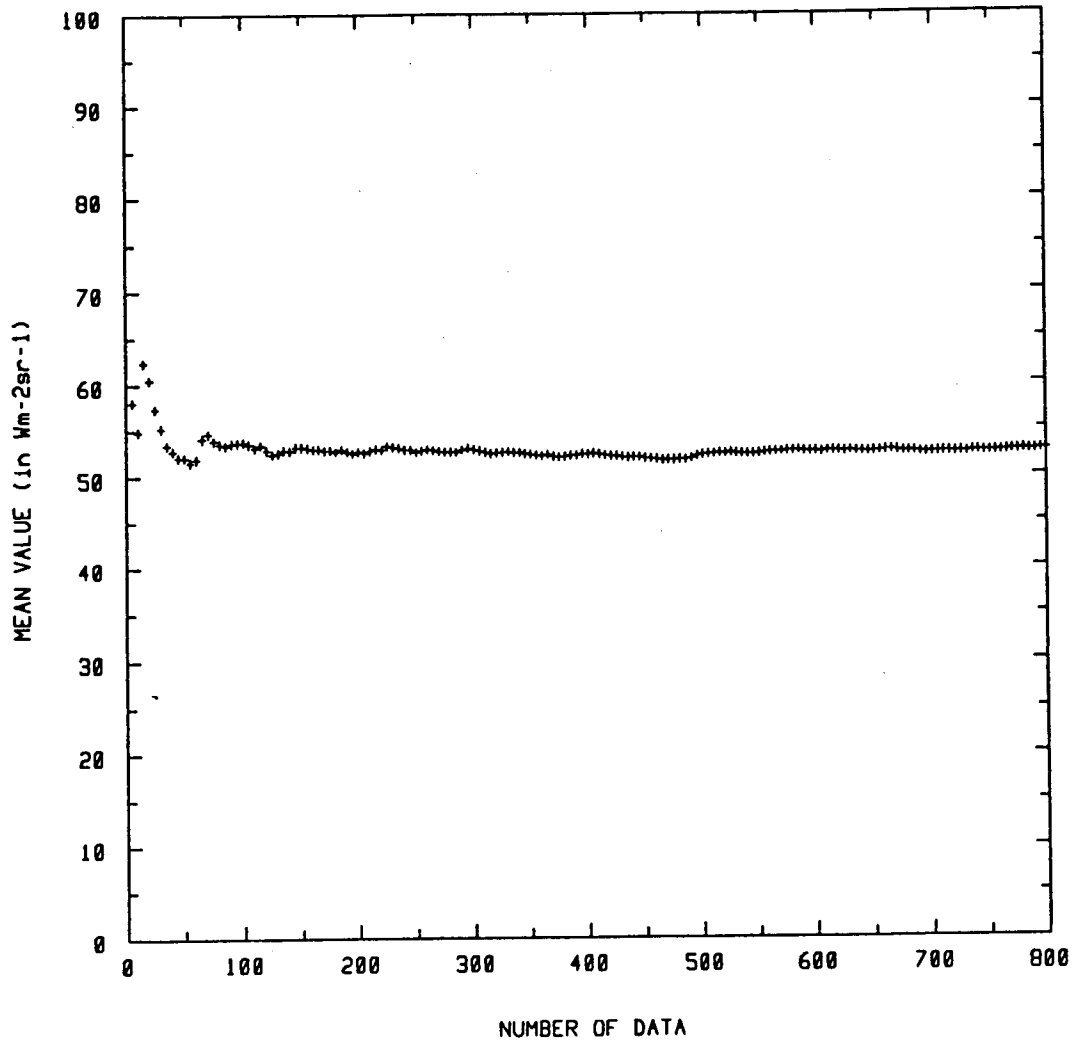
ERBS APRIL 1985

FIG. 2.4.1 Mean value of the SW radiance over a partly cloudy ocean. Data are from ERBS April the 13th, 1985 and are collected jumping scanlines as suggested.

Chapter 3

Scanner data analysis

Having a better resolution than the non-scanner instrument as well as providing data for different viewing angles, the ERBE scanner instrument is useful for climatological studies. Applications of the ERBE scanner data and the sampling strategy discussed in Chapter 2 are presented in this chapter. The data used are from ERBS November 1984 and April 1985. As suggested at the end of the previous chapter, measurements are separated by 16 consecutive scanlines or about 430 kilometres.

At first, the diurnal LW measurements are studied since, from Wen (1987), they show much less variability than the SW measurements. A greater attention was given to the SW data analysis.

3.1 Longwave results

3.1.1 LW radiances

LW radiation depends mostly on cloudiness and on temperature, which is related to latitude, and is usually not far from being isotropic. For that matter, the LW radiances from 10 consecutive days of ERBS April 1985 data set were binned according to the cosine of the viewing angle θ ($\mu = \cos\theta$) and latitude λ so that a study of the dependence of I_{lw} on μ can be made for certain latitude bands. μ is divided into 7 bins, 6 being equal for $0.4 \leq \mu \leq 1.0$ ($0° \leq \theta \leq 66.4°$) with $\Delta\mu = 0.1$ and the 7th bin representing $0 \leq \mu \leq 0.4$ ($\theta \geq 66.4°$). The latitude λ was divided into $10°$ bands starting from the equator.

Figures 3.1.1 and 3.1.2 show the values of $\overline{I}_{lw} \cdot \overline{\mu}$ against the mean $\overline{\mu}$ of each viewing angle bins for respectively the $0° - 10°$ N and the $30° - 40°$ N latitude bands. The vertical bars give the value of one standard deviation of the mean $(\sigma/\sqrt{N})$ on each side of the curves. Sampling in θ was homogeneous since $\overline{\mu}$ equals the mid-value of each θ bins except the very last one because of the cutoff angle.

The curves are very well behaved and show an almost perfect linear decrease towards zero. The linear behaviour is an indication of isotropy in the LW radiation field for viewing angles not too large ($\theta \lesssim 70°$) since limb darkening could be observed if satellite scanner data were available for very oblique viewing positions.

3.1.2   LW integrated versus estimated fluxes

The ERBE data package provides estimated values of the LW flux based on the radiance measurements and the directional models. The integrated flux is defined to be the value of the flux obtained by integrating the radiances over viewing angle and can be easily calculated for each latitudinal band using

$$F_\lambda = 2\pi \sum_{i=1}^{7} \overline{I}_{\lambda i} \cdot \overline{\mu}_i \cdot \Delta\mu_i \qquad (3.1)$$

where the index i is for the 7 viewing angle bins.

Figure 3.1.3 gives the mean values of the integrated and estimated fluxes for each of the $10°$ latitude bands. Integrated flux could not be calculated for the two $60° - 70°$ North and South bands because no nadir radiances are available from ERBS for these regions.

47
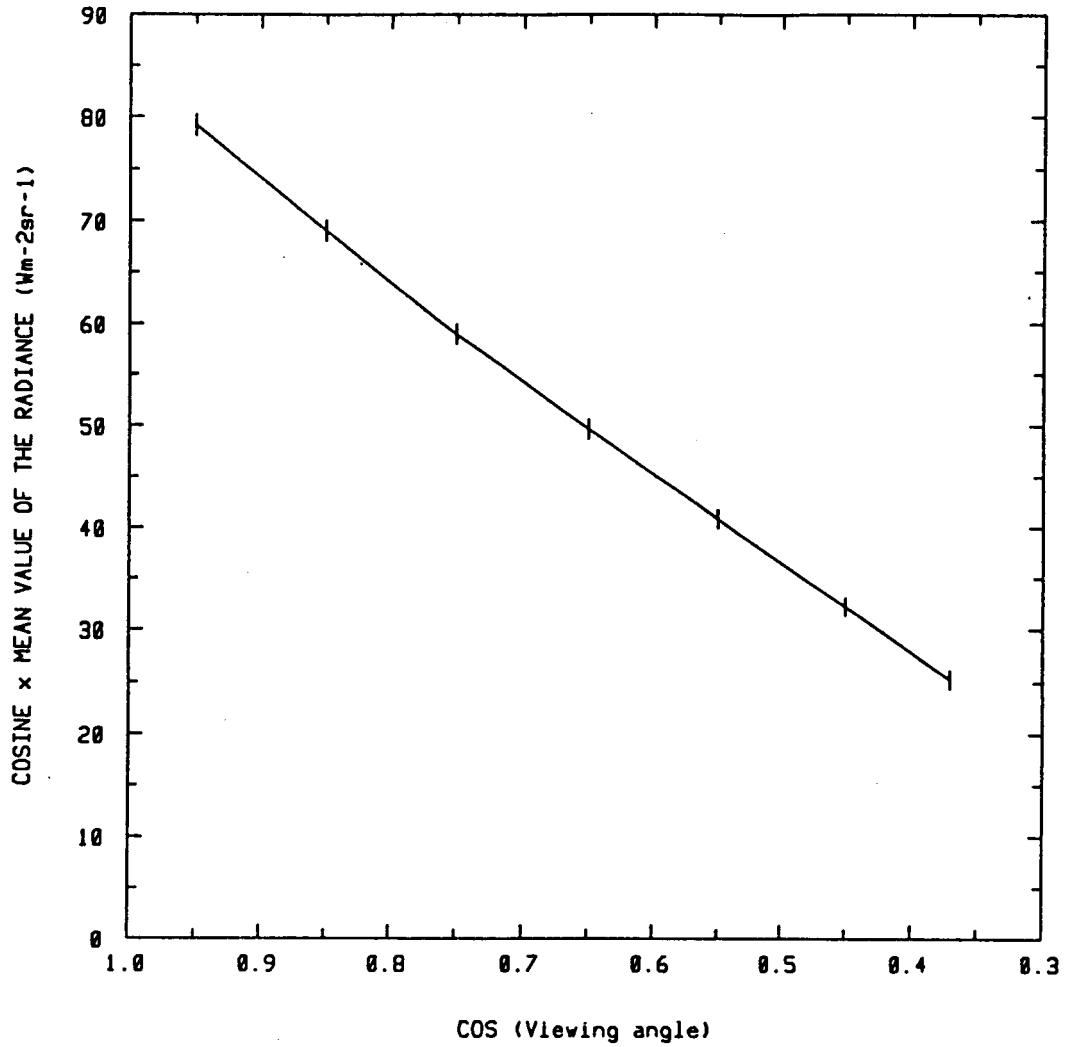
ERBS APRIL 1985

FIG. 3.1.1 Product of the LW radiance with the cosine of viewing angle versus the values of this cosine. Data are from ERBS April the 1st to the 10th, 1985 and for all θ_o, all ϕ and $0° \leq \lambda \leq 10°N$.

ERBS APRIL 1985
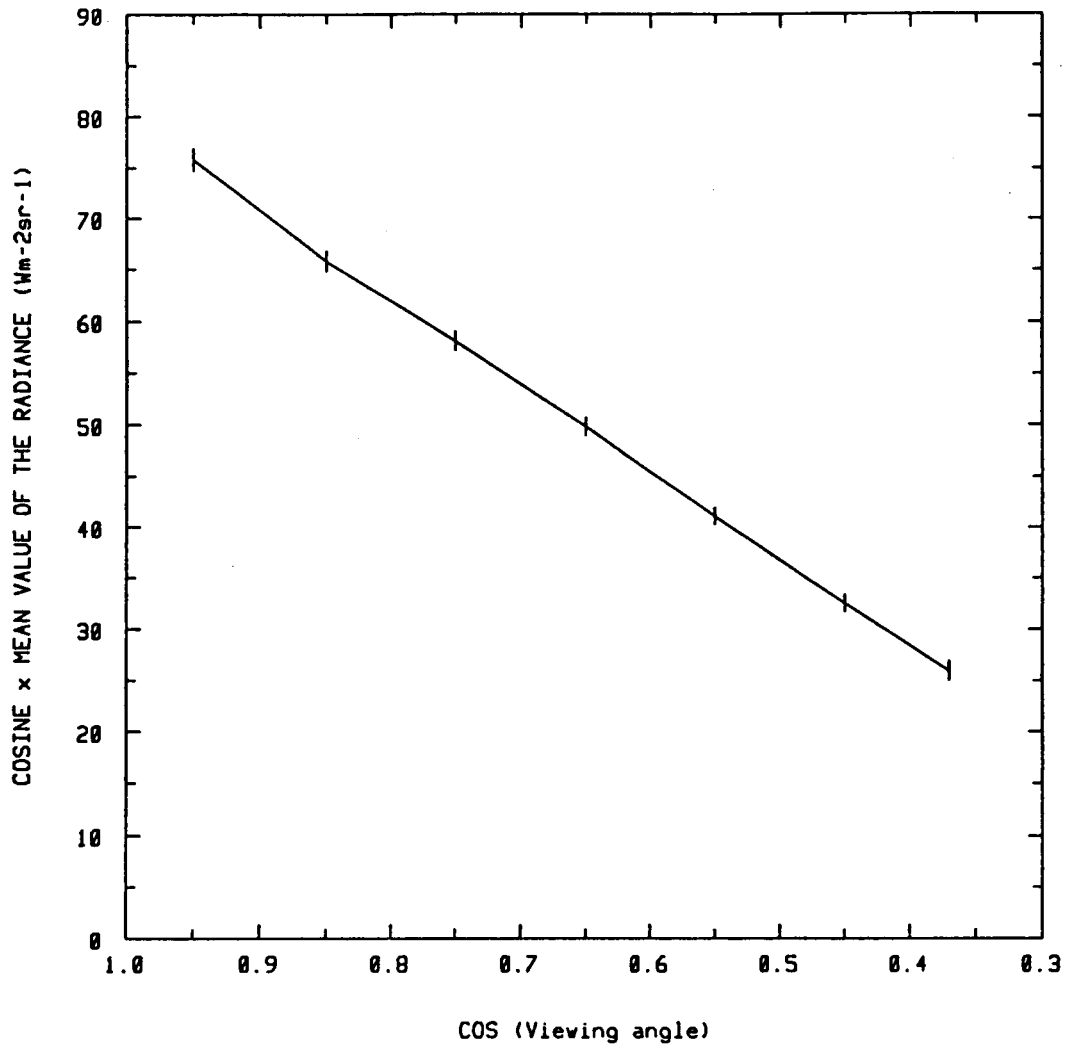
FIG. 3.1.2 Same as Fig. 3.1.1 with $30°N \leq \lambda \leq 40°N$.

ERBS APRIL 1985
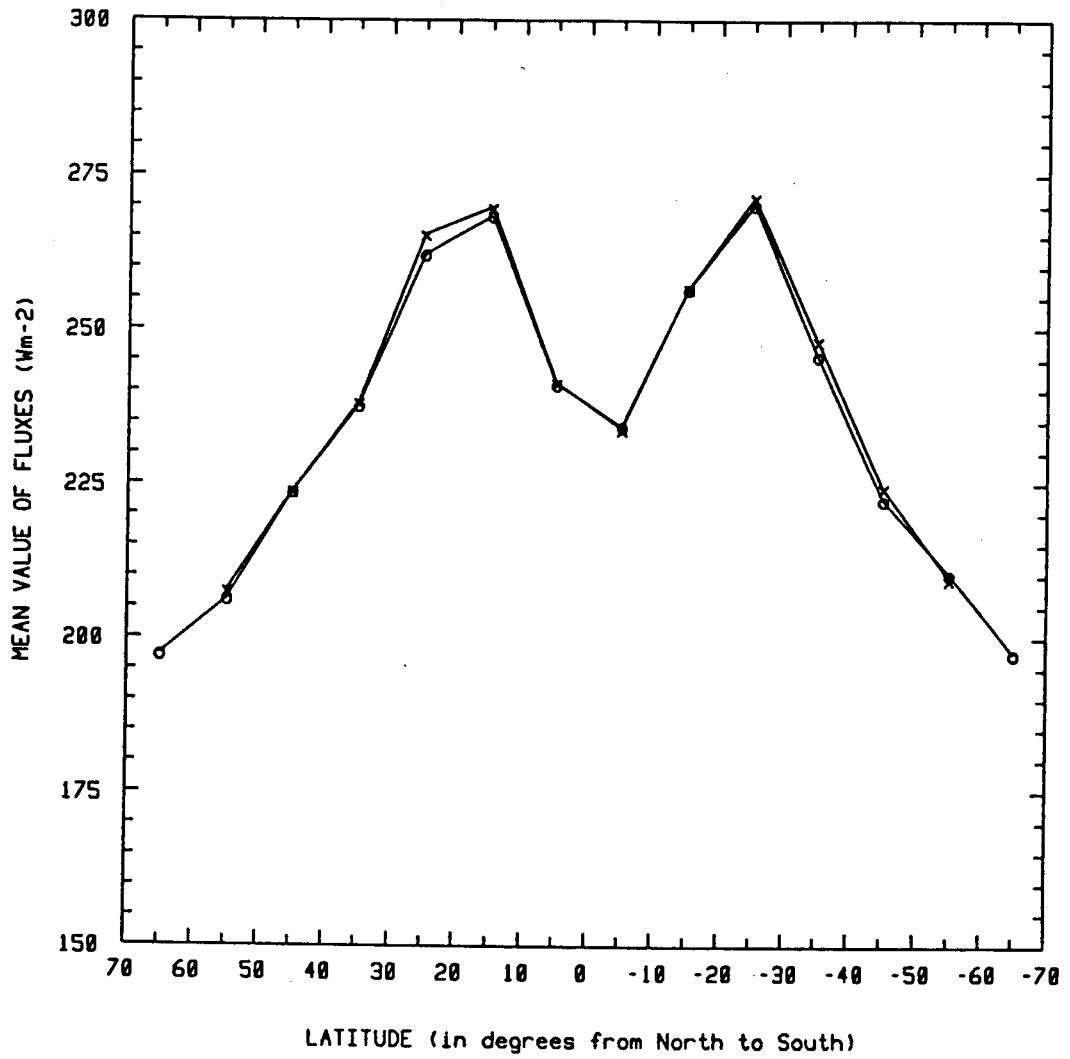
FIG. 3.1.3 Integrated and estimated LW fluxes versus latitude. The x sign is for integrated flux while the o sign is for estimated flux. Data are from ERBS April the 1st to the 10th, 1985 and for all θ_o and all ϕ.

ERBS APRIL 1985

FIG. 3.1.4 Absolute difference between the integrated and estimated
LW fluxes given by curves in Fig. 3.1.3.

The curves reach two maxima of about 270 Wm^{-2} near $20°$ North and South. This value drops at 235 Wm^{-2} near the equator because of the higher cloudiness.

An important conclusion is the fact that the integrated and the estimated flux curves are almost identical. Figure 3.1.4 shows the difference

$$\Delta F = \bar{F}_{int} - \bar{F}_{est} \qquad (3.2)$$

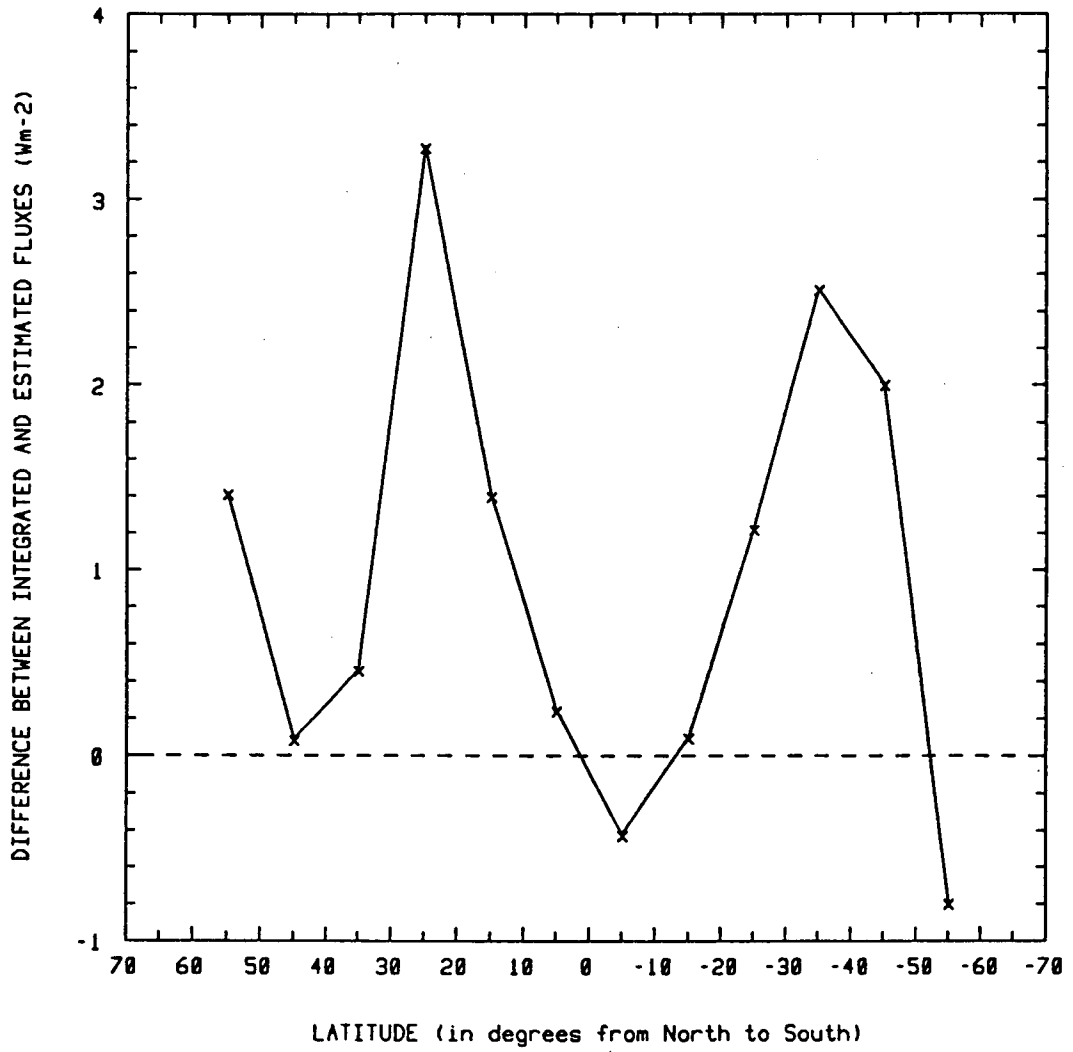for each latitude band. The absolute difference is never larger than 3.5 Wm^{-2} and is maximum near maximum fluxes. The relative difference

$$\Delta F_{rel} = \frac{\Delta F}{1/2 \ (\bar{F}_{int} + \bar{F}_{est})} \qquad (3.3)$$

is of the order of 1%. Since the radiances are direct satellite measurements and since they have shown a very uniform behaviour, much confidence is given to the integrated fluxes. The fact that the estimated fluxes are within 1% of the value of the integrated fluxes suggests that the LW directional models are very good and that the LW fluxes can be obtain directly by taking their ERBE estimated values.

3.2   Shortwave results

3.2.1   SW radiances

The reflected SW radiation depends on more parameters than the LW emission and is hence expected to show, in agreement with the correlation results, much more natural variability than the LW radiation. It also depends much more on Sun position, i.e. θ_o, than on the latitude λ. For that reason, the SW data are divided into viewing

52

angle and solar zenith angle bins in the following way : 10 equal μ_0 bins from $\mu_0 = 1$ to $\mu_0 = 0$ and 7 equal μ bins from $\mu = 1$ to $\mu = 0.3$ near where the cutoff angle occurs. Calculation for each θ and θ_0 bins were made for the values of $\bar{\mu}$, the mean of $\cos\theta$; $\bar{I}$, the mean of the SW radiance ; $\overline{I\mu}$, the mean of the product of I and μ and for $\bar{F}_{est}$, the mean of the estimated SW fluxes related with the radiance measurements. Data were taken from 10 days of ERBS November 1984 and April 1985 data sets and were collected on alternate days to avoid redundancy and to study a large enough range of solar zenith angles.

One of the first questions to arise was whether or not the product of the mean of I and μ is equal to the mean of the product $I\mu$. The answer to that question is interesting because it gives an idea of the homogeneity in the viewing angle samples and because it also shows a possible scatter of the product of I with μ within a θ bin (remember that the covariance is given by $\sigma_{xy} = \overline{xy} - \bar{x}\cdot\bar{y}$). Figure 3.2.1 gives an example of $\overline{I\mu}$ and $\bar{I}\cdot\bar{\mu}$ versus μ. The two curves perfectly overlap. This is also true for each of the other data sets studied.

The next results are given in a series of graphs representing three physical quantities inferred from ERBE SW data versus viewing angle. These quantities are the product $\overline{I\mu}$ which will be used to calculate the integrated SW flux, the value of the radiance $\bar{I}$ and the value of the normalized estimated flux (i.e. the estimated mean radiance) defined as

$$F'_{est} = \frac{F_{est}}{\pi} \qquad (3.4)$$

53

ERBS APRIL 1985
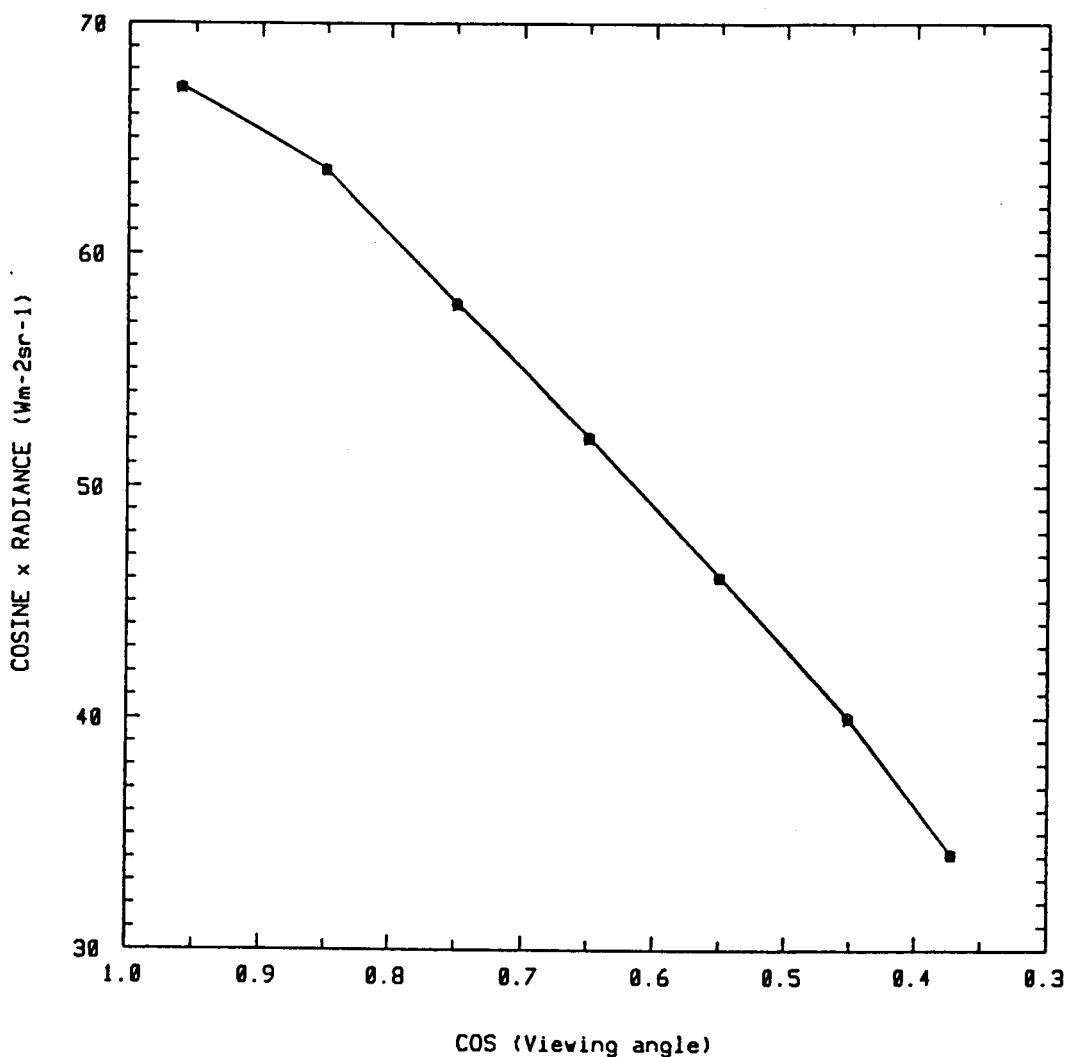

FIG. 3.2.1 Comparison of the values of the cosine of viewing angle times the SW radiance versus the cosine. The x sign is for the mean $\overline{I}\mu$ and the o sign is for the product $\overline{I}\cdot\overline{\mu}$. Curves are perfectly superposed. Data are from ERBS April the 3rd to the 21st, 1985 taking alternate days and for $0.7 \leq \mu_o \leq 0.8$.

which gives the uniform value of the radiance of an isotropic radiation field having a flux F_{est}. Figures 3.2.2 to 3.2.6 are related to April data. They show results for five different ranges of solar zenith angle θ_o, from overhead position ($0.9 \leq \mu_o \leq 1.0$) to a near horizon position ($0.1 \leq \mu_o \leq 0.2$). In each graphs, the upper solid and dot-dashed curves are for $\bar{I}$ and $\bar{F}'_{est}$ respectively while the lower curve is for $\overline{I\mu}$. Error bars are shown which are given by one standard deviation of the mean on each sides of the different curves.

The curves for $\overline{I\mu}$ present very little statistical noise and are quite smooth for every Sun positions. They are extrapolated with a parabola passing through the origin and the last two data points in order to provide a complete set of values of $\overline{I\mu}$ for each $\Delta\mu = 0.1$ viewing angle bins so that an integrated SW flux can be calculated. For overhead Sun (Fig. 3.2.2) the value of $\overline{I\mu}$ near nadir show a strong backscatter of the reflected SW radiation. For the other four Sun positions, the curve $\overline{I\mu}$ is smooth and has downward curvature.

The values of $\bar{I}$ and $\bar{F}'_{est}$ can also be compared. Since

$$F_{est} = \frac{\pi I}{\mathcal{R}} \tag{3.5}$$

where $\mathcal{R}$ is the bidirectional function,

$$\mathcal{R} = \frac{I}{F'_{est}} \quad , \tag{3.6}$$

and the ratio of I to F'_{est} gives the value of the bidirectional function $\mathcal{R}$. For overhead Sun (Fig. 3.2.2) it is not far from 1 because

ERBS APRIL 1985
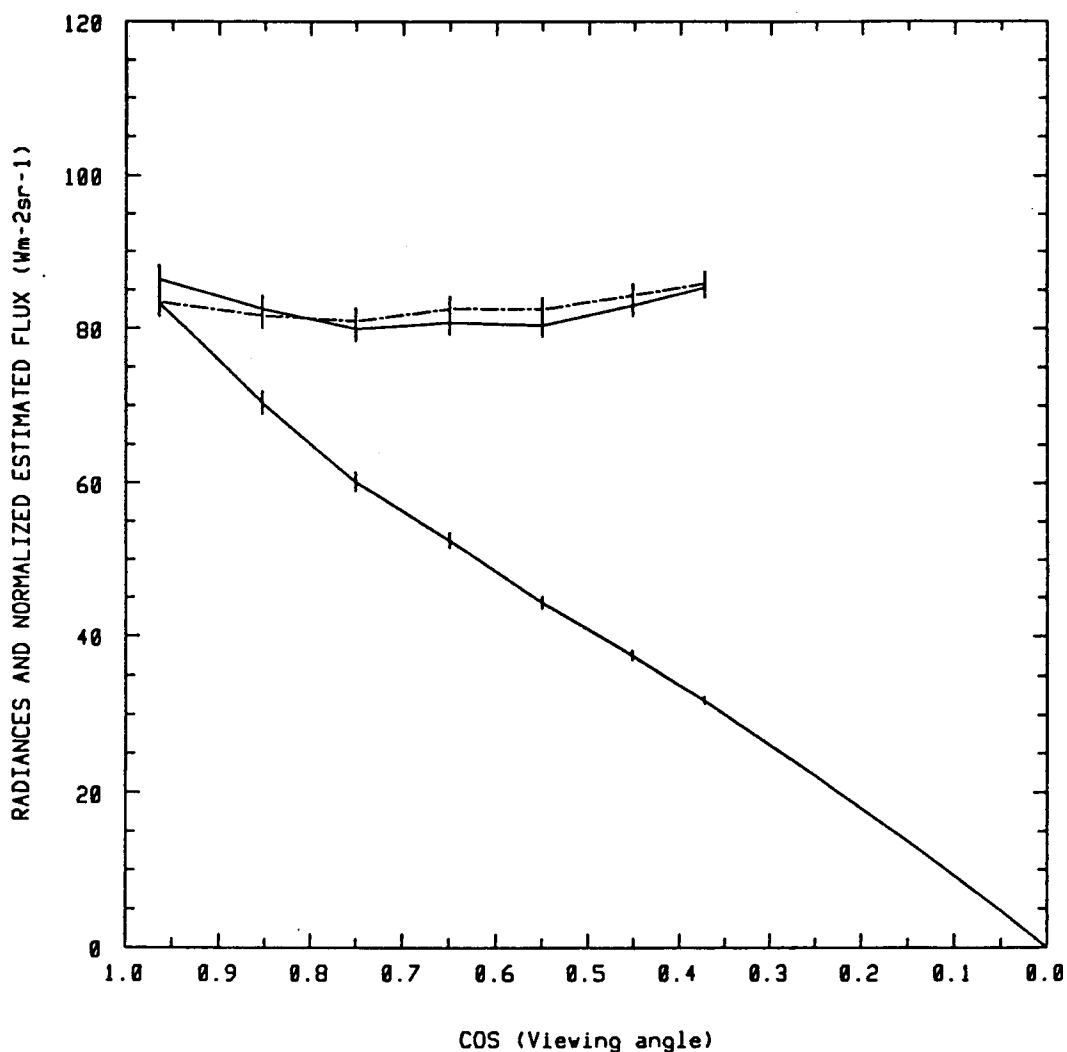
FIG. 3.2.2 Values of normalized estimated SW flux, SW radiance, and product of cosine of viewing angle with SW radiance versus the cosine. Dot-dashed curve is for F'_{est}, the upper solid curve is for I_{sw} and the lower solid curve is for $I_{sw}\mu$. Data are from ERBS April the 3rd to the 21st, 1985 taking alternate days and for $0.9 \leq \mu_o \leq 1.0$.
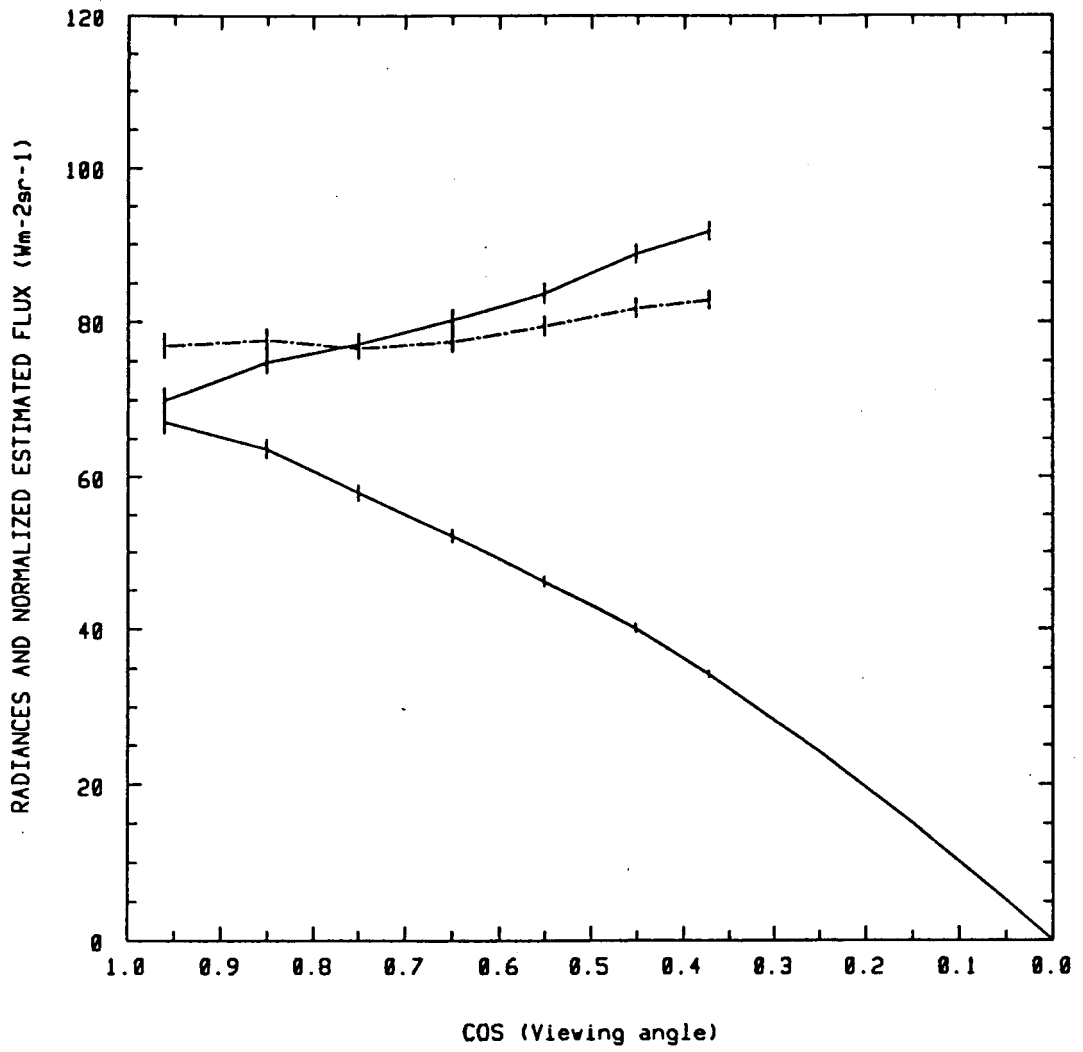
ERBS APRIL 1985

FIG. 3.2.3   Same as Fig. 3.2.2 with $0.7 \leq \mu_o \leq 0.8$.
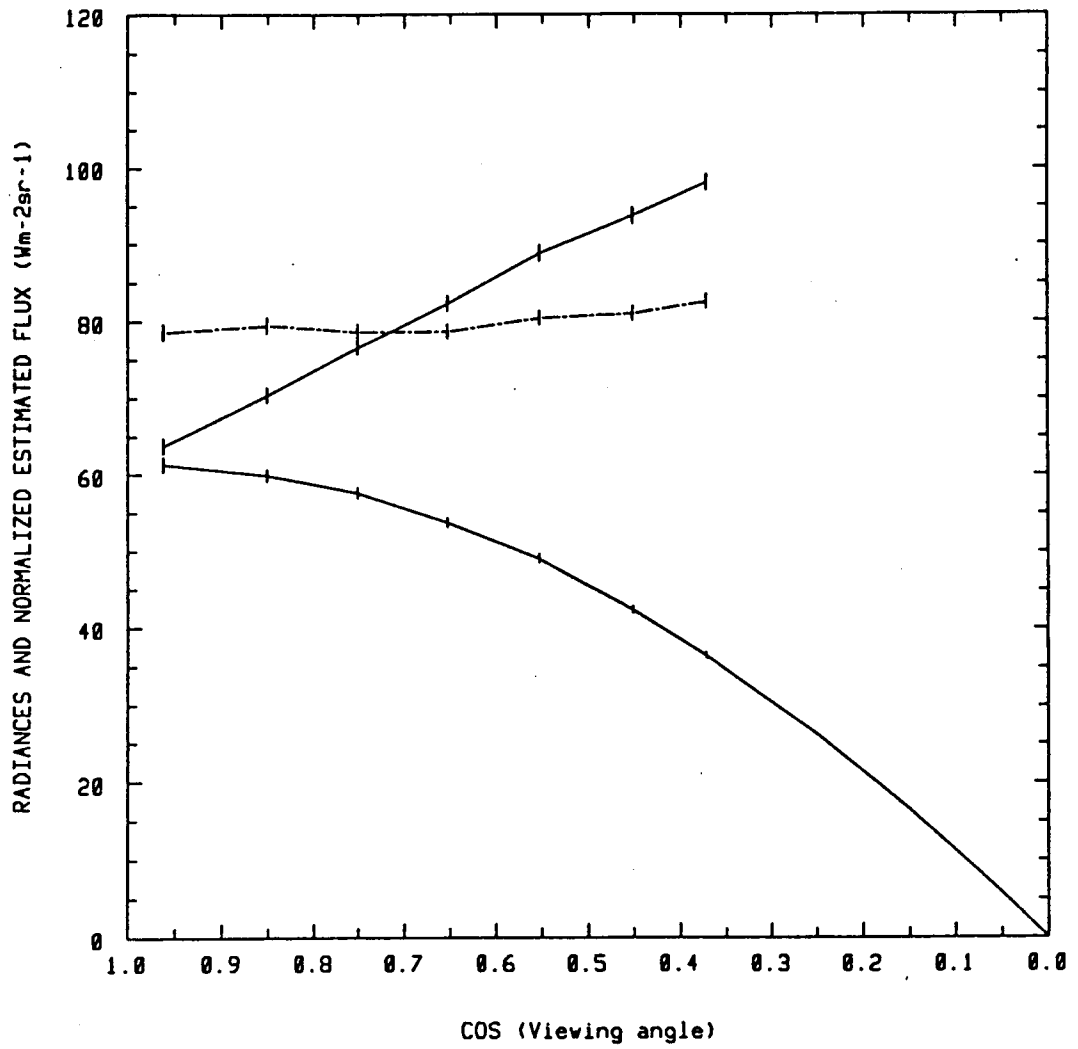
ERBS APRIL 1985

FIG. 3.2.4 Same as Fig. 3.2.2 with $0.5 \leq \mu_o \leq 0.6$.

58
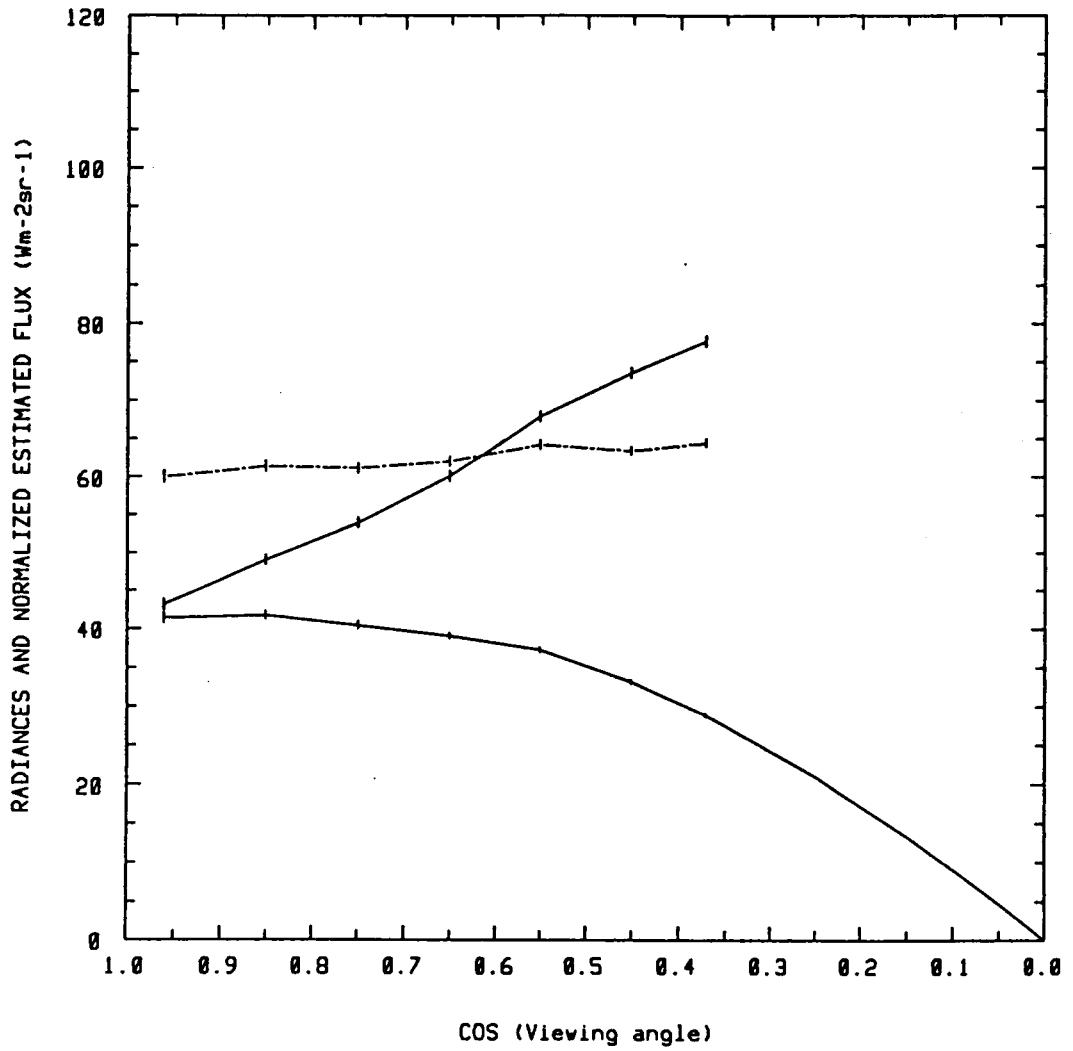
ERBS APRIL 1985

FIG. 3.2.5 Same as Fig. 3.2.2 with $0.3 \leq \mu_o \leq 0.4$.

ERBS APRIL 1985
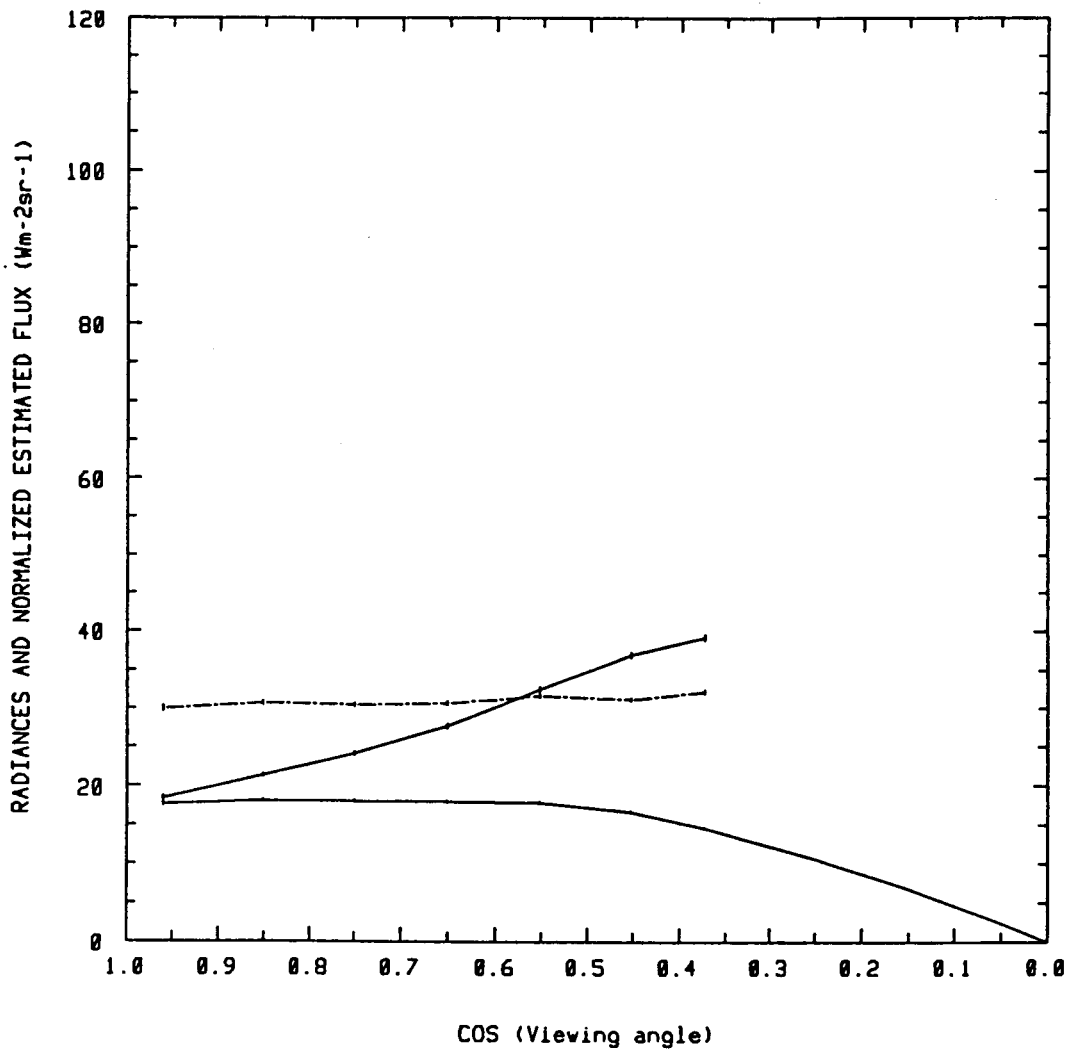
FIG. 3.2.6 Same as Fig. 3.2.2 with $0.1 \leq \mu_o \leq 0.2$.

of the symmetry of the illumination, but for the inclined Sun positions it can be observed that the radiation field is anisotropic with higher values of the radiance occuring at large viewing angles. This is due to the cloudy or partially cloudy scenes since cloud sides tend to reflect more radiation than the cloud tops.

. It can also be noted that $\overline{F}'_{est}$ has a weak but persistant tendency to increase with θ. If the bidirectional function $\mathcal{R}$ was perfect, the $\overline{F}'_{est}$ curve would remain flat with viewing angle.

Similar results for November 1984 are presented in Figs. 3.2.7 to 3.2.11. As for April, the curves for $\overline{I\mu}$ are smooth. Again, for the overhead Sun position (Fig. 3.2.7), backscattered SW radiation is observed. The curves for $\overline{I}$ and $\overline{F}'_{est}$ show a similar behaviour to the previous April results. The value of $\mathcal{R}$ is also close to 1 for overhead Sun position while indicating an asymmetric SW radiation field with the larger radiances at large viewing angle for the other oblique Sun positions. The only exception concerns Fig. 3.2.8 ($36.9° \leq \theta_o \leq 45.6°$) where $\overline{I}$ reaches its maximum near $\theta = 50°$. The values of the estimated SW fluxes still show a slight tendency to increase with viewing angle.

3.2.2   SW integrated versus estimated fluxes

An interesting experiment is to compare the integrated fluxes calculated from the ERBE scanner SW radiance measurements with their corresponding estimated fluxes from the bidirectional models.

The integrated flux is obtained using

ERBS NOVEMBER 1984
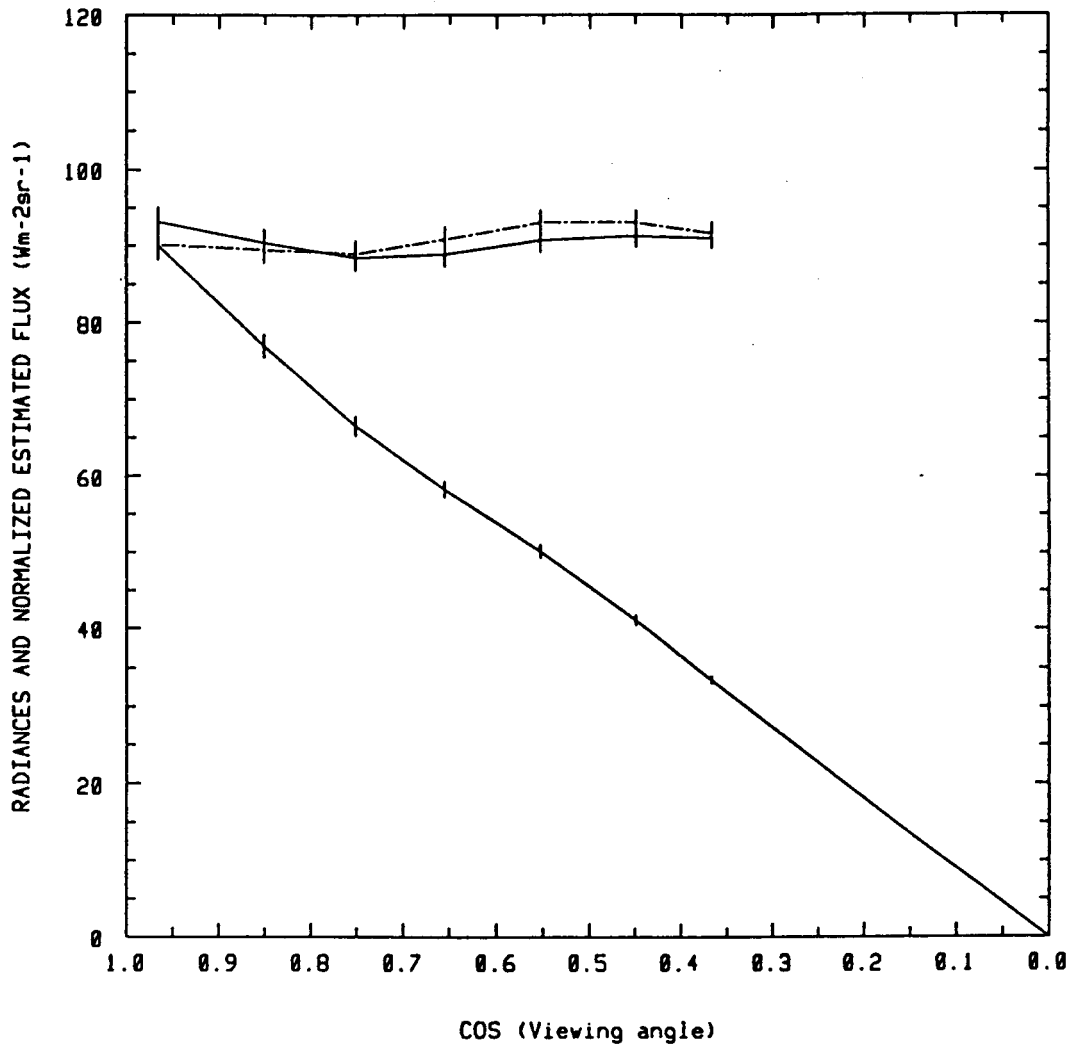
FIG. 3.2.7 Same as Fig. 3.2.2 with data from ERBS November the 5th to the 23rd, 1984 taking alternate days and for $0.9 \leq \mu_o \leq 1.0$.

ERBS NOVEMBER 1984
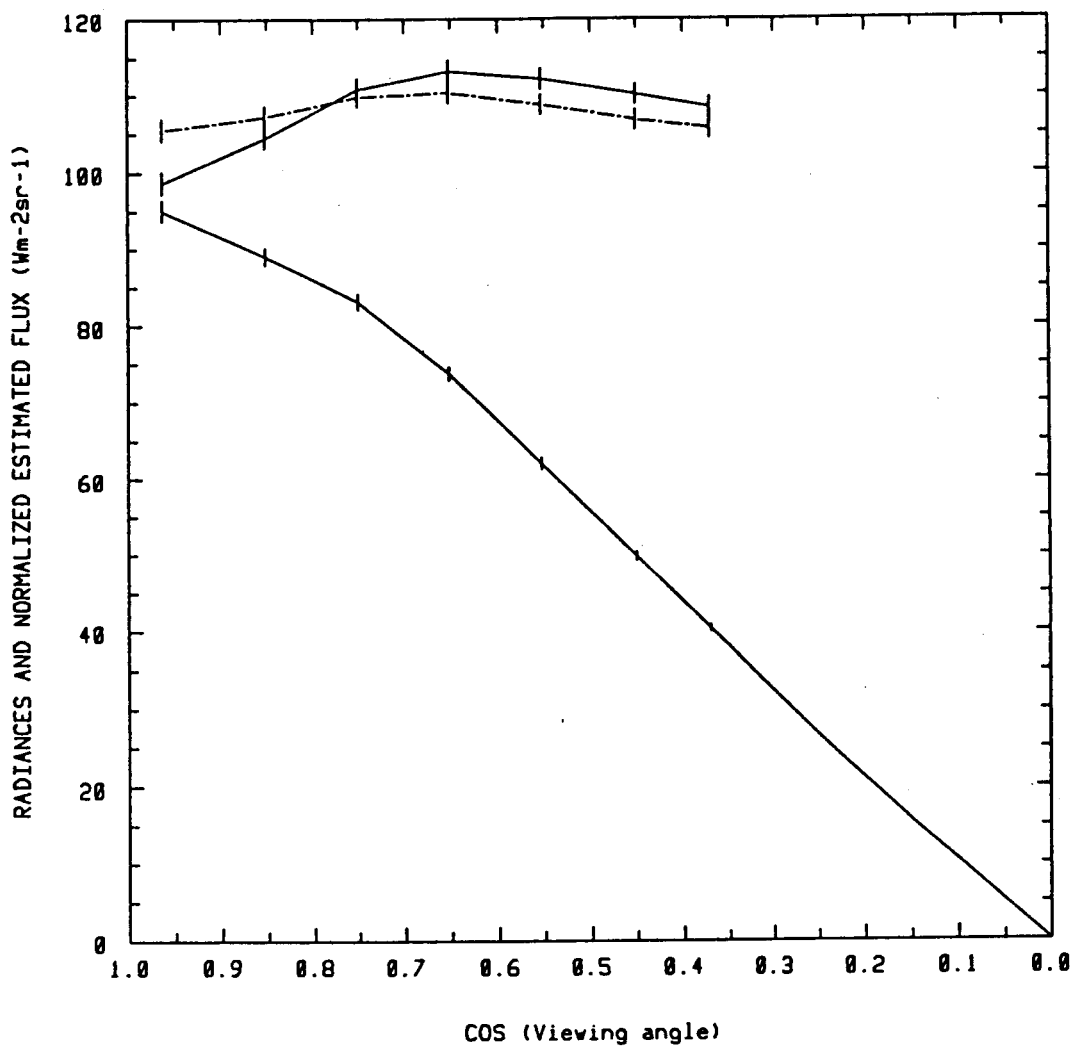
FIG. 3.2.8 Same as Fig. 3.2.7 with $0.7 \leq \mu_o \leq 0.8$.

ERBS NOVEMBER 1984
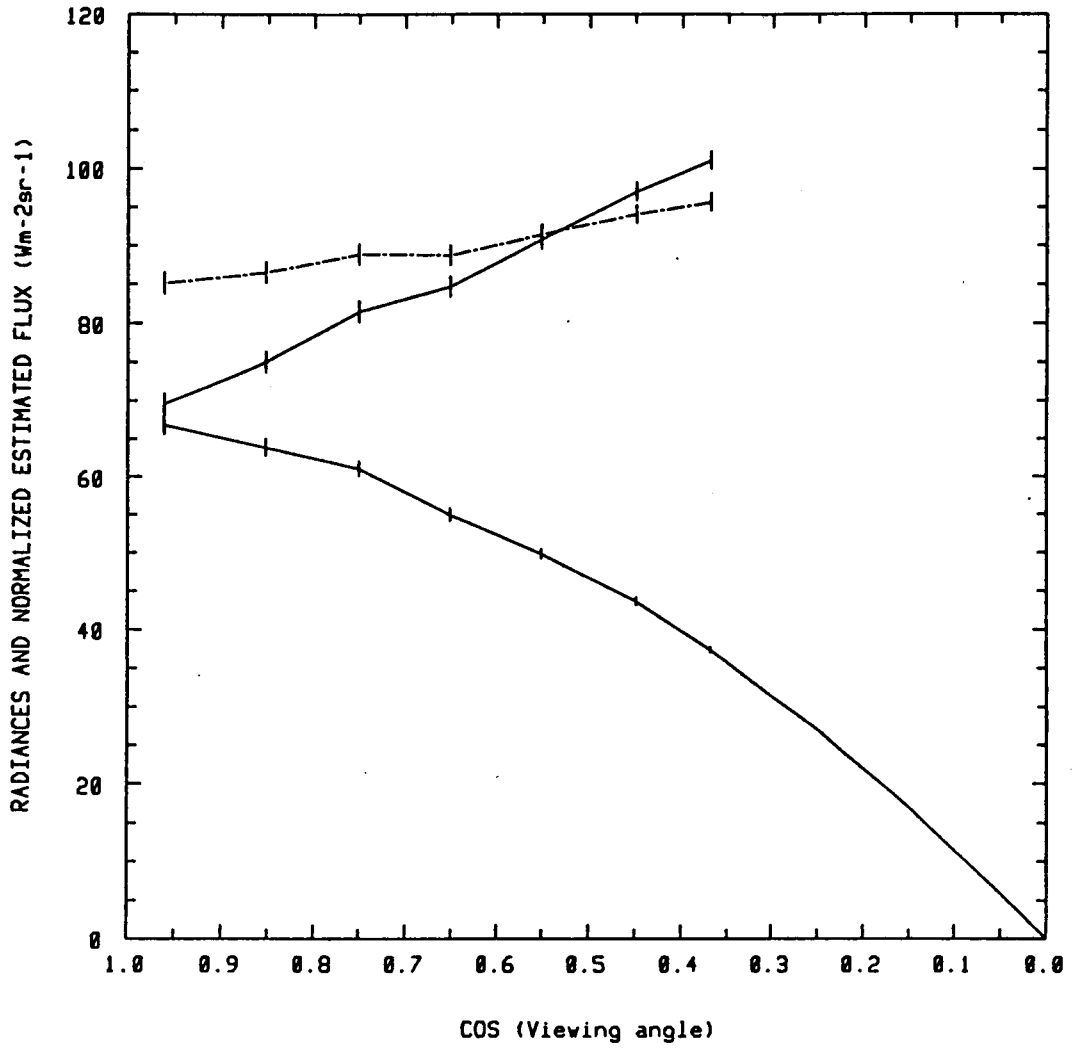
FIG. 3.2.9   Same as Fig. 3.2.7 with $0.5 \leq \mu_o \leq 0.6$.

ERBS NOVEMBER 1984
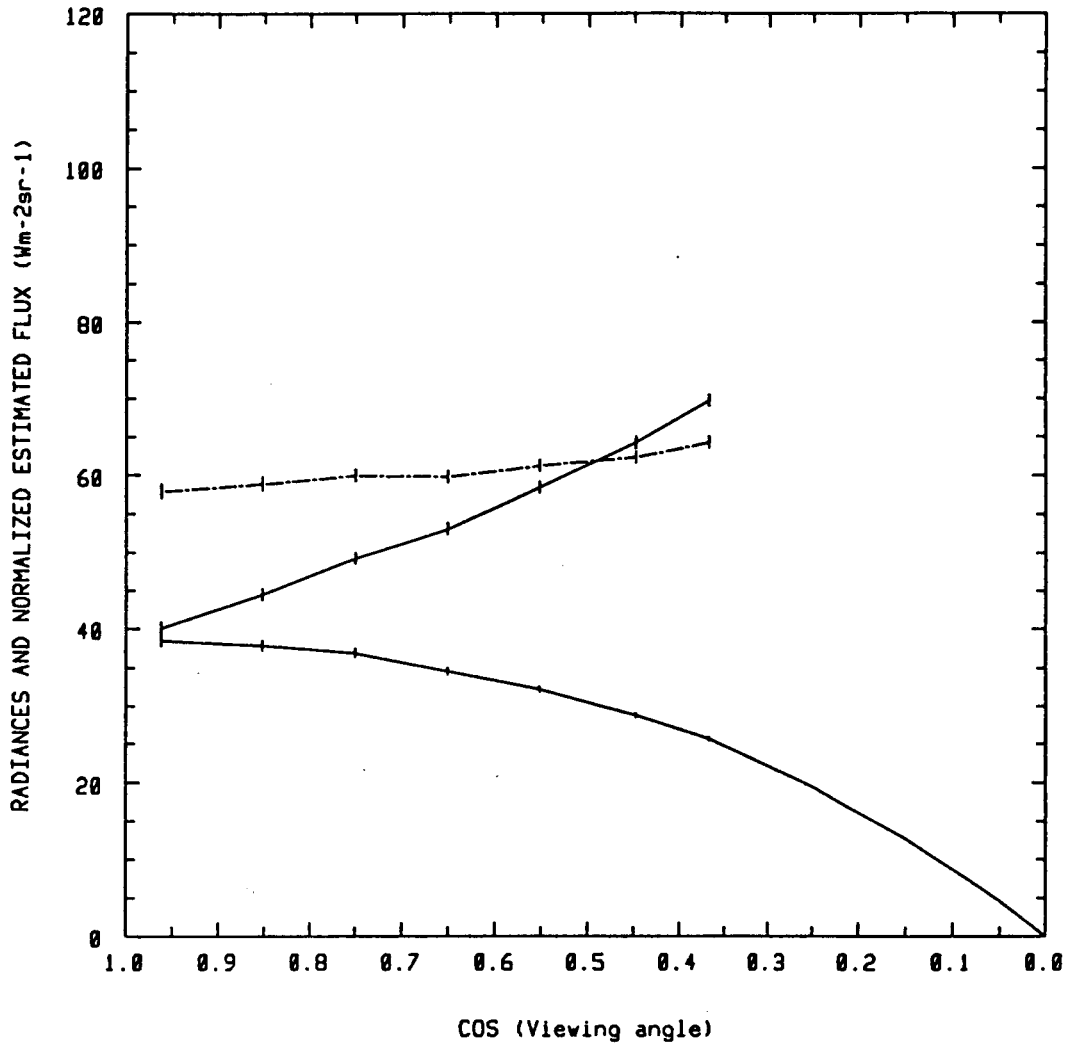
FIG. 3.2.10 Same as Fig. 3.2.7 with $0.3 \leq \mu_o \leq 0.4$.

ERBS NOVEMBER 1984
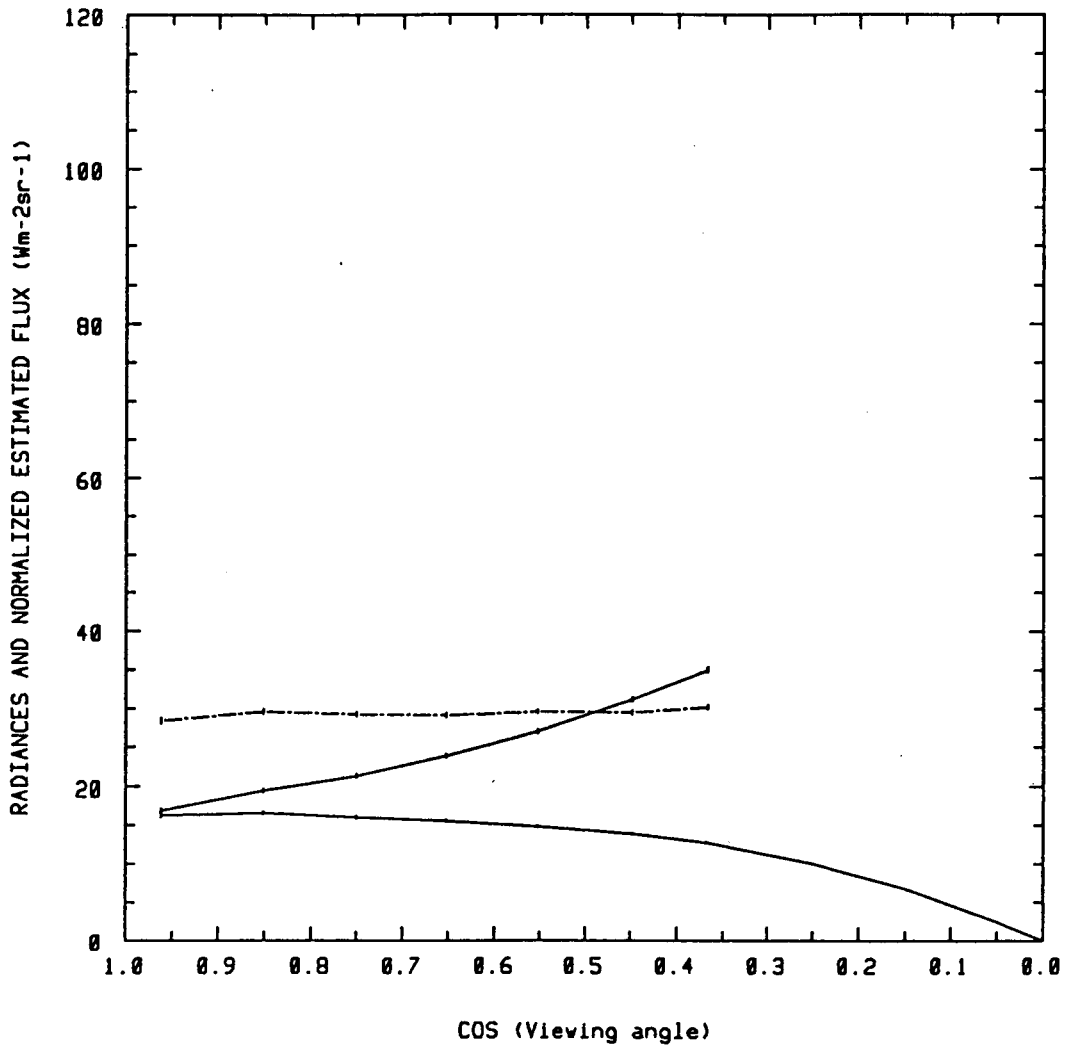
FIG. 3.2.11 Same as Fig. 3.2.7 with $0.1 \leq \mu_o \leq 0.2$.

$$\overline{F}_{int} = 2\pi \sum_{i=1}^{10} \overline{I\mu_i} \cdot \Delta\mu_i \qquad (3.7)$$

where $\Delta\mu_i = 0.1$ and the last three values of $\overline{I\mu_i}$ for $\mu \leq 0.3$ are extrapolated using a parabola as explained earlier. The estimated SW fluxes F_{est} are directly given in the ERBE data packages. As in the last section, data are from ERBS November 1984 and April 1985 and are taken on alternate days.

First, a global comparison is made and mean values are calculated regardless of viewing angle and solar zenith angle. For 10 days in April, $\overline{F}_{int}$ is 200 ± 4 Wm^{-2} and $\overline{F}_{est}$ is 200 ± 3 Wm^{-2} where the error is given by one standard deviation of the mean. For 10 days in November, $\overline{F}_{int}$ and $\overline{F}_{est}$ are respectively 219 ± 4 Wm^{-2} and 228 ± 3 Wm^{-2}. These mean values do not have a physical significance since they do not take account of Sun position and equally weight overhead and oblique Sun cases. What is more relevant is the difference

$$\Delta F = \overline{F}_{int} - \overline{F}_{est} \ . \qquad (3.8)$$

Because $\overline{I\mu}$ has low statistical noise and use of integrated radiances avoids the uncertainty of angular models, more confidence may be given to the integrated fluxes. Consequently, ΔF gives an indication of the reliability of the mean values of estimated fluxes since they are compared with the trusted integrated fluxes. For April, ΔF is 0 ± 5 Wm^{-2}

and for November ΔF is -9 ± 5 Wm^{-2}. At this point, it is important to note the significance of the standard error related to ΔF. With the sampling strategy used, the data for the radiance as well as for the estimated flux are considered as being independent but since I is collected at the same time as its corresponding value of F_{est} there is a

dependence of F_{est} on I. This means that when, for example, a single value of I is greater than the mean $\bar{I}$, there is a high probability that its corresponding value of F_{est} will be greater than the mean $\bar{F}_{est}$. It is then likely that the real error for ΔF is not simply the sum of the errors for $\bar{F}_{int}$ and $\bar{F}_{est}$. For the study of ΔF, the standard error $\sigma_{\Delta F}$ is calculated assuming independent statistical data and is considered to be an upper limit to the real error for ΔF. Considering the previous experiment only, it would seem that ΔF is not far from zero and that, especially for April, confidence can also be given to the estimated SW fluxes. A more sophisticated comparison of $\bar{F}_{int}$ and $\bar{F}_{est}$ will show that this is not correct.

The same November and April data are now separated into 10 equal μ_o bins. Figure 3.2.12 displays the values of ΔF against μ_o for April. Error bars are shown having the same definition as before. The curve shows that ΔF has a clear tendency to be positive for $\mu_o \geq 0.5$ and negative for $\mu_o \leq 0.5$. In other words, the estimated fluxes tend to underestimate the integrated fluxes for smaller solar zenith angles and to overestimate them for the larger θ_o values. The same curve for the November data is presented in Fig. 3.2.13 and has a similar shape except that ΔF changes sign near $\mu_o = 0.7$.

A more detailed analysis can be done. In addition to the binning in μ_o, data are now divided into 7 equal μ bins for $0.3 \leq \mu \leq 1.0$ with $\Delta\mu = 0.1$. Figures 3.2.14 to 3.2.17 give the value of ΔF against μ for four different Sun positions in April. The first figure (Fig. 3.2.14) is for overhead Sun $(0.9 \leq \mu_o \leq 1.0)$. It indicates that the integrated flux is larger than the estimated flux for small viewing angles and that the

68
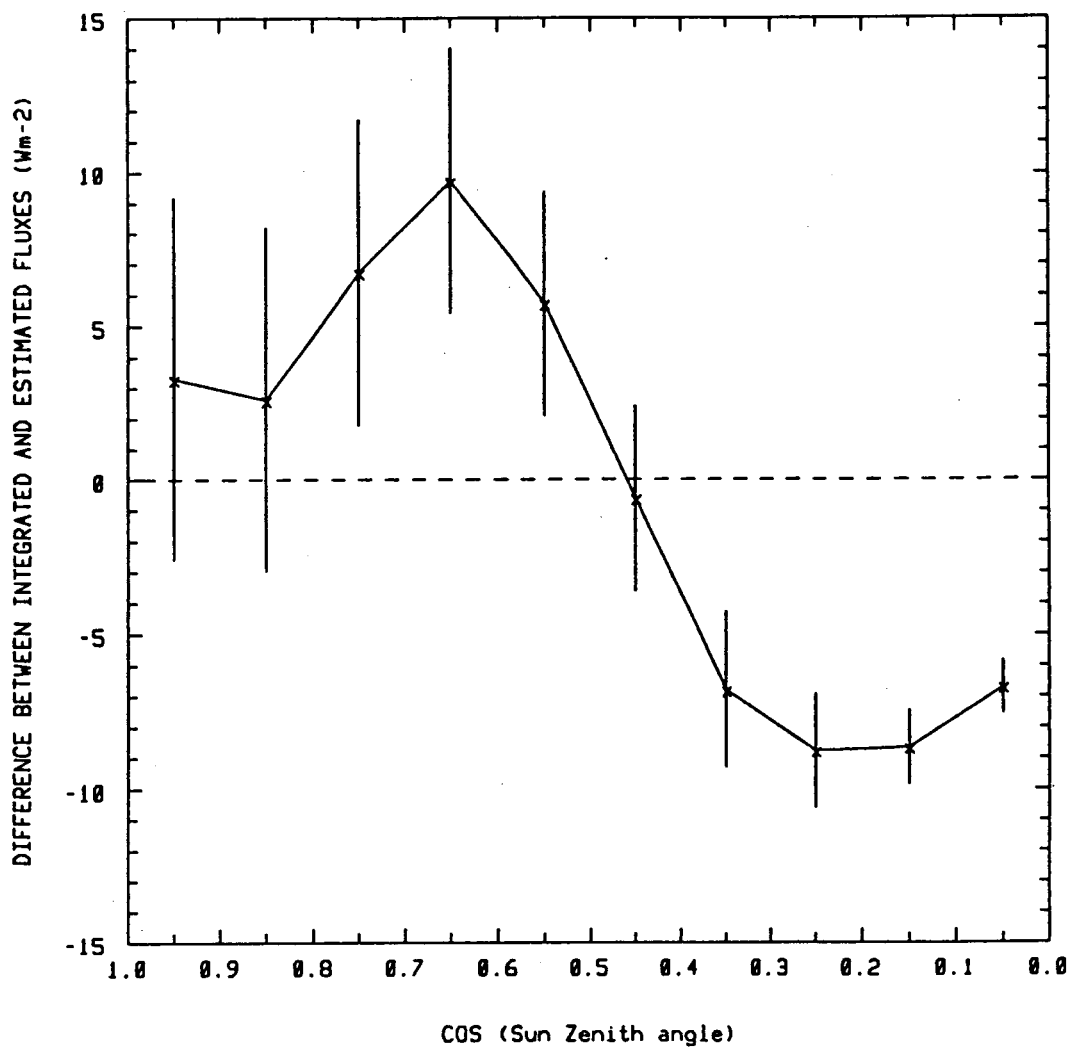
ERBS APRIL 1985

FIG. 3.2.12 Difference between integrated and estimated SW fluxes versus cosine of solar zenith angle. Data are from ERBS April the 3rd to the 21st, 1985 taking alternate days and for all θ.
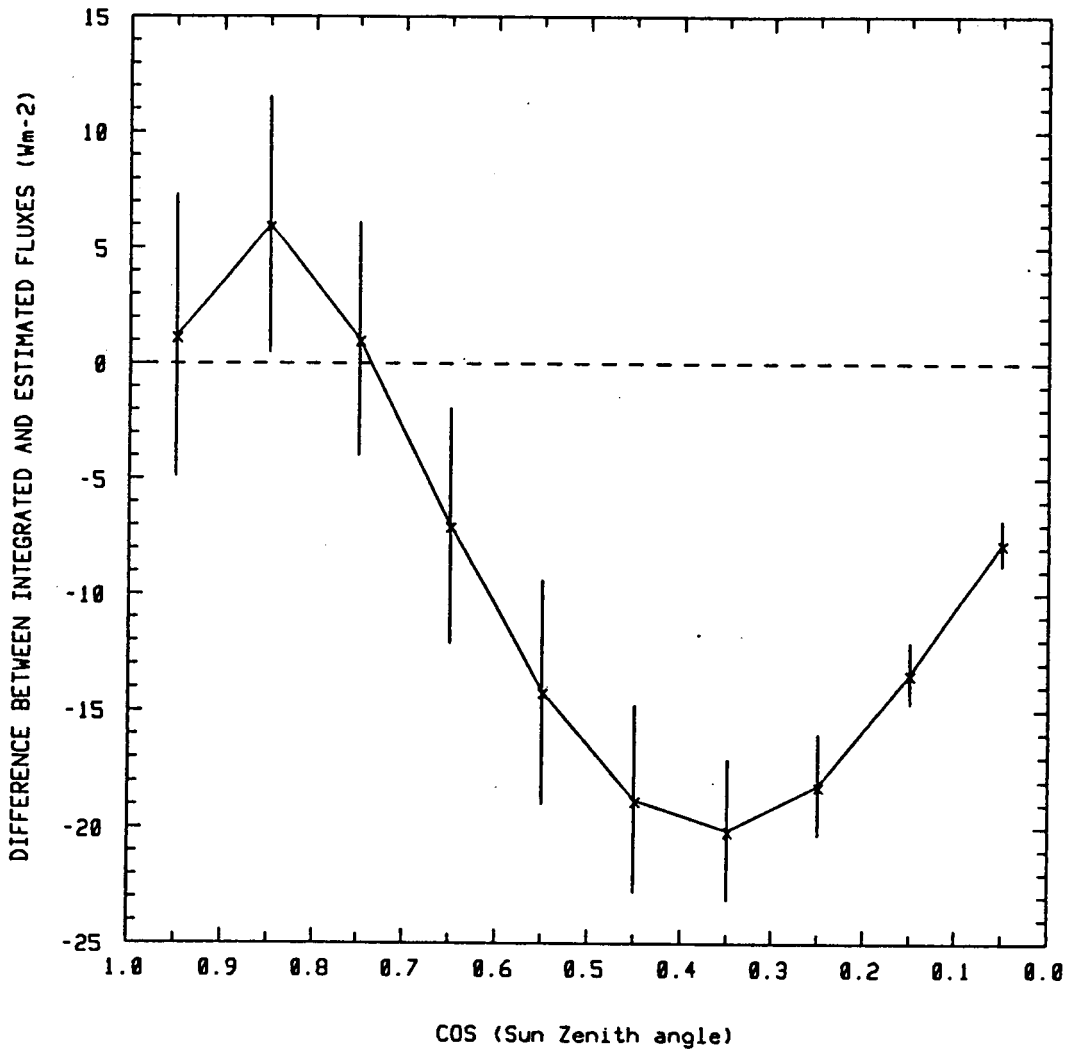
ERBS NOVEMBER 1984

FIG. 3.2.13 Same as Fig. 3.2.12 with data from ERBS November the 5th to the 23rd, 1984 taking alternate days.
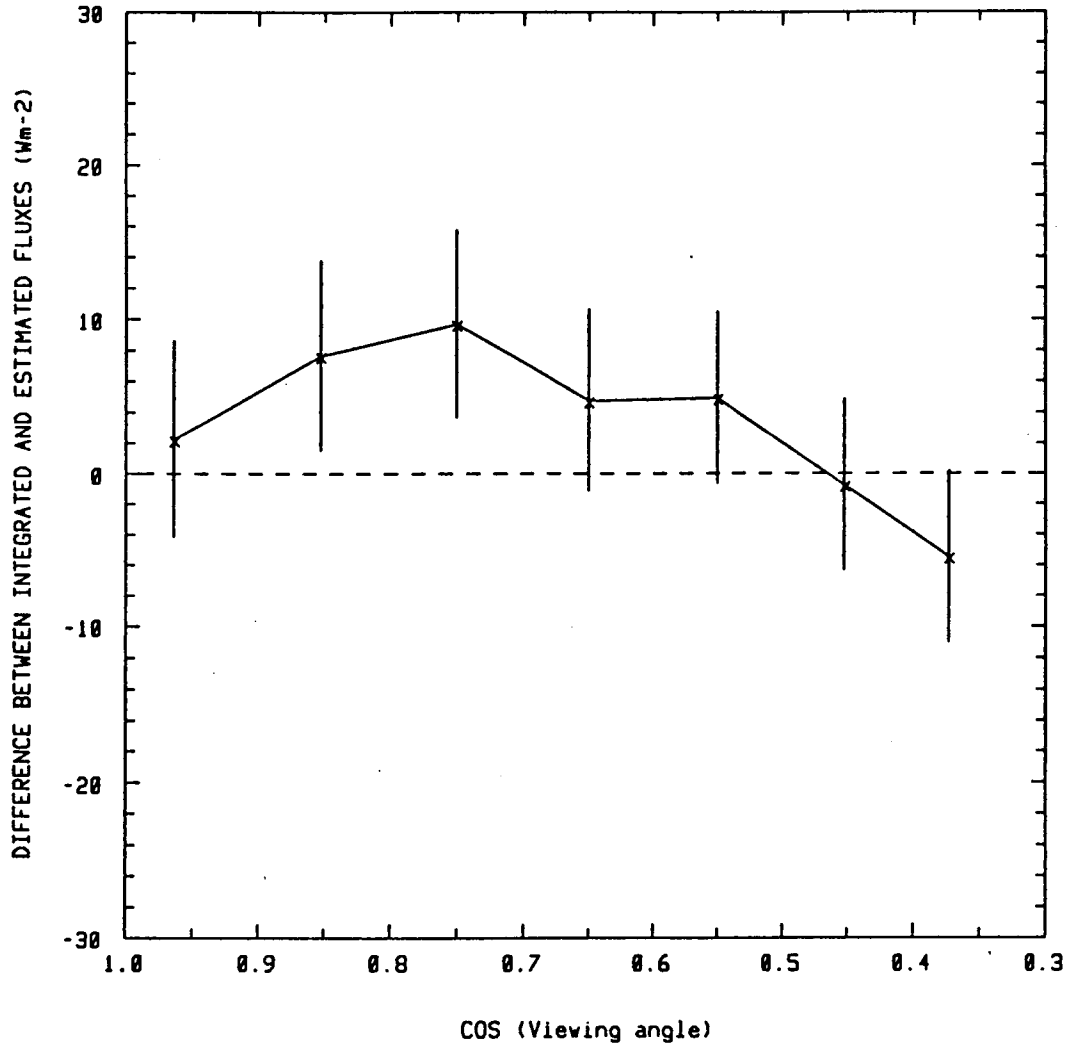
ERBS APRIL 1985

FIG. 3.2.14 Difference between integrated and estimated SW fluxes versus viewing angle for $0.9 \leq \mu_o \leq 1.0$. Data are from ERBS April as in Fig. 3.2.12.

ERBS APRIL 1985
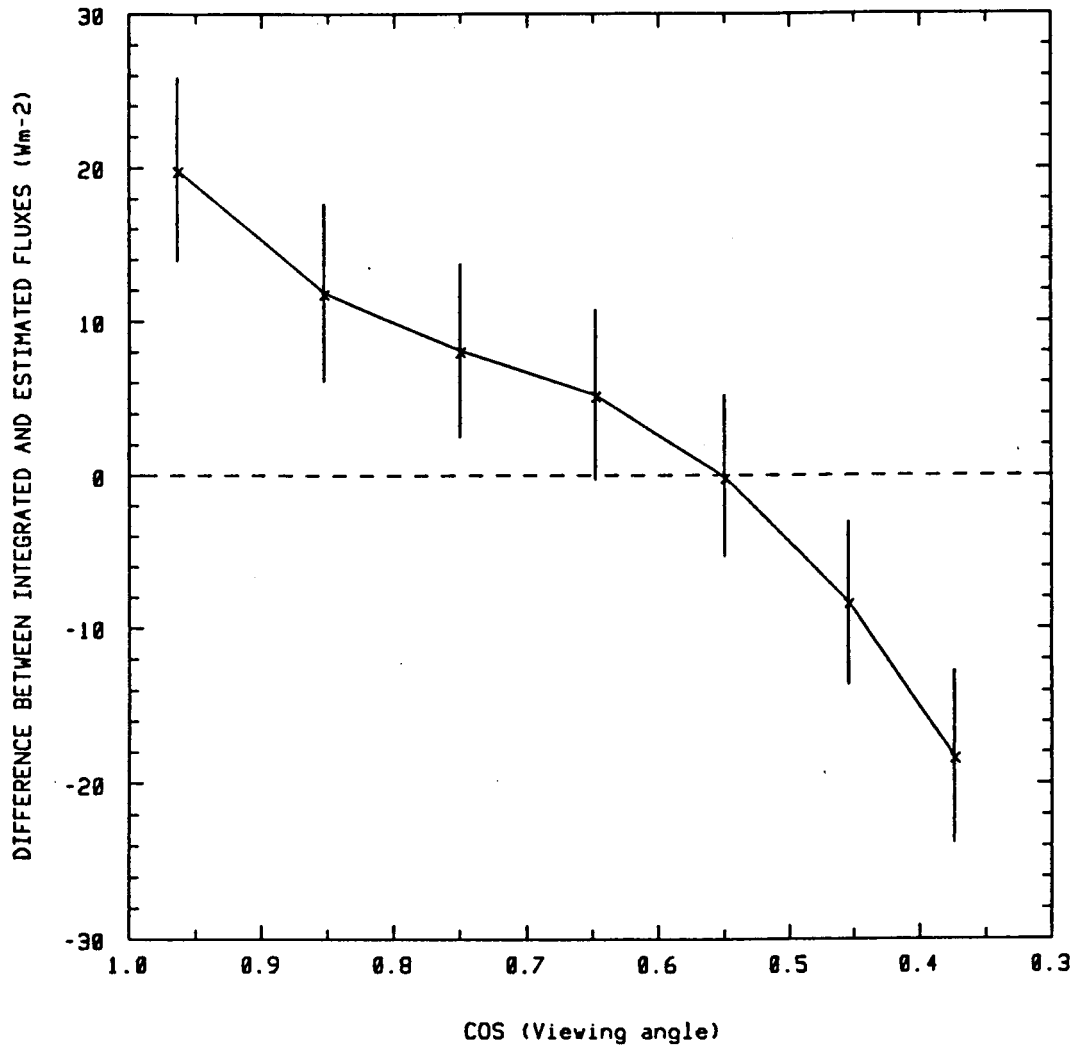
FIG. 3.2.15 Same as Fig. 3.2.14 with $0.8 \leq \mu_o \leq 0.9$.
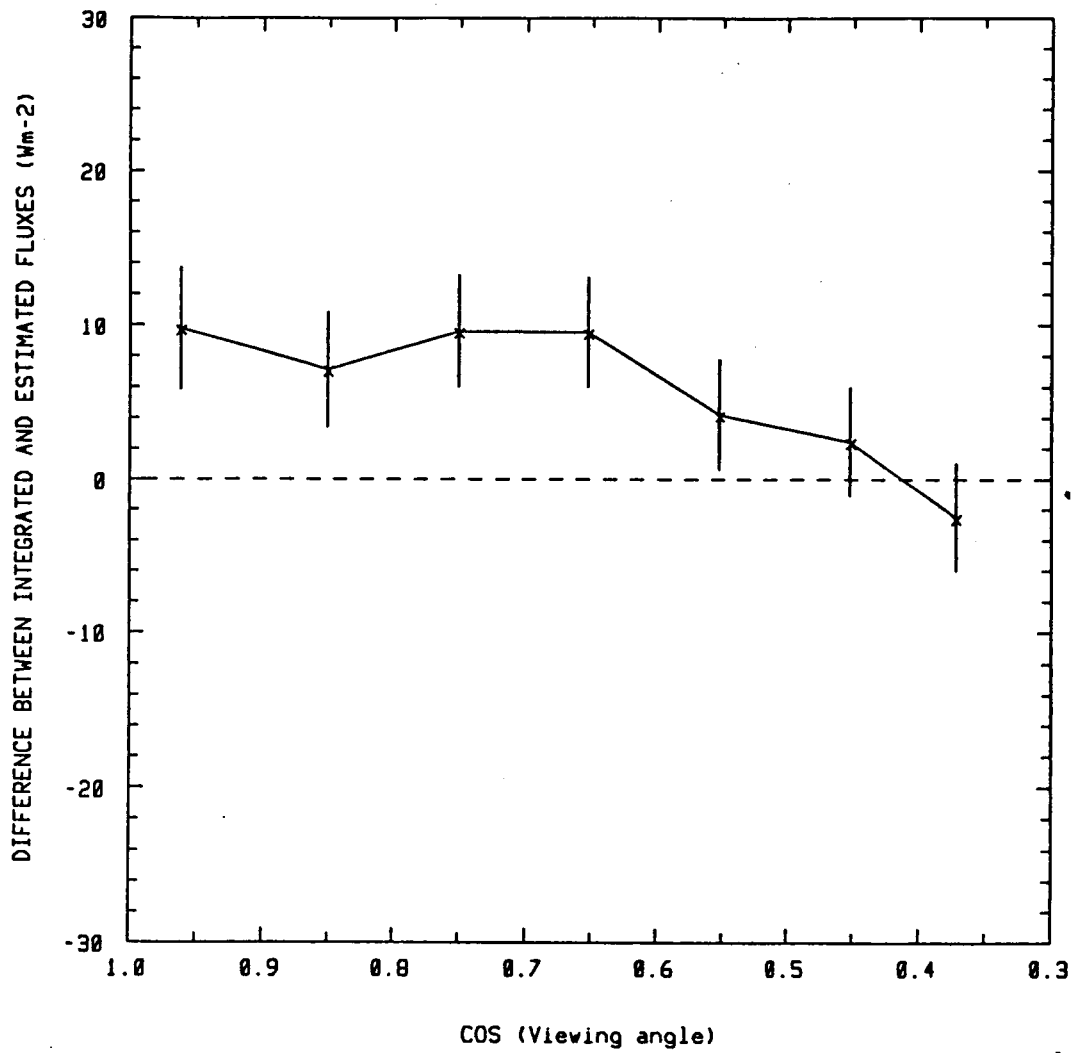
ERBS APRIL 1985

FIG. 3.2.16 Same as Fig. 3.2.14 with $0.5 \leq \mu_o \leq 0.6$.
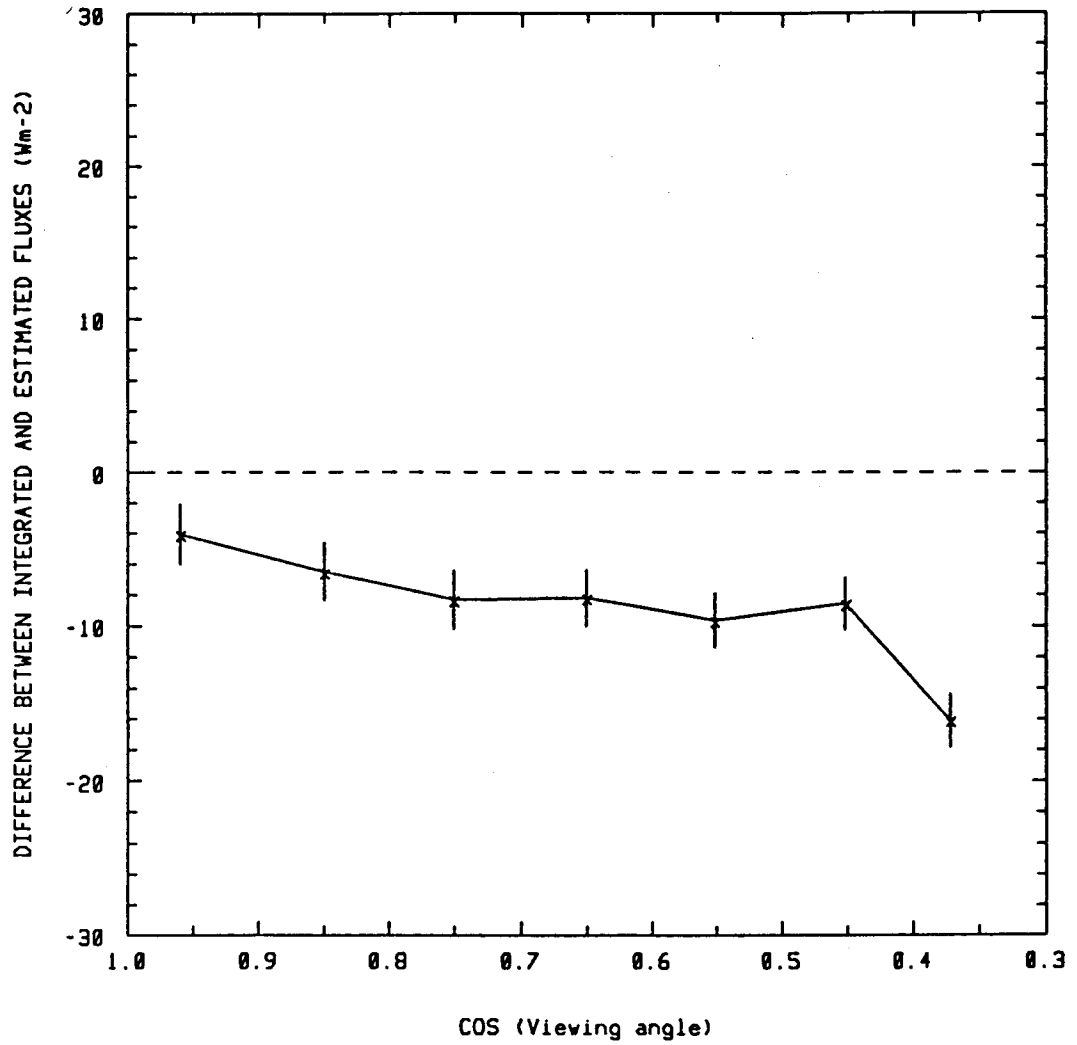
FIG. 3.2.17   Same as Fig. 3.2.14 with $0.2 \leq \mu_o \leq 0.3$.

best agreement between the two is for $\mu = 0.5$. The next figure (Fig. 3.2.15) is for $0.8 \leq \mu_o \leq 0.9$ and shows a similar trend except that ΔF is larger for small viewing angles. Again integrated and estimated fluxes are equal near $\mu = 0.5$. Values of ΔF corresponding to $0.7 \leq \mu_o \leq 0.8$ and $0.6 \leq \mu_o \leq 0.7$ are not shown but also indicate that the best value of $\overline{F}_{est}$ compared with $\overline{F}_{int}$ is for $\mu = 0.5$. When $0.5 \leq \mu_o \leq 0.6$, ΔF is smaller and changes sign near $\mu = 0.4$ as shown in Fig. 3.2.16. For Sun positions corresponding to $\mu_o \leq 0.4$, ΔF is always negative, the closest value to zero being for nadir viewing. Figure 3.2.17 gives an example showing the graph for $0.2 \leq \mu_o \leq 0.3$. For the November data, we observe a similar behaviour of the difference ΔF. Figures 3.2.18 and 3.2.19 are for $0.8 \leq \mu_o \leq 0.9$ and $0.6 \leq \mu_o \leq 0.7$ respectively during that month.

From this analysis, it can be seen that the differences between integrated and estimated SW fluxes present much variability but have, in some cases, a tendency to decrease with increasing viewing angle (see Figs. 3.2.15 and 3.2.19). Furthermore, as the solar zenith angle becomes larger, this difference becomes negative for all viewing angles (e.g. Fig. 3.2.17).

Another type of analysis was made that was inspired from Fig. 3.2.15 for April. In that figure, ΔF has a strong tendency to decrease with viewing angle. The analysis now consists of subdividing the data of April for $0.8 \leq \mu_o \leq 0.9$ according to the 12 different scene identification numbers defined in Section 1.3, and observing the behaviour of ΔF. A first analysis included every available viewing angle

ERBS NOVEMBER 1984

FIG. 3.2.18 Same as Fig. 3.2.14 with data from ERBS November as in Fig. 3.2.13 and for $0.8 \leq \mu_o \leq 0.9$.

ERBS NOVEMBER 1984
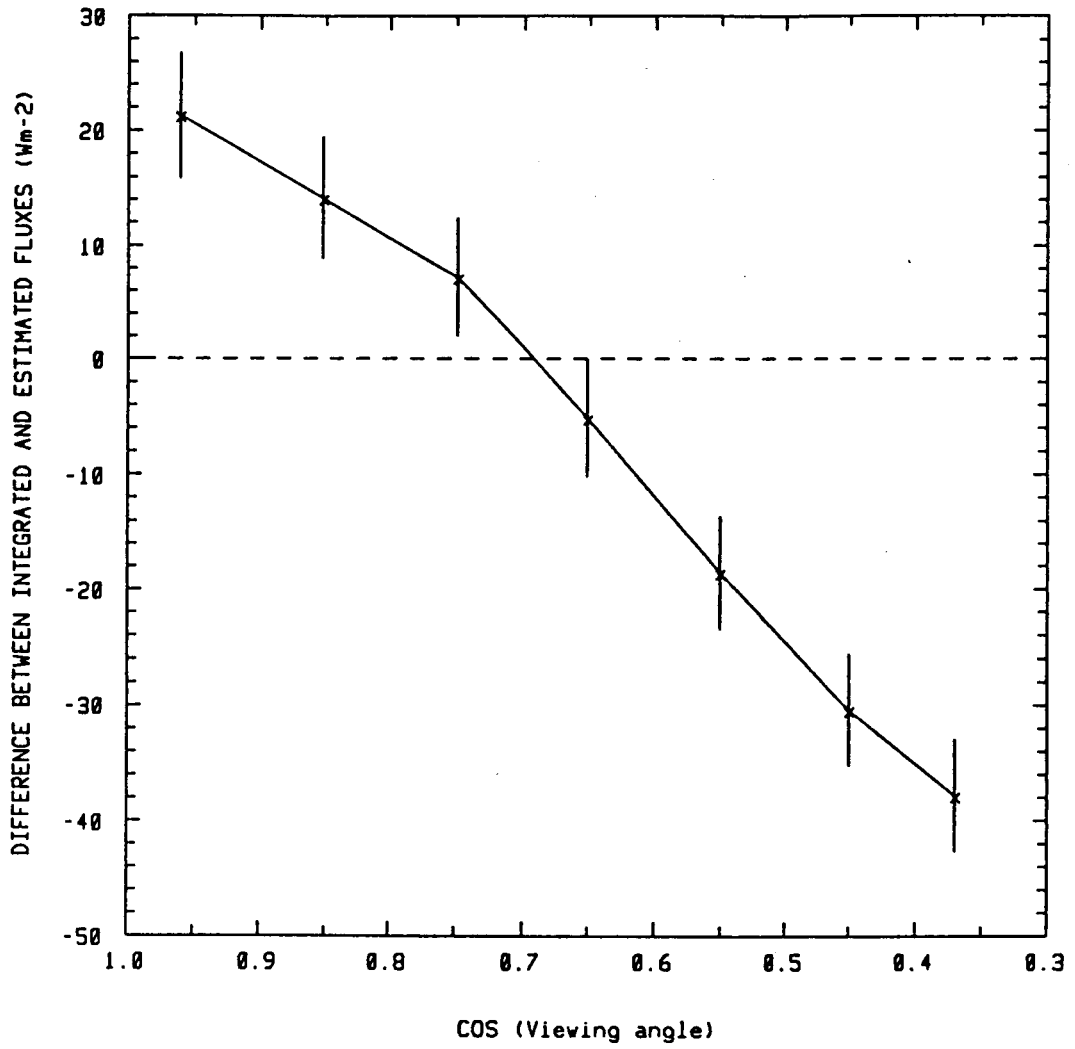
FIG. 3.2.19 Same as Fig. 3.2.18 with $0.6 \leq \mu_o \leq 0.7$.

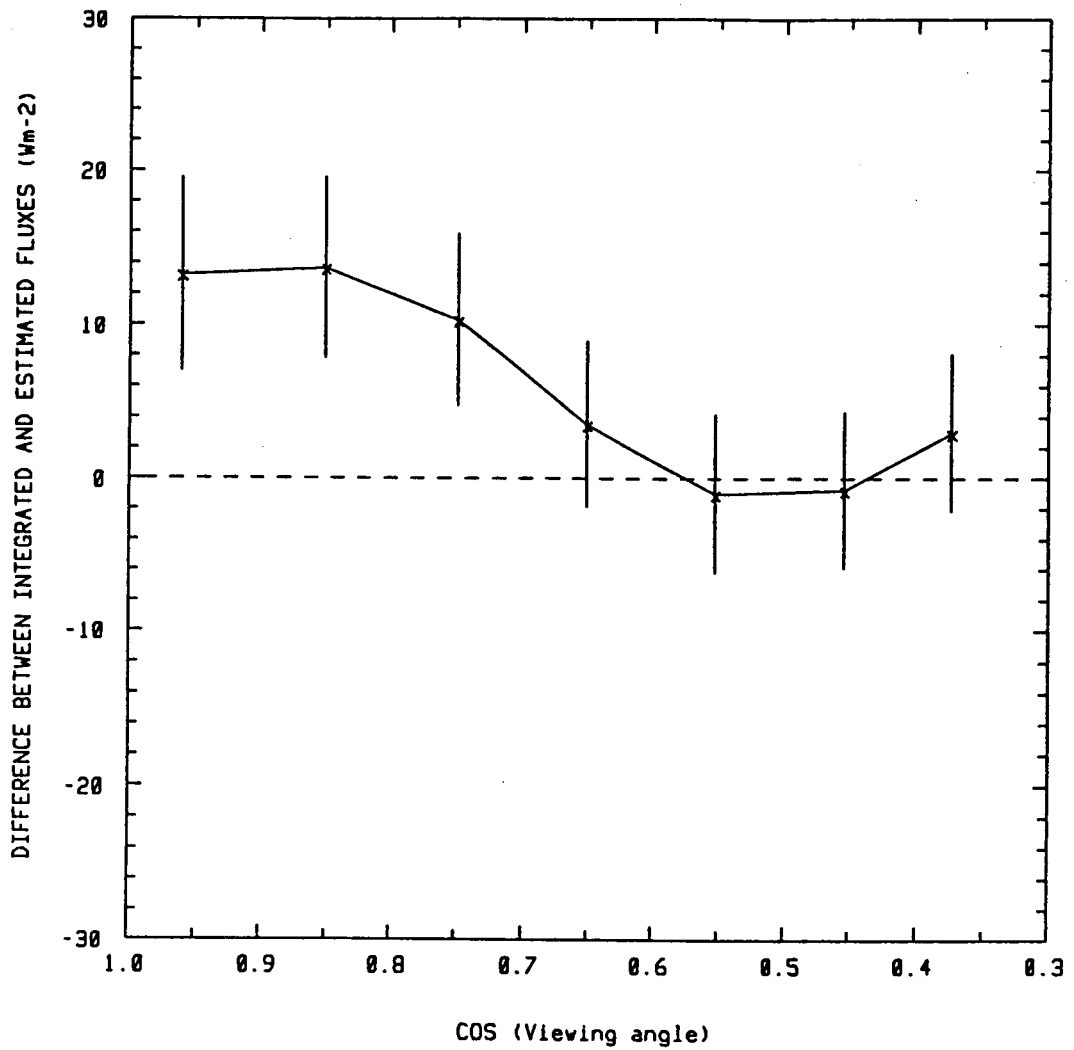in order to find a possible effect due to scene identification only. The results are presented in Fig. 3.2.20. The value of ΔF for scene type 3, "clear sky over snow", is zero since ERBS did not see this scene type in April. Results do not show an important dependence of ΔF on scene type. The values of ΔF are on each sides of the zero line and most of them are zero within a standard deviation of the mean. The maximum numbers of data, as one would expect, are for the ocean scenes. Figures 3.2.21 to 3.2.24 present ΔF versus μ for these four scenes i.e. clear ocean, partly and mostly cloudy over ocean and overcast. Even with the error bars which are overestimates of the statistical noise, the curves all show a tendency of ΔF to decrease with increasing θ. The overcast scene has the largest ΔF and shows the greatest variability in the data.

In the previous analysis the number of data per scene identification number for each viewing angle bin was also calculated. It is interesting to note from that analysis that the percentage of the number of cloudy areas increases slightly with viewing angle while the percentage of clear scenes decreases. This is possible since the scanner instrument sees more of the cloud sides as it scans towards large viewing angles so that some scenes are classified having a higher cloudiness than the one observed at the target point.

Table 3.2.1 shows the percentage of the total number of data used related to each scene type versus the viewing angle bin number, bin number 1 corresponding to nadir viewing, etc. Note that sampling was homogeneous over the Earth's surface within the latitude constraints of ERBS since, for all viewing angles, ocean scenes represent about 72% of the total data set considered, a value nearly equal to the percentage of

ERBS APRIL 1985
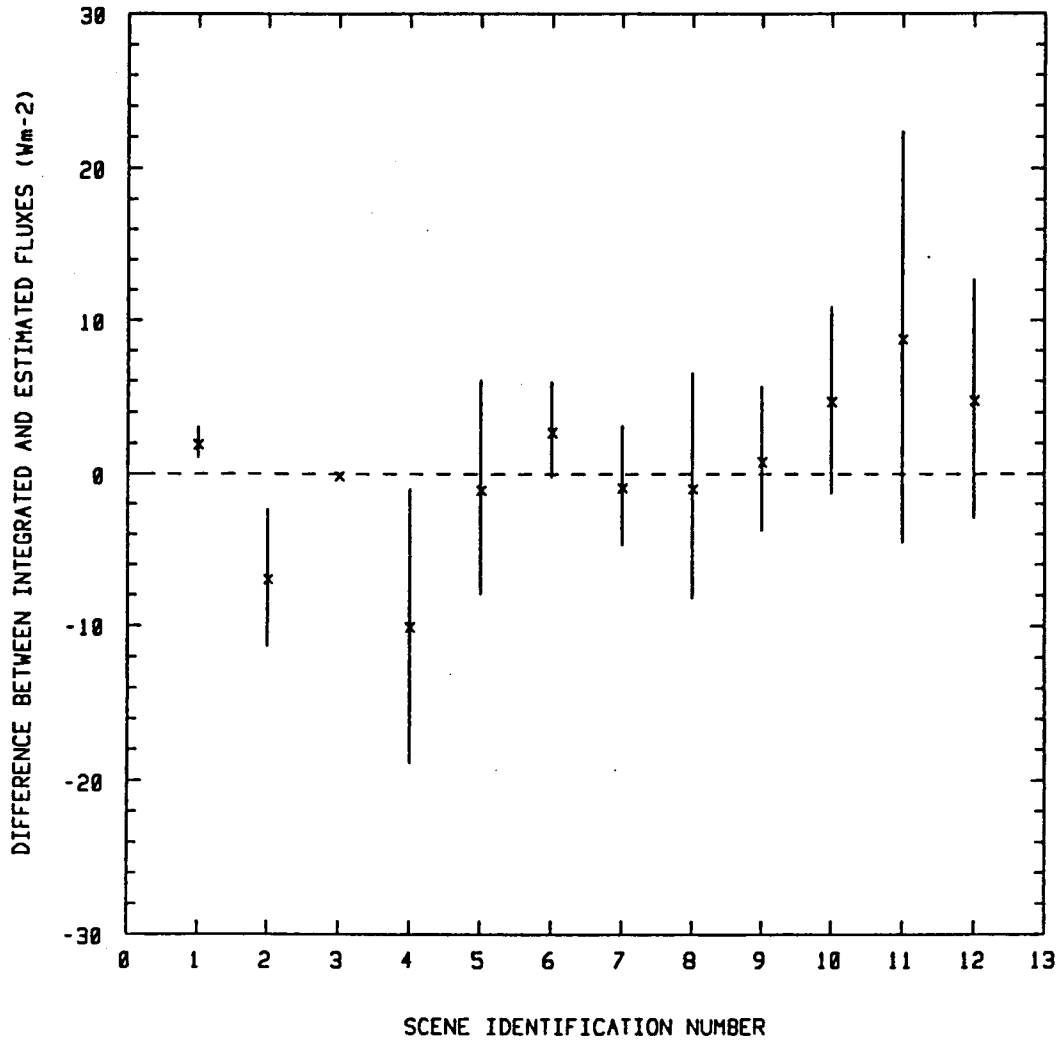
FIG. 3.2.20 Difference between integrated and estimated SW fluxes versus scene identification number (c.f. Table 1.3.1). Data are from ERBS April the 3rd to the 21st, 1985 taking alternate days and for $0.8 \leq \mu_o \leq 0.9$ and all θ.
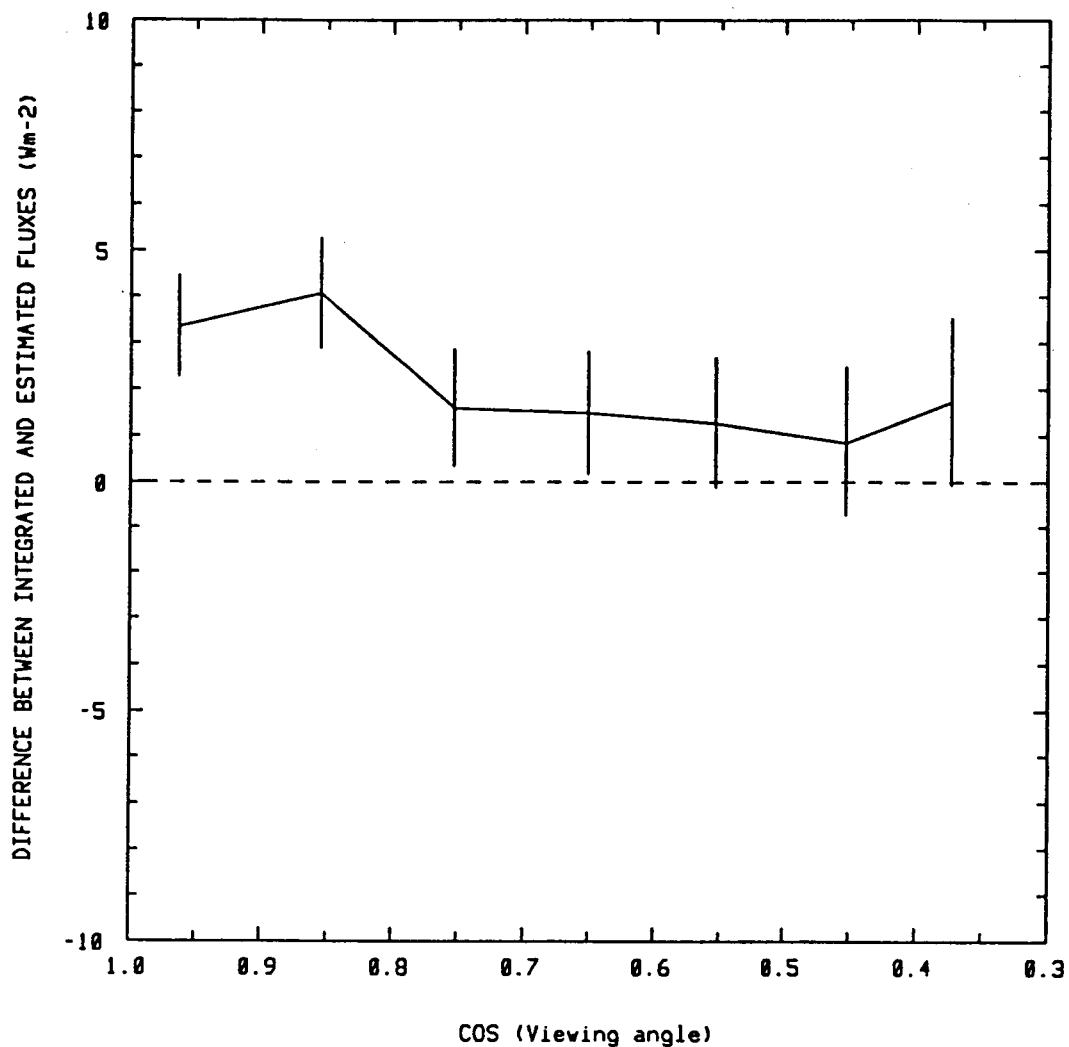
FIG. 3.2.21 Difference between integrated and estimated SW fluxes versus viewing angle for the clear ocean case. Data are from ERBS April as in Fig. 3.2.20.

ERBS APRIL 1985
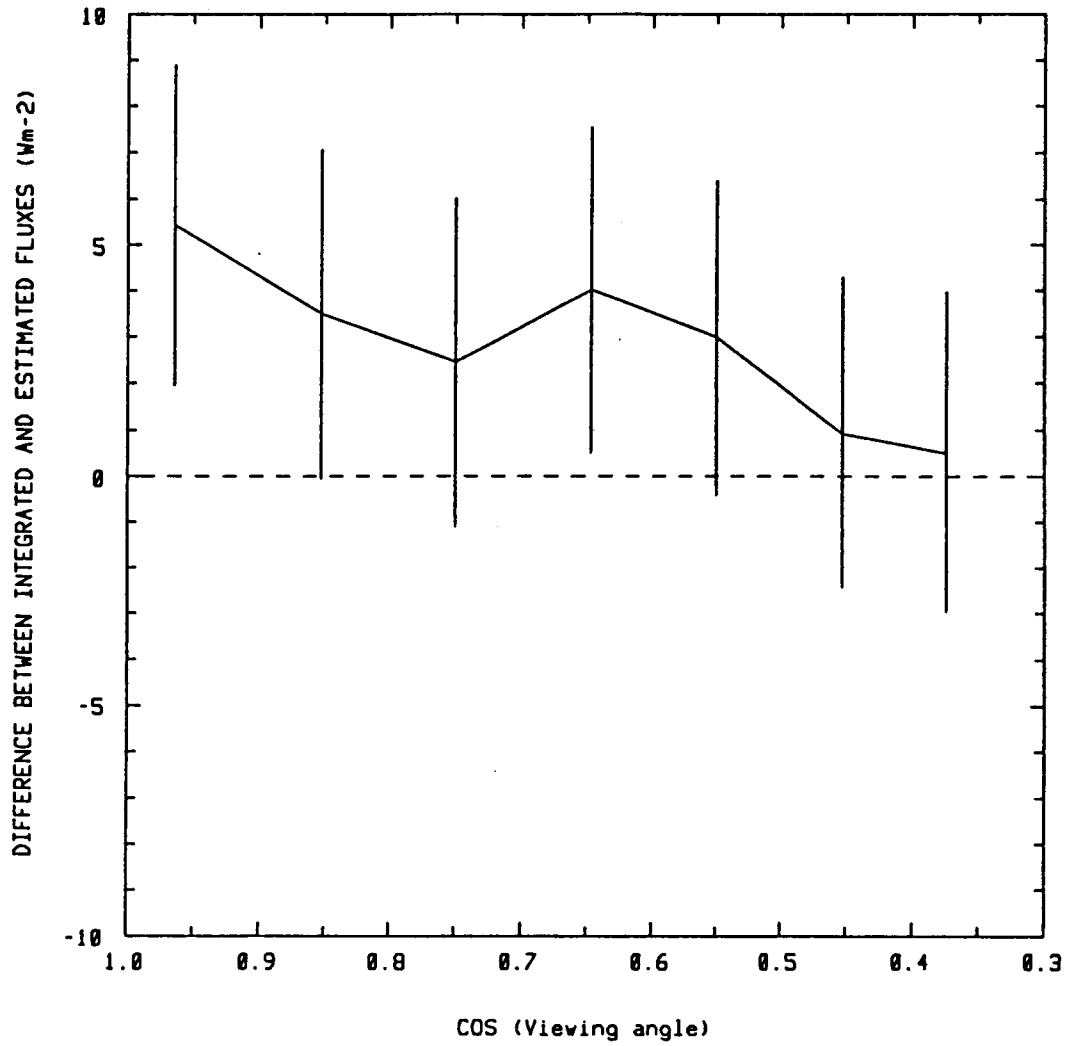
FIG. 3.2.22 Same as Fig. 3.2.21 for the partly cloudy ocean case.
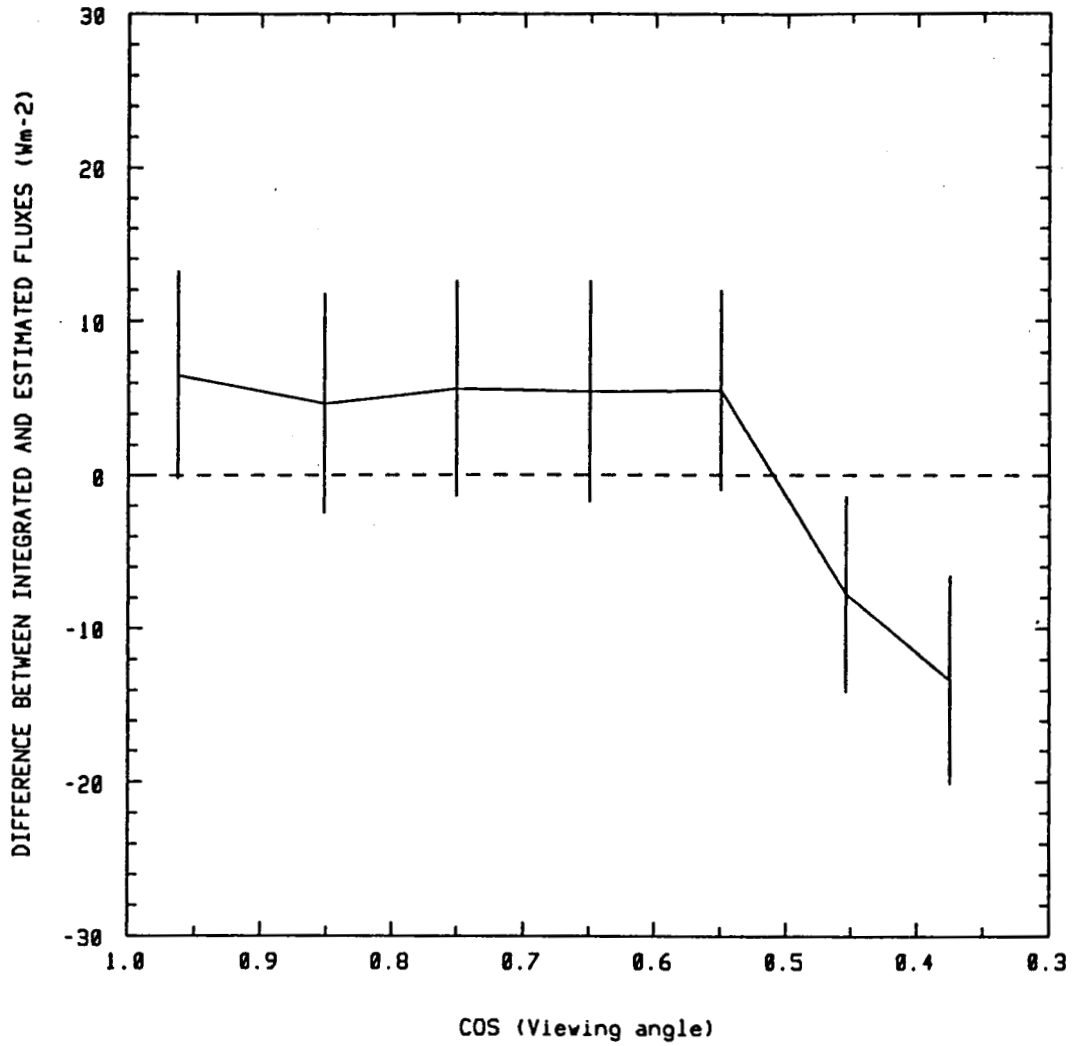
FIG. 3.2.23 · Same as Fig. 3.2.21 for the mostly cloudy ocean case.
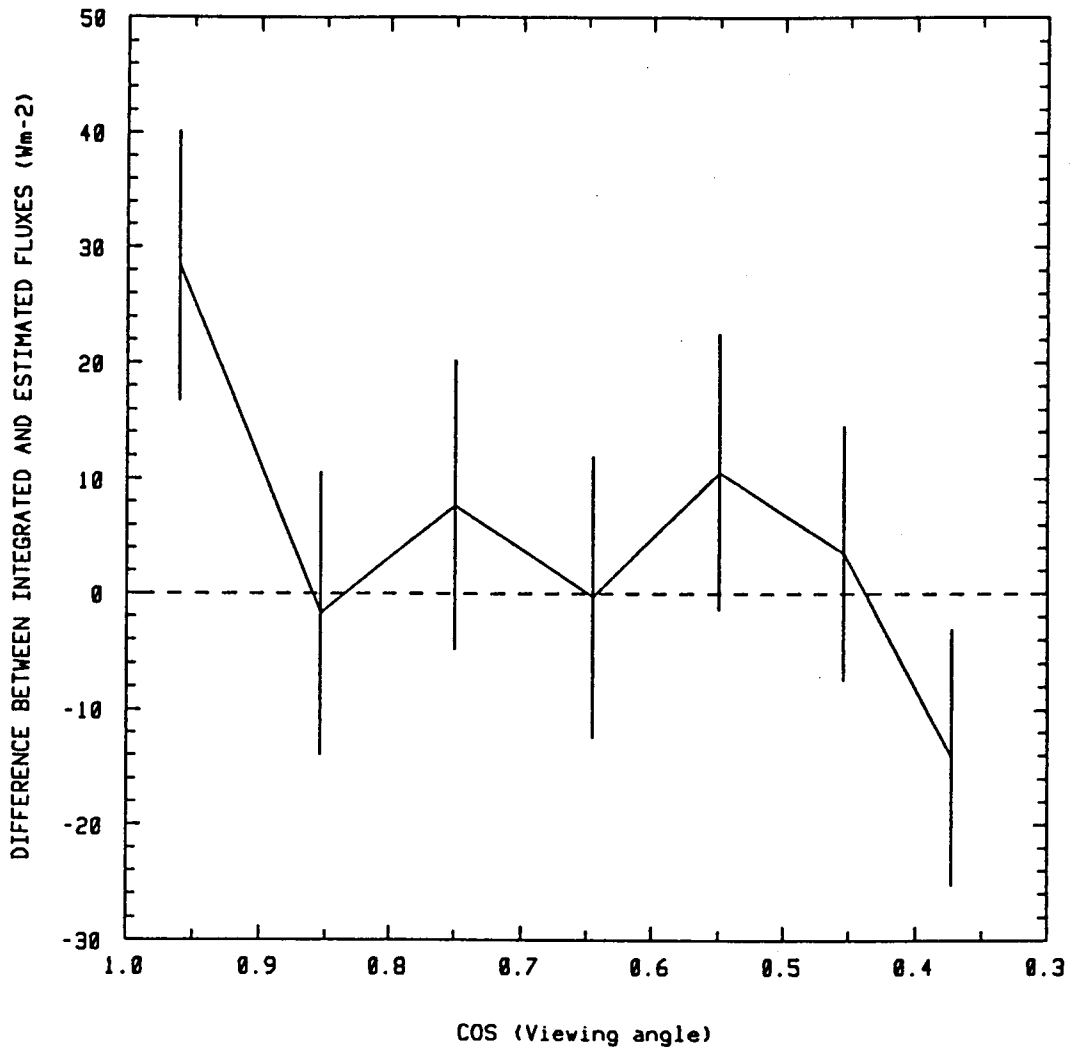
FIG. 3.2.24 Same as Fig. 3.2.21 for the overcast case.

83

TABLE 3.2.1 Percentage of the total number of data for each scene
type versus viewing angle. Data are from 10 days of ERBS April, 1985.
Viewing angle bin number 1 is for nadir viewing.

Viewing angle bin number Scene type	1	2	3	4	5	6	7
Clear ocean	18	17	16	14	11	10	7
Clear land	4	4	4	4	3	3	2
Clear snow	0	0	0	0	0	0	0
Clear desert	3	3	3	3	3	3	3
Clear land-ocean mix	2	2	2	2	1	1	1
Partly cloudy over ocean	24	25	27	27	29	30	32
Partly cloudy over land or desert	9	8	8	9	9	8	8
Partly cloudy over land-ocean mix	3	2	2	2	2	2	2
Mostly cloudy over ocean	16	17	17	16	18	19	19
Mostly cloudy over land or desert	7	7	7	8	8	7	8
Mostly cloudy over land-ocean mix	2	2	2	2	2	2	1
Overcast	12	13	12	13	14	15	17
Total land	30	28	28	30	28	26	25
Total ocean	70	72	72	70	72	74	75

the Earth's surface covered by water.

3.2.3   Estimated albedo

The spatial and temporal variation of the absorbed SW radiation provided by the Sun drives the atmospheric and oceanic circulations. Because it gives the amount of this absorption, the albedo is an important climatological quantity and its value inferred from the ERBE scanner measurements is certainly worth calculating. The albedo is defined as

$$\alpha = \frac{F_{sw}}{F_o \cos\theta_o} \tag{3.9}$$

where F_{sw} is the reflected SW flux, F_o is the incident solar flux density, and again θ_o is the solar zenith angle.

The results presented in this section are from 7 consecutive days of ERBS April 1985 data set. The albedo was calculated using the estimated SW fluxes given by the bidirectional models. The incident solar flux density in Wm^{-2} was calculated using the Earth-Sun distance d given in astronomical units such that

$$F_o = \frac{1368 \ Wm^{-2}}{d^2} \tag{3.10}$$

where $1368 \ Wm^{-2}$ is the solar constant. This value was taken from Wen (1987) in order to compare some of his results. It is important to note that a temporal averaging of the albedo would require diurnal corrections (Smith *et al.*, 1986) but for the purpose of studying the

variability of the data and its dependence on solar zenith and viewing angles, this procedure is not necessary.

The data were divided according to μ_o and μ bins in the same way as in the previous sections : 10 μ_o bins with $\Delta\mu_o$ — 0.1 and 7 μ bins with $\Delta\mu$ — 0.1 for $0.3 \leq \mu \leq 1.0$ since no data are available for $\mu \leq 0.3$.

Figure 3.2.25 shows the dependence of α on μ for each of the 10 solar zenith bins. The 10 curves are in order with respect to Sun position, the bottom curve corresponding to overhead Sun position while the top curve is for the near horizon Sun position. Error bars are given by one standard deviation of the mean. The value of the albedo α more than doubles from a near zenith Sun position to a near horizon Sun position.

A general feature is that the albedo increases with viewing angle. The variation of α from nadir viewing to the most oblique viewing position is about 0.021 (or 10%) for overhead Sun and approximately 0.114 (or 24%) for the near horizon Sun position.

A mean value of α for all Sun positions is now calculated and plotted against μ in Fig. 3.2.26. When averaging over solar zenith angle, α was weighted by μ_o such that

$$\overline{\alpha} = \frac{\sum_{i=1}^{10} \alpha_i \, \mu_{o_i} \, \Delta\mu_o}{\sum_{i=1}^{10} \mu_{o_i} \, \Delta\mu_o} \tag{3.11}$$

where the index i is for the 10 μ_o bins, $\Delta\mu_o$ — 0.1 and

C - 2

86
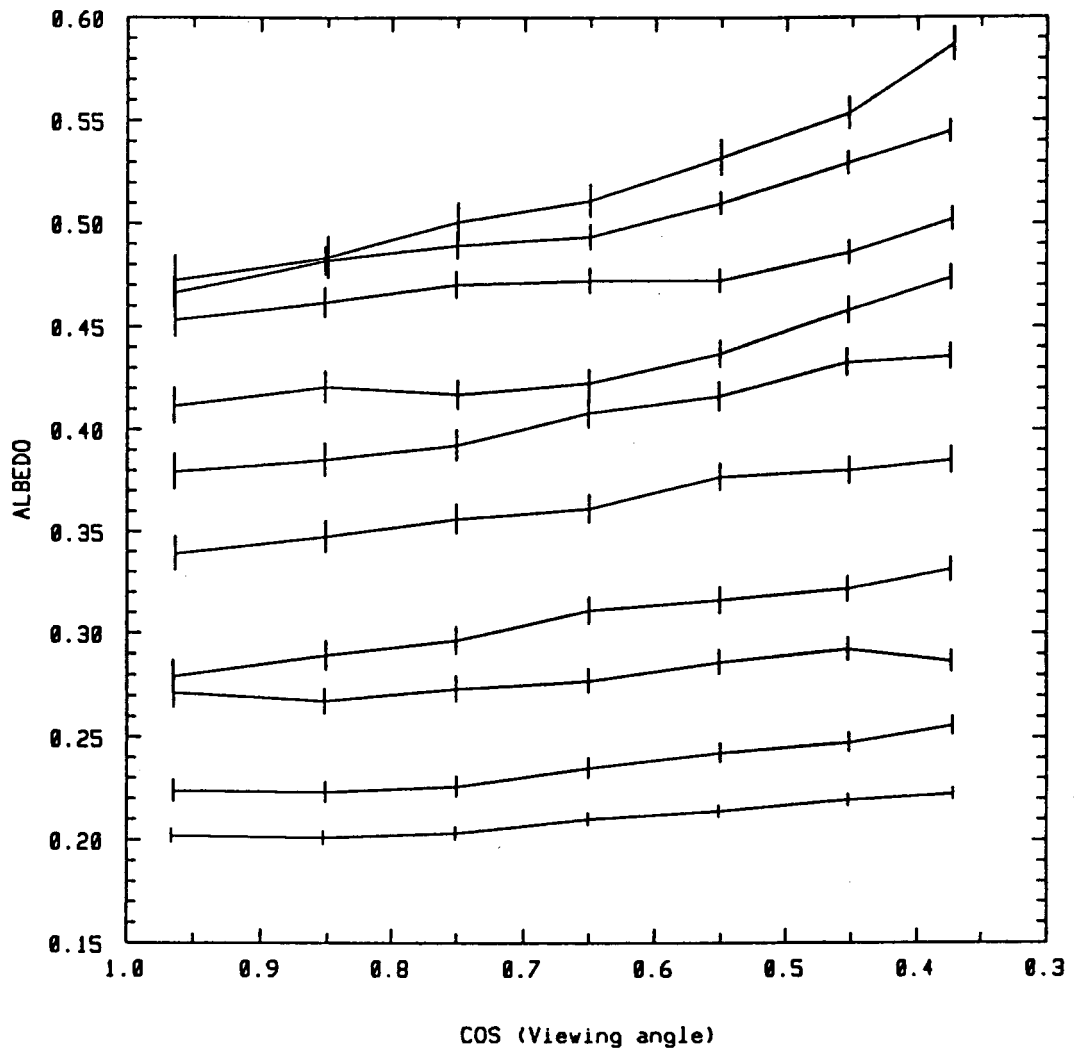
ERBS APRIL 1985

FIG. 3.2.25 Estimated albedo versus viewing angle for different Sun positions. The lower curve is for overhead Sun ($0.9 \leq \mu_o \leq 1.0$) and the upper curve is for near horizon Sun ($0.0 \leq \mu_o \leq 0.1$) with decreasing values of μ_o for curves in between. Data are from ERBS April the 16th to the 22nd, 1985.

ERBS APRIL 1985
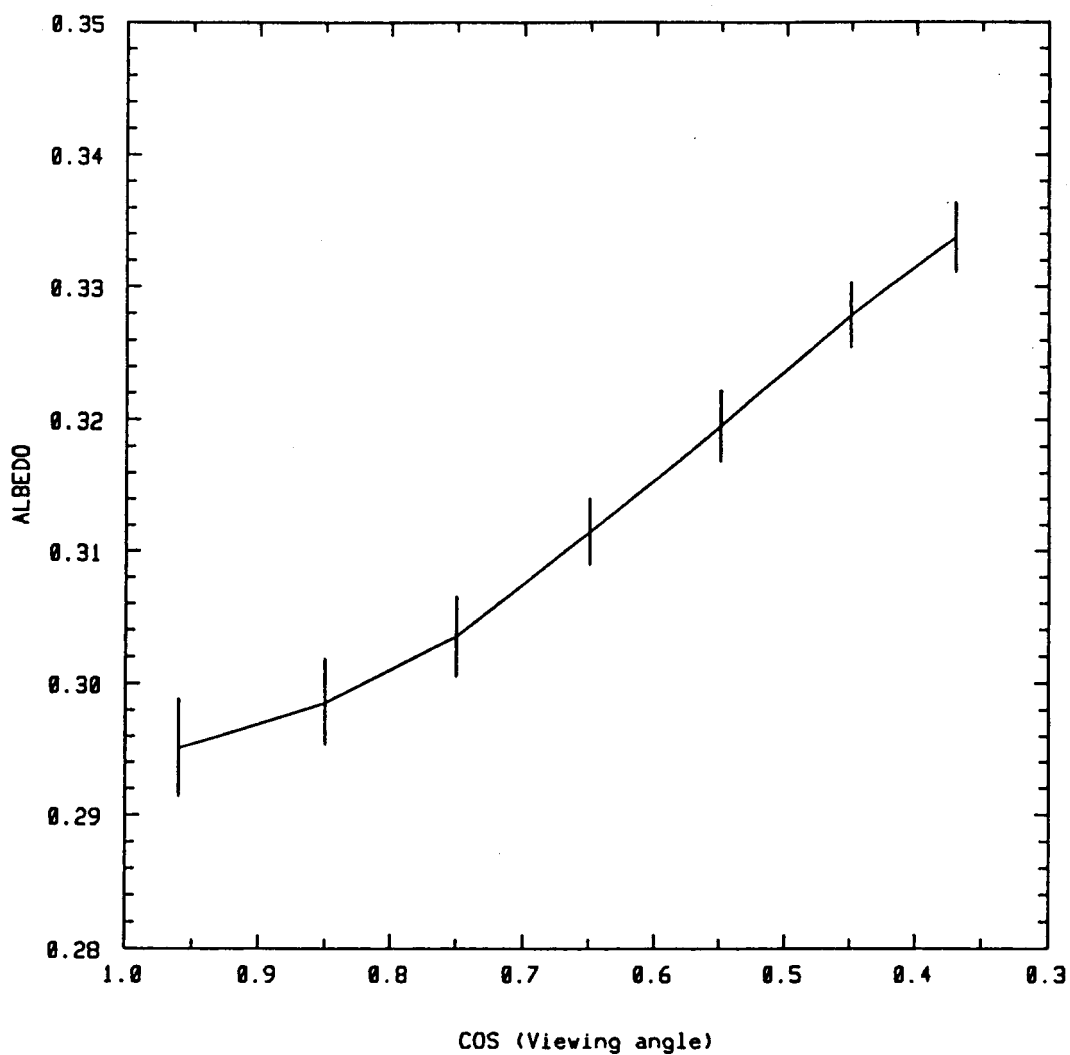
FIG. 3.2.26   Estimated albedo versus viewing angle. Data are from ERBS April as in Fig. 3.2.25 and for all θ_o.

$$\sum_{i=1}^{10} \mu_{o_i} \Delta\mu_o = \frac{1}{2} \quad . \qquad (3.12)$$

The error bars are of the order of $\Delta\alpha = 0.003$ indicating a good statistical behaviour. The values of α increase steadily with μ from 0.295 at nadir viewing to 0.334 at the largest viewing angle bin. This corresponds to a variation of 13% with viewing angle.

3.2.4 Cloud-forcing over ocean

The SW reflected and LW emitted radiation components of the planet depend on atmospheric conditions, cloudiness being one of them. As a matter of fact, the presence of clouds tends to increase the albedo so that the SW net flux reaching the ground is much less. But these same clouds will also tend to trap the LW emission of the surface and atmosphere, the lower clouds being considered as having a black-body behaviour. The radiation budget, which is defined as the difference between the incoming SW net flux and the outgoing LW net flux, can then possibly vary with cloudiness (c.f. Schneider, 1972; Ohring and Clapp, 1980; Cess *et al.*, 1982; Hartmann *et al.*, 1986; Ramanathan, 1987). The net effect of this cloud-forcing is important to evaluate because it could have serious implications for global climate and general circulation models.

In this section, the cloud-forcing is studied using only clear and overcast ocean radiation components and is defined as

$$CF = \Delta F_{cloudy\ ocean} - \Delta F_{clear\ ocean} \qquad (3.13)$$

where

$$\Delta F_x = [(F_o\mu_o - F_{sw}) - F_{lw}]_x \qquad (3.14)$$

F_o and μ_o being respectively the incident solar flux density and a mean

value of the cosine of solar zenith angle. F_{sw} and F_{lw} are the reflected SW radiation and the LW emission at the top of the atmosphere.

The data used are from the April 1985 ERBS data set, taking alternate days. The values of F_{sw} and F_{lw} are given by the ERBE estimated SW and LW fluxes. As was discussed in the last section, these estimated fluxes are sometimes quite different from the integrated fluxes. Integrated fluxes are more accurate and are considered to be good values to take. The problem is that they must be calculated. Corrections given by the study presented in Section 3.2.3 were added to the estimated fluxes in order to get the values of the integrated ones while collecting only the raw value of estimated fluxes. Doing this removes the viewing angle dependence of these data.

The fluxes were grouped by categories. For the LW, the estimated fluxes were binned according to 14 latitude bands of $10°$ starting from the equator, and to 2 scene types; clear ocean and overcast ocean. Since, as we saw earlier, estimated LW fluxes are already very good, little correction was needed but was still taken into account. The SW fluxes are much more variable and need to be separated in a larger number of categories. They were classified with the 10 usual μ_o bins and 7 μ bins as well as with the same 14 latitude bins and 2 scene type bins used for the LW fluxes. Once the corrections are made for each category, the LW fluxes were ready to be used but the SW ones had to be averaged over viewing and solar zenith angles. Since, with the corrections applied to the estimated fluxes, the viewing angle dependence must disappear, an equal weighting in μ was used. The averaging in μ_o is more complicated. The mean value of F_{sw} for each latitude band and each scene

type was given using a weighting function ω such that

$$\overline{F}_{sw}(\lambda, ID) = \sum_{i=1}^{10} \omega(\lambda)_i \ F_{sw}(\lambda, ID)_i \qquad (3.15)$$

where the index i is for the 10 solar zenith angle bins and λ and ID refer to latitude and scene identification. The ω's were derived from theoretical calculations and represent the mean fraction of an April day during which the value of the cosine of solar zenith angle falls in one of the 10 μ_o bins. This is done for each of the 14 latitude bands so that ω is really a 14×10 matrix. The procedure to calculate ω is simple and will not be discussed here. The mean value of μ_o is calculated in the same manner yielding

$$\overline{\mu}_o(\lambda) = \sum_{i=1}^{10} \omega(\lambda)_i \ \mu_{o_i} \qquad (3.16)$$

and, with the value of F_o defined as in the previous section, values of $F_o\overline{\mu}_o(\lambda)$ can be computed.

Figure 3.2.27 shows the net radiation components for clear ocean. The incoming SW net flux is given by the + sign, the outgoing LW net flux by the o sign and the x sign represents $\Delta F_{clear\ ocean}$. Error bars are drawn but are very small because of the large number of data. The SW net flux is maximum in the northern hemisphere since results are for April when the mean solar declination is $10°$. The LW net flux has a similar pattern to the curve in Fig. 3.1.4 (Section 3.1.2) with higher values of the fluxes because in this case cloudiness is restricted to be small (less than 5% for clear ocean). The radiation budget curve

91

resembles the SW net flux curve and is, as one would expect, positive at lower latitudes and negative at the higher ones.

The same three curves for the overcast ocean are shown in Fig. 3.2.28. The SW net flux is much less than for the previous case since clouds increase the albedo. The LW net flux is also smaller but its curve is still symmetric with respect to the equator. In comparison with the clear ocean case, the radiation budget curve also reaches its maximum in the northern hemisphere but drops off faster towards the North Pole.

Let us now define the SW and the LW forcing. As given earlier

$$CF = [(F_o\bar{\mu}_o - \bar{F}_{sw\ ov}) - \bar{F}_{lw\ ov}] - [(F_o\bar{\mu}_o - \bar{F}_{sw\ cl}) - \bar{F}_{lw\ cl}]$$

$$\Rightarrow CF = (\bar{F}_{sw\ cl} - \bar{F}_{sw\ ov}) + (\bar{F}_{lw\ cl} - \bar{F}_{lw\ ov})$$

$$= CF_{sw} + CF_{lw} \qquad (3.17)$$

where cl stands for clear ocean and ov for overcast ocean. A negative CF indicates a decrease in the radiation budget when a clear sky becomes a completely cloudy sky over ocean and a positive CF implies an increase in the radiation budget. Figure 3.2.29 gives the values of CF_{sw} and CF_{lw} using respectively the + and o signs. The LW forcing presents a latitudinal symmetry with higher values at the equator where convective cloud tops are colder. The x curve presents the residual and real cloud-forcing versus latitude for the ocean in April. It is everywhere negative indicating that the presence of clouds has a cooling effect on the Earth-atmosphere system.

ERBS APRIL 1985
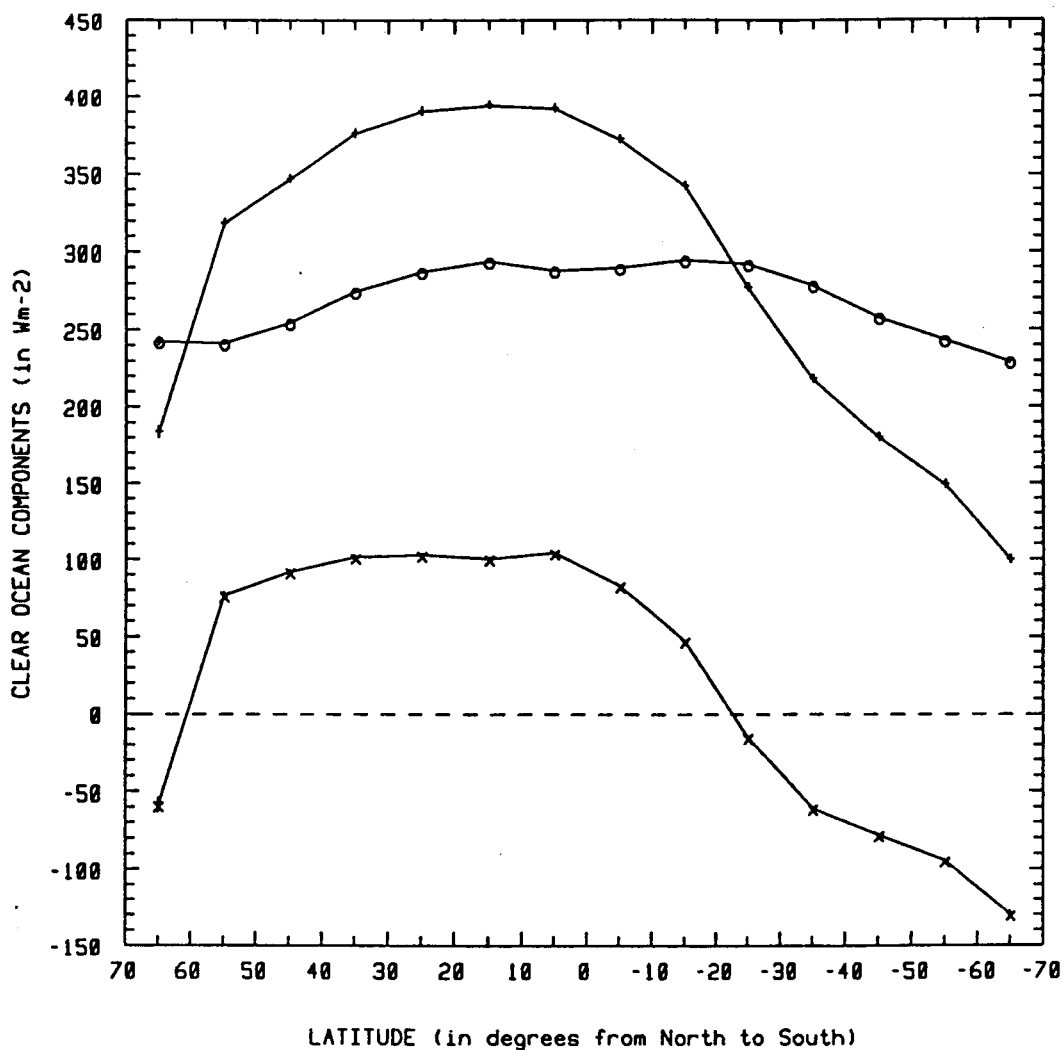
FIG. 3.2.27   SW and LW net fluxes over clear ocean versus latitude. The + sign is for incoming SW net flux, the o sign is for outgoing LW net flux and the x sign gives the radiation budget. Data are from ERBS April the 1st to the 30th, 1985 taking alternate days.

ERBS APRIL 1985

FIG. 3.2.28 Same as Fig. 3.2.27 for the overcast ocean case.

ERBS APRIL 1985
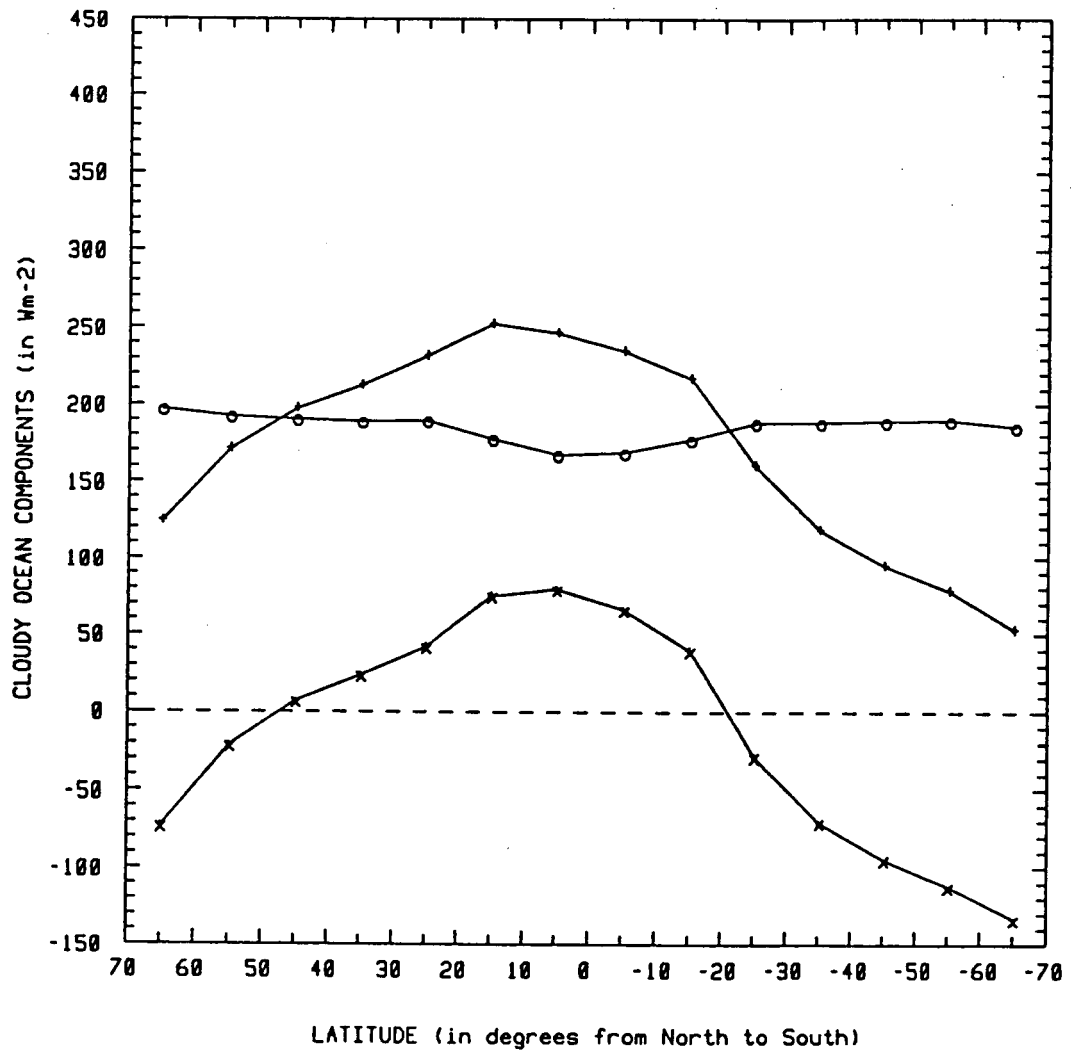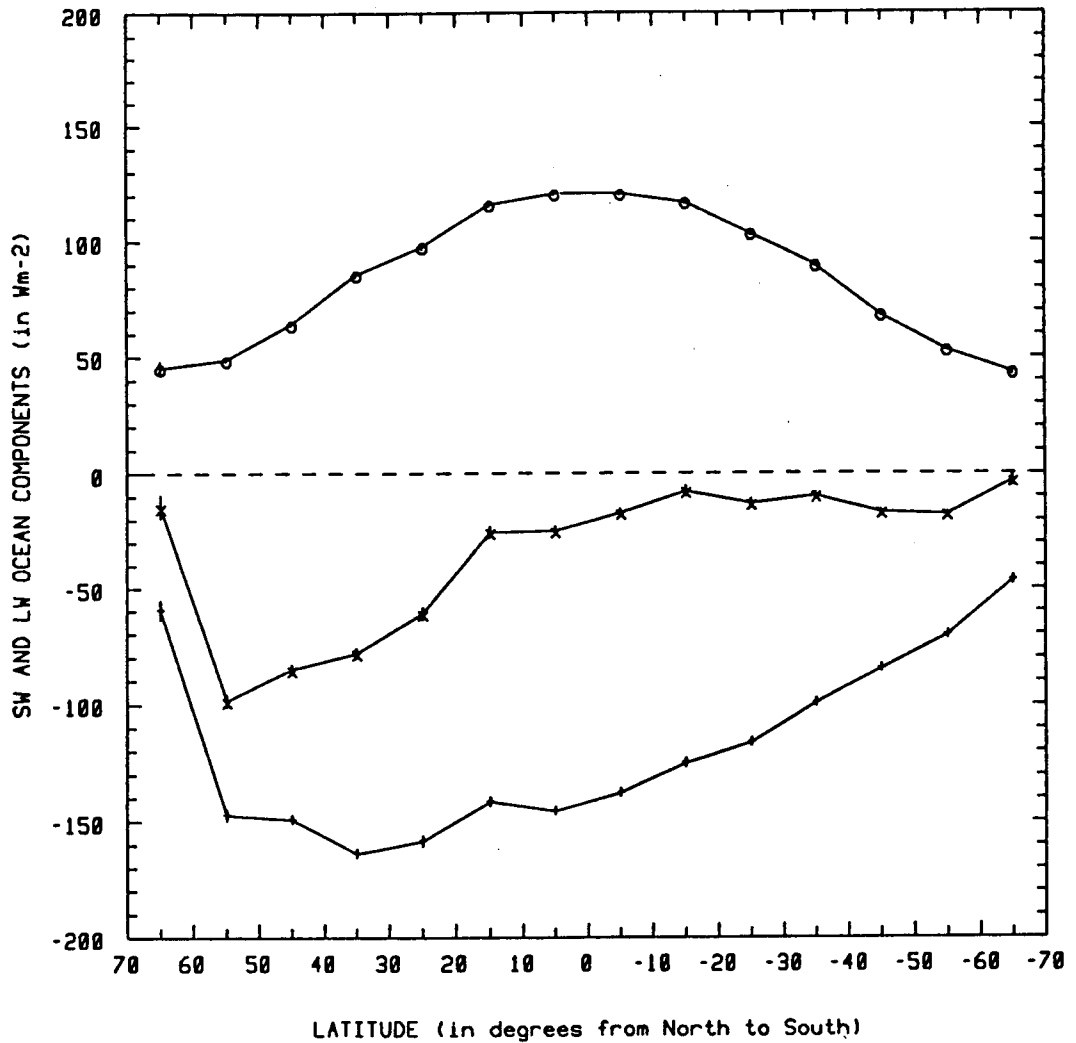

FIG. 3.2.29 SW and LW cloud forcing versus latitude. The + sign is
for the SW forcing, the o sign is for the LW forcing and the x sign is
for the total cloud forcing. Positive values indicate a reduction of
outgoing radiation with increasing cloudiness. Data are from ERBS April
as in Fig. 3.2.27.

Chapter 4

Conclusion

Based on results from the ERBE scanner data it was found that the radiance measurements show a strong statistical dependence. A quantitative study of that dependence was conducted using a linear autocorrelation coefficient calculated for several separation distances between two scanner measurements. It was indeed found that two successive along- or across-track radiance measurements, separated by a distance of 27 kilometres, are so highly correlated that they show almost identical values. In order to obtain complete decorrelation, measurements must be separated by approximately two thousand kilometres. The fact that this distance is synoptic scale suggests that cloud patterns are responsible for the high correlations. On the other hand, no conclusion on climatology can really be made on the basis of the correlation study since correlation depends on the resolution of the instruments. The results of that study must be considered as specific properties of the ERBE data.

The correlation study also showed that the along-track correlation coefficient depends on viewing angle. A possible explanation for this angle effect is the fact that, as the viewing angle increases up to 60°, the angular distribution function becomes more similar for various cloud shapes, increasing the similarity of the radiance measurements and hence the correlation. The increasing area viewed with viewing angle could also be part of the explanation but the angle effect takes place even for small values of the viewing angle where the

variation of the surface ratio is quite small.

It was also observed that the along-track correlation for longwave radiation depends on latitude, reaching a maximum in both the north and south mid-latitudes. This observation also indicates the importance of climatology in the correlation of the data. Another general feature is the fact that the SW coefficients are always smaller than the LW coefficients for equal separation distances. This is not surprising because the SW reflected radiation depends on more degrees of freedom, namely cloud type and optical thickness, than the LW emitted radiation so that much variability is observed in the SW data.

Since highly correlated data tend to give the same information, a sparse sampling strategy is suggested — that is, collection only of data that are separated by a certain physical distance on Earth. The decorrelation distance of two thousand kilometres should not be chosen since the autocorrelation coefficient does not present a sharp decrease, but tends smoothly towards zero and a good deal of information would be lost. It was decided to take the value d of the separation distance for which

$$\int_0^d R(x)\ dx \quad = \quad \frac{1}{2} \int_0^\infty R(x)\ dx \qquad (4.1)$$

which is approximately 400 kilometres. Corresponding to that distance, a jump of 16 consecutive scanlines is made while collecting the data. They are afterwards treated like statistically independent data.

Further research can still be made in that field with the ERBE data, particularly verifying the variations of the autocorrelation

coefficient with solar zenith angle using a much larger data set than for the results presented in this work. The latitudinal dependence for ERBS correlation as well as the NOAA-9 and -10 whole data sets are surely to be looked at with more care but for the purpose of finding a sampling procedure to avoid redundancy and save computer time and memory space, the present study should be sufficient.

Radiances and estimated fluxes from two different months of ERBS data were studied using the suggested sampling strategy. Mean values of radiance versus viewing angle show a smooth behaviour with low statistical noise, giving high confidence to the values of the flux obtained by integrating these radiances, i.e. the integrated fluxes. When compared with the integrated fluxes the estimated fluxes tend to be larger at large viewing angles. This should not be the case. Similarly, the estimated albedo based on estimated fluxes also depends on viewing angle, increasing several percent from nadir to oblique viewing. Biases in the bidirectional models used to infer the estimated fluxes from the measured radiances could explain this behaviour. Dependence of estimated SW fluxes on solar zenith angle is observed as well, these fluxes being smaller than their corresponding integrated SW fluxes for near nadir Sun positions and much larger for oblique and near horizon Sun positions. Again, this feature may be due to the bidirectional models.

The values of two important climatological quantities were derived from ERBS April 1985 data set. First, the estimated value of the global albedo for a week of April is near 31%, a value in agreement with the previous satellite observations (Hartmann *et al.*, 1986). It is noted

that the albedo reaches its maximum for a near horizon Sun position. Secondly, it was established that for the whole month of April 1985, the mean cloud-forcing over ocean is negative indicating a reduction of the radiation budget with increasing cloudiness over this scene type. For that month, the cloud-forcing can reach a minimum of about -100 Wm^{-2} over ocean.

Future work concerning cloud-forcing inferred from the ERBE data is still to be performed. An important study that should be considered is the comparison between the cloud-forcing calculated for the whole of the data for one month and the cloud-forcing obtained with the sparse sampling for that same month. Similar results would show the usefulness of this sampling strategy since the same answer could be obtained more rapidly. Different results could even identify the necessity of adopting a sparse sampling. As a matter of fact, using all the data available for a month in order to calculate a mean value could lead to a overweighting of certain categories of data since these data are highly correlated. Such a study could yield interesting results.

Furthermore, similar studies of cloud-forcing over the different land scene types or for different months would be of interest. A study of such forcing for various Sun positions using the ERBE data would be a more sophisticated approach as would the correction for diurnal effects. This can be done more rapidly by applying the sampling strategy presented in this work since the large ERBE data volume could then be significantly reduced with little loss of information.

REFERENCES

Barkstrom B. R., 1984 : The Earth Radiation Budget Experiment (ERBE). *Bull. Am. Meteorol. Soc.*, **65**, 1170-1185.

Cess R. D., B. P. Briegleb and M. S. Lian, 1982 : Low-latitude cloudiness and climate feedback : comparative estimates from satellite data. *J. Atmos. Sci.*, **39**, 53-59.

Coakley J. A. Jr. and R. Davies, 1986 : The effect of cloud sides on reflected solar radiation as deduced from satellite observations. *J. Atmos. Sci.*, **43**, 1025-1035.

Davies R., 1984 : Reflected solar radiances from broken cloud scenes and the interpretation of scanner measurements. *J. Geophys. Res.*, **89**, 1259-1266.

Edwards Allen L., 1979 : *Multiple regression and the analysis of variance and covariance*. W. H. Freeman and Company, 212 pp.

Hartmann D. L., V. Ramanathan, A. Berroir and G. E. Hunt, 1986 : Earth radiation budget data and climate research. *Rev. Geophys.*, **24**, 439-468.

Minutes of the twenty-second Earth Radiation Budget Experiment (ERBE) science team meeting held at Drexel University Philadelphia, PA. NASA Langley research center, February 1988.

Minutes of the twenty-third Earth Radiation Budget Experiment (ERBE) science team meeting held at NASA Langley research center Hampton, VA. NASA Langley research center, May 1988.

Ohring G. and P. Clapp, 1980 : The effect of changes in cloud amount on the net radiation at the top of the atmosphere. *J. Atmos. Sci.*, **37**, 447-454.

Ramanathan V., 1987 : The role of Earth radiation budget studies in climate and general circulation research. *J. Geophys. Res.*, **92**, 4075-4095.

Schneider S. H., 1972 : Cloudiness as a global climate feedback mechanism : the effects on the radiation balance and the surface temperature of variations in cloudiness. *J. Atmos. Sci.*, **29**, 1413-1422.

Smith G. L., R. N. Green, E. Raschke, L. M. Avis, J. T. Suttles, B. A. Wielicki and R. Davies, 1986 : Inversion methods for satellite studies of the Earth's radiation budget : development of algorithms for the ERBE mission. *Rev. Geophys.*, **24**, 407-421.

Stephens G. L., G. G. Campbell and T. H. Vonder Haar, 1981 : Earth radiation budgets. *J. Geophys. Res.*, **86**, 9739-9760.

Wen G., 1987 : Analysis of the Earth Radiation Budget Satellite scanner measurements. M. Sc., Purdue University, 98 pp.